DISS. ETH NO. 18345

Enhanced Transport Phenomena involving Droplets with Nanoparticles

A dissertation submitted to

ETH ZURICH

for the degree of

DOCTOR OF SCIENCES

presented by

Hans MAGNUS Alexander FISCHER

Diplom-Ingenieur
Technische Universität Darmstadt

born March 3^{rd}, 1978
citizen of Germany

accepted on the recommendation of

Prof. Dr. Dimos Poulikakos
Prof. Dr. John Thome

2009

Acknowledgements

I owe my gratitude to numerous people who have motivated and supported me during my stay as a doctoral student at the Laboratory of Thermodynamics in Emerging Technologies (LTNT).

First of all, I am grateful to *Prof. Dr. Dimos Poulikakos* for supervising this project, for his support and for giving me the opportunity to work in his laboratory. I also thank *Prof. Dr. John Thome* for co-advising this thesis and his interest in my work.

When I started my thesis, more than three years ago, I did my first steps under the guidance of *Dr. Mathias Dietzel*. I sincerely thank him for his valuable help and his encouragement during the first project of this thesis.

Further, I wish to express my gratitude to *Dr. Igor Zinovik* for the fruitful scientific discussions on the dissolution of oxygen bubbles as well as for his general advice.

I am very grateful to *Dr. Damir Juric* for the collaboration on Front Tracking methods, for the time he spent working with me during my stays in Paris, as well as his valuable and inspiring suggestions.

Finally, I would like to thank my colleagues and friends at the LTNT for giving me a warm welcome and for the numerous recreational activities, such as snow ball fights and hiking trips. Among others, I want to mention *Timo*, *Christian*, *Nico*, *Brian*, *Niklas*, *Cédric* and *Philipp* for adventurous journeys to Trafalgar Square, Portugal and the Black Sea. During my stay at the LTNT I shared my office with *Christian Weinmüller*. I thank him for his friendship and for being a very pleasant office mate. Many thanks also to *Dr. Dorothea Hollnagel* for providing me with computer resources and the very helpful LaTeX template.

This thesis is dedicated to my family, especially to *Katharina*, to whom I am deeply thankful for being a constant source of motivation and moral support.

The Swiss national science foundation is kindly acknowledged for the financial support of this project under grant number 200020-107450.

Abstract

Micro- and nanofluidics are experienceing an increase in research interest as the size of microelectronics and lab-on-chip appliances continuously decreases. The underlying reason is, that an increase in power density makes the quick removal of process heat more relevant and challenging. In this context multiphase flows, as well as engineered nanofluids (nanoinks) are investigated, as they possess enhanced thermal properties. Further, the understanding of nanoink behavior plays a vital role in the manufacturing of nano- and microelectronic systems.

Despite the large range of potential applications, the unique thermophysical aspects of multiphase microfluidics, especially surface effects, are still not sufficiently understood. These include capillary and Marangoni effects at phase interfaces as well as the transfer of mass, momentum and energy across interfaces. Moreover the convective and diffusive nanoparticle transport and its influence on the thermal transport needs further investigation.

The present research work aims to theoretically and numerically investigate physical aspects connected to microfluidics by focusing on three different scenarios: The diffusion controlled shrinking of micron sized nanoink droplets, the dissolution of gas bubbles into a surrounding liquid and the thermal transport in liquid-liquid flow of nanofluid droplets through microchannels.

In the first part of the thesis a theoretical investigation of the diffusion-dominated shrinking of a nanoink droplet into a surrounding liquid of a different substance is presented. The shrinking is controlled by thermally enhancing the solubility of the droplet into the surrounding medium. The spherically symmetric model is based on the mass, momentum and energy transport equations for both phases, taking all important thermophysical phenomena such as particle transport and diffusion processes within the droplet and the surrounding medium into account. Analytical solutions for the interfacial velocity and the velocity fields are presented. Parametric studies reveal the strong influence of temperature on the shrinking process.

In a second step, the derived methodology is applied to investigate the dissolution of micron-sized oxygen bubbles into a surrounding blood medium. The collapse of the bubbles is controlled by diffusion, which is facilitated by the oxygen uptake reaction between the dissolved gas and the hemoglobin in the red blood cells. Results for several physiological parameters and bubble sizes are obtained, showing that the collapse time may vary from ten seconds to two or three hours.

Finally, the thermal transport and the pressure drop in a two phase liquid flow of nanofluid droplets through microchannels is investigated. The calculation of the multiphase-multispecies flow problem is performed applying a Front Tracking Method, additionally extended to account for nanoparticle transport in the suspended phase. The influence of differently shaped droplets on the thermal transport

and the friction losses in the channel are investigated. The effect of Marangoni flow at the liquid interfaces is further taken into account and quantified. It is shown that the use of a second suspended liquid (with or without nanoparticles) is an efficient way to significantly increase the thermal performance while avoiding large pressure drop.

Zusammenfassung

Mit zunehmend kleineren Elektronik-Bauteilen rückt die Mikrofluidtechnik in den Fokus des Forschungsinteresses. Dabei wird unter anderem nach Möglichkeiten gesucht, die durch die hohe Energiedichte der Bauteile anfallende Wärme möglichst schnell abzutransportieren. Um dies zu erreichen, werden neben Mehrphasenströmungen auch künstlich hergestellte Nanofluide (so genannte Nanotinten) eingesetzt, da diese bessere thermische Eigenschaften aufweisen. Auch bei der Herstellung von mikroelektronischen Bauteilen spielt der Gebrauch dieser Nanotinten eine wesentliche Rolle.

Trotz der Vielfalt an potentiellen Anwendungen sind die speziellen thermophysikalischen Aspekte von Mehrphasenströmungen im Bereich der Mikrofluidtechnik noch nicht ausreichend verstanden. Hierzu zählen Kapillar- und Marangoni-Effekte sowie der Übergang von Masse, Impuls und Energie an Phasengrenzflächen. Bei der Untersuchung von Nanotinten ist zudem der konvektive und diffusive Transport von Nanopartikeln und sein Einfluss auf den Energietransport zu berücksichtigen.

Die vorliegende Arbeit zielt auf die theoretische und numerische Untersuchung der physikalischen Aspekte in Mikroströmungen. Hierzu werden exemplarisch drei verschiedene Szenarien betrachtet: Das diffusionsbestimmte Schrumpfen von Nanotintentröpfchen, die Auflösung von Gasblasen in eine sie umgebende Flüssigkeit sowie der Wärmetransport in Zweiphasenströmungen mit Nanofluidtropfen durch Mikrokanäle.

Der erste Teil der Dissertation untersucht das diffusionsbestimmte Schrumpfen eines Nanotintentropfens in eine ihn umgebende Flüssigkeit (z.B. Wasser). Durch das Erhöhen der Löslichkeit des Tropfens in das umgebende Medium kann das Schrumpfen thermisch reguliert werden. Zur Betrachtung dieses Phänomens wird ein kugelsymmetrisches Modell erstellt. Dieses basiert auf den Transportgleichungen für Masse, Impuls und Energie in beiden Phasen. Alle wichtigen thermophysikalischen Phänomene, wie zum Beispiel der Nanopartikeltransport und die Diffusionsprozesse innerhalb des Tropfens und der ihn umgebenden Phase, werden berücksichtigt. Für die Geschwindigkeit der Phasengrenzfläche sowie die Geschwindigkeitsverteilung in beiden Phasen wird eine analytische Lösung hergeleitet. Parameterstudien offenbaren den großen Einfluss der Temperatur auf den Schrumpfungsprozess.

In einem zweiten Schritt wird die hergeleitete Methodik verwendet, um die Auflösung von kleinsten Sauerstoffblasen in Blut zu untersuchen. Der Zerfall der Blasen wird durch Diffusion bestimmt. Der Prozess wird durch die Aufnahme des gelösten Gases durch das Hämoglobin erleichtert. Mehrere Fälle mit unterschiedlichen physiologischen Parametern und Blasengrößen werden betrachtet. Die Ergebnisse zeigen, dass die Zeit bis zur vollständigen Auflösung der Blase zwischen zehn Sekunden und zwei bis drei Stunden variieren kann.

Im dritten Teil der Arbeit werden Wärmetransport und Druckverlust in Zweiphasenströmungen von Nanofluidtropfen in Mikrokanälen untersucht. Die Berechnung dieses Mehrphasen- und Mehrstoffströmungsproblems wird durch die Anwendung der Front-Tracking Methode gelöst. Soweit erforderlich wird diese um die Berücksichtigung des Transports von Nanopartikeln in den Tropfen erweitert. Der Einfluss verschiedener Tropfenformen (Pfropfen und sphärische Tropfen) auf den Wärmetransport und auf die Reibungsverluste wird untersucht. Ergebnisse von Parameterstudien zum Einfluss verschiedener Faktoren im Zusammenhang mit dem Wärmetransport in Mikrokanälen werden präsentiert. Auch der Effekt von Marangoniströmungen an der Phasengrenzfläche wird berücksichtigt und quantifiziert. Es wird gezeigt, dass die Verwendung einer zweiten unlöslichen Phase (mit oder ohne Nanopartikel) ein effizienter Weg ist, um ohne große Druckverluste den Wärmeübergang erheblich zu erhöhen.

Contents

Chapter 1

Introduction

1.1 Motivation

In recent years, liquid suspensions containing nanoparticles (nanoinks) gained significant attention in science and engineering. Their unique thermophysical properties, such as a drastically reduced melting temperature of the nanoparticles compared to their bulk counterpart [1, 2], allow for novel methods in the manufacturing of nano- and microelectronic devices. These include the mask-less writing of electrically conductive circuits on temperature sensitive organic substrates [3, 4], the assembly of flexible nanoscale transistors [5, 6] or the soldering of carbon nanotubes on metal pads [7]. For these purposes nanoinks are printed on flexible or rigid surfaces with a drop-on-demand ink jet technology or with a fountain pen method and subsequently treated with a laser to evaporate the solvent and to coalesce the particles [8–10]. It was experimentally shown, that a further size reduction can be achieved if the nanoink is surrounded by an initially immiscible secondary liquid, such as water, which then, by thermally increasing the solubility of the nanoink into the surroundings, causes shrinking and dewetting of the deposited nanoink structures [11]. Dockendorf et al. [11] showed, that by applying this method, the pattern size can be reduced to a few microns.

The continuous size reduction of micro-electronic devices makes their thermal management much more important. The demand of quick heat removal in microscale devices such as microprocessors or micro fuel cells explains the growing research activities in the field of liquid cooling [12–15]. Among the various proposed techniques to improve the cooling performance in micro channels, two promising approaches are mentioned in the following. One exploits the fact, that the heat transfer from the channel wall in multiphase flows is increased in comparison to single phase flows. In the presence of immersed bubbles the thermal transport is augmented by a blockage effect in front of the bubbles and recirculation in their wake [16–19]. Another option to improve the cooling performance of microchannels is to employ nanofluids. Nanofluids possess a significantly increased thermal conductivity at concentrations of a few percent per volume, however, at the expense of increased viscosity. Depending on particle size and concentration, the effective thermal conductivity of nanofluids can be increased by as much as 10 to 40% [20, 21].

1.2 Physics at the Microscale

The present work investigates various physical phenomena occurring in microfluidic devices. The importance of these phenomena can be described by a series of dimensionless groups, such as the Reynolds number, the Peclet number, the Capillary number and the Marangoni number.

In contradiction to the macroscale, the Reynolds number is the least important of the above mentioned numbers, as in microfluidics usually very low Reynolds number flows are encountered. The Reynolds number, which relates inertia forces to viscous forces is defined as:

$$\mathrm{Re} = \frac{\rho v_0 L}{\mu}, \tag{1.1}$$

where ρ and μ are the fluid density and dynamic viscosity respectively.L and v_0 are the characteristic length scale and velocity. In the present study the Reynolds

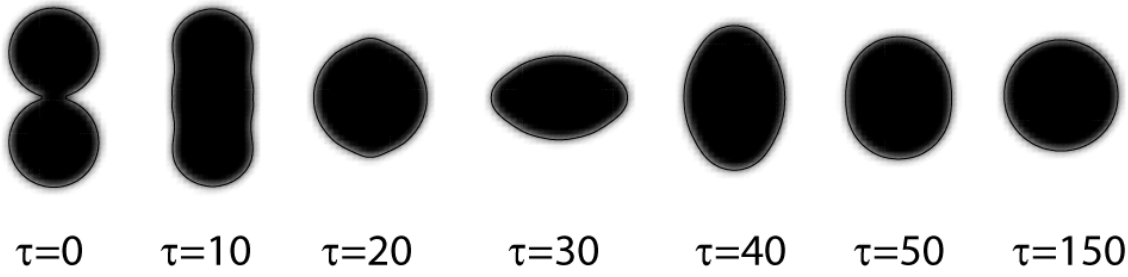

Figure 1.1: Numerical results of the coalescence of two initially separated oil droplets.

numbers are in the range of $O(10^{-6})$ and $O(10^2)$. Low Reynolds numbers imply a laminar flow regime. From this follows, that turbulence as a mixing mechanism does not play a role any more. Mixing in microfluidics is therefore driven by diffusive transport. This may result in much increased mixing times.

The Peclet number relates convective to diffusive transport. For thermal diffusion, this number is defined as:

$$Pe = \frac{v_0 L}{\kappa}, \tag{1.2}$$

with κ being the thermal diffusivity. The Peclet numbers in this study are in the range of $O(10)$ and $O(10^2)$.

As the influence of inertia forces (indicated by low Reynolds numbers) decreases and gravitational effects nearly vanish, the importance of surface and interfacial tension effects increases. This is due to the high surface-to-volume ratios in microfluidic devices. The Capillary number, which relates viscous forces to interfacial tension forces, is defined as:

$$Ca = \frac{\mu v_0}{\sigma}, \tag{1.3}$$

The importance of capillary effects in the present work can be seen by Capillary

numbers between $O(10^{-4})$ and $O(10^{-2})$.In Equation 1.3 σ is the surface tension. Surface tension is a result of the reduced cohesive energy between molecules at the free surface. A molecule at the surface of a liquid looses roughly one half of its cohesive energy. The surface tension is a direct measure of this energy shortfall per unit surface area [22]. As a result, liquids tend to minimize their surface area. This can be seen in Figure 1.1, where two initially separated silicon oil droplets merge in order to lower their surface energy. The lowest surface energy can be achieved, when the resulting droplet takes up a spherical shape. The work done by pressure and capillary forces at the interface of a droplet or bubble surrounded by a secondary phase can be written as [22]:

$$\delta W = -p_1 dV_1 - p_2 dV_2 + \sigma_{1,2} dA, \tag{1.4}$$

where dV and dA are the change in volume and surface, respectively. The condition for mechanical equilibrium $\delta W = 0$ leads to the well known Laplace equation:

$$\Delta p = p_1 - p_2 = \frac{2\sigma_{1,2}}{R}. \tag{1.5}$$

The surface tension of a fluid depends on temperature, its electrostatic potential and on the concentration of surfactants. A gradient in these properties induces a so-called Marangoni flow. In the present work, we will focus on temperature dependent surface tension. The thermal Marangoni number is defined as:

$$Ma = \frac{|\sigma_T| \nabla T L^2}{\mu \kappa}, \tag{1.6}$$

where $\sigma_T = -d\sigma/dT$. Under the influence of a thermal gradient the liquid at the interface of a droplet or bubble will experience a thermocapillary force, pushing it along the temperature gradient. Due to unbalanced stresses which are a result of surface tension gradients, the droplet moves towards higher temperatures, as shown by Gao et al. [23] and Yin et al. [24]. In their studies they present results of the thermocapillary droplet motion in closed cylinders. Similar results are illustrated in Figures 1.2 and 1.3, where the velocity and temperature field of a silicon oil droplet

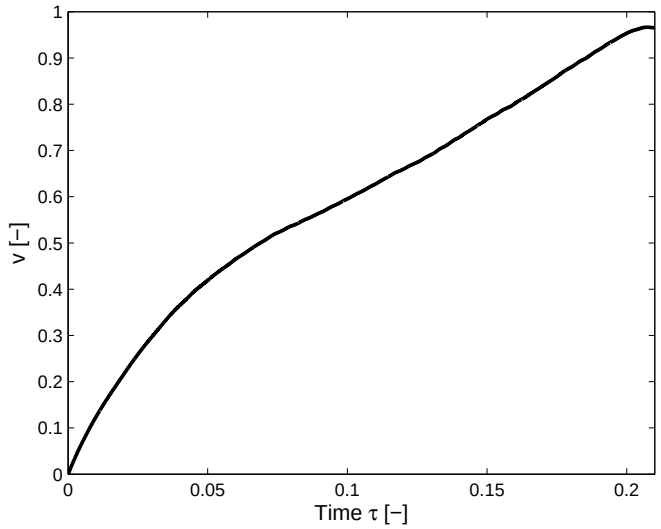

Figure 1.2: Temporal evolution of the droplet velocity induced under the influence of a temperature gradient.

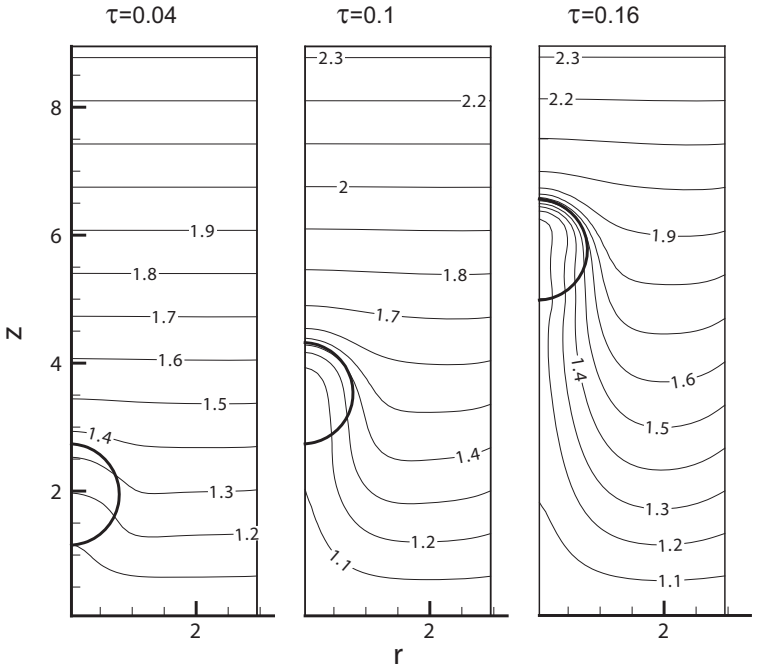

Figure 1.3: Non dimensional temperature field for different times. The temperature difference between the top and bottom of the cylinder is 40 K.

in a cylinder filled with water is shown. The temperature gradient in the carrier liquid induces the droplet velocity. The droplet accelerates and cold fluid is drawn to the wake of the droplet. During the movement of the droplet the temperature gradient at the interface rises (Figure 1.3), resulting in a further acceleration of the droplet (Figure 1.2).

In the presence of nanoparticles three additional dimensionless groups must be mentioned: the Schmidt number, relating momentum diffusivity to mass diffusivity, the Lewis number, describing the ratio of thermal diffusivity to Brownian diffusivity, as well as an additional number to relate Brownian diffusivity to thermophoretic diffusivity [25].

The Schmidt and Lewis numbers are defined as:

$$Sc = \frac{\mu}{\rho D_B} \quad Le = \frac{\lambda}{\rho_P c_P D_B \psi}, \tag{1.7}$$

where ρ_P, c_P, ψ and λ are the nanoparticle density, specific heat, concentration and the thermal conductivity of the bulk fluid respectively. D_B is the Brownian diffusion coefficient. Brownian motion describes the random motion of nanoparticles suspended in a liquid, moving with an average kinetic energy of $3/2k_bT$. The particle motion in a Newtonian liquid can be expressed by the Einstein-Stokes equation [25]:

$$D_B = \frac{k_b T}{3\pi\mu d_p}, \tag{1.8}$$

where k_b is the Boltzmann's constant. Nanoparticle diffusion is not only dominated by ordinary (Brownian) diffusion resulting concentration gradients, but also by thermal diffusion, which desribes the particle motion under the influence of a thermal gradient. Nanoparticles move in the direction of lower temperatures. Brownian diffusivity and thermophoretic diffusivity can be related as follows [25]:

$$N_{BT} = \frac{\psi D_B T \mu}{D_T \Delta T}, \tag{1.9}$$

where D_T is the thermal diffusion coefficient. In the present work N_{BT} is in the range of $O(10^{-2})$ and $O(10)$, showing the relative importance of both diffusion mechanisms

in laminar, low Reynolds number flow. The thermal diffusion coefficient D_T can be estimated as:

$$D_T = \beta \frac{\mu}{\rho} \psi, \tag{1.10}$$

with a proportionality factor β. For nanoparticles, D_T and D_B are both in the range of $O(10^{-12})$ to $O(10^{-10})$.

1.3 Outline

The following chapters aim on deepening the understanding of the various physical phenomena present in different microscale applications.

In Chapter 2 the shrinking of a nanoink droplet into a large pool of surrounding water is investigated. This should enable researches to understand the underlying physical phenomena when shrinking nanoink droplets in the process of printing small-scale electrically conductive lines and patterns on various substrates. A comprehensive spherical symmetric model of the diffusive transport mechanisms is presented. The model consists of a system of coupled differential equations, describing the related mass and energy transfer physics, in an expanding computational domain which follows the moving interface between the shrinking droplet and its surrounding liquid. In parametric studies the influence of different scenarios on the movement of the interface is investigated. These scenarios include isothermal settings as well as heating of the droplet or the outer phase.

Small scale fluidic structures are not only present in Micro-Electro-Mechanical Systems (MEMS) but also in a large variety of biological systems, such as the human body. In Chapter 3 the collapse of an oxygen bubble in surrounding blood is investigated. This is achieved by applying a modified version of the method derived in Chapter 2. The diffusion of the gas from the bubble surface is facilitated by the oxygen uptake reaction by hemoglobin in the red blood cells.

Another potential application for nanoinks is their use as a cooling liquid. In Chapter 4 we will present a numerical investigation of the heat transfer in two phase flow in microchannels. It is shown that the heat transfer can be considerably increased by introducing droplets or slugs of an immiscible liquid into the main flow. A Front Tracking Method, extended to account for nanoparticle transport, is applied to numerically solve the multiphase-multispecies flow problem. The influence of differently shaped colloidal or simply pure droplets, as well as the effect of induced Marangoni flow and viscosity differences between the two phases on the thermal transport are presented in parametric studies.

Chapter 2

On the Shrinking of a Nanoink Droplet

Parts of this chapter are published in:
M. Fischer, M. Dietzel, and D. Poulikakos. Thermally enhanced solubility for the shrinking of a nanoink droplet in a surrounding liquid. *International Journal of Heat and Mass Transfer*, 52(1-2):222-231, 2009.
M. Fischer, and D. Poulikakos. Thermally Controlled Size Reduction of Nanoink Droplets in Water *CHT-08-304, Proceedings of CHT-08*, ICHMT Symposium, May 2008, Marrakech, Morocco

2.1 Introduction

In this chapter a theoretical investigation of the phenomenon of diffusion-dominated shrinking of a nanoparticle suspension droplet in a surrounding liquid of a different substance is presented. The fluid within the droplet consists of toluene as a base fluid and nanoparticles. It is surrounded by water. After the initiation of the process the toluene diffuses over the interface between the two phases into the water, causing the nanoink droplet to shrink.

A comprehensive model of the diffusive transport mechanisms present in the nanoink droplet and the surrounding water is presented. Toluene is only marginally soluble in water at room temperature. Therefore, hardly any toluene diffuses into the surrounding water phase at ambient conditions, despite the initially steep concentration gradient at the interface between the nanoink droplet and the water. The diffusion process can be augmented by heating the fluids and hence, increasing the solubility of toluene in water [26, 27]. The present work focuses on the convective and diffusive particle transport as well as the mass, momentum (capillarity) and energy transfer across the interface.

The heat and mass transfer present in spherical droplets or bubbles with moving interfaces has been intensively investigated throughout a wide range of research fields. The present work employs the fundamental equations of a bubble growth model originally developed by Scriven [28] enhanced to describe droplet shrinkage and combined with a nanofluidic transport model introduced by Buongiorno [25] to account for the convective and diffusive nanoparticle transport within the nanoink droplet. In his work, Buongiorno identifies thermophoresis and Brownian diffusion as the major slip mechanisms causing nanoparticle transport relative to the embedding liquid and develops from this finding a two component mixture model.

The influence of different scenarios on the movement of the interface, i.e. the evolution of the shrinking process in time is investigated. These scenarios are the extent of the outer phase for isothermal settings as well as the heating of the inner or the outer phase. Solutions for the temperature and particle/solvent concentration fields inside and outside the droplet are presented.

In the following section the fundamental transport equations for mass, momentum and energy for the droplet and its surrounding as well as two additional equations describing the particle transport and diffusion of toluene in the water phase are introduced for the spherically symmetric case with particular focus on the specific boundary conditions at the interface. Based on these equations, solutions for the

velocity field within the droplet and its surrounding phase can be derived. Only the energy equation and the concentration equation for both phases have to be solved numerically. These four equations for both phases are strongly coupled and have to be computed iteratively. To facilitate the numerical solution and to immobilize the moving boundary a transformation proposed by Landau [29] is employed. The solution procedure is described in Section 2.3. Results of the calculations as well as parametric studies on the heating rate can be found in Section 2.4, followed by concluding remarks in Section 2.5.

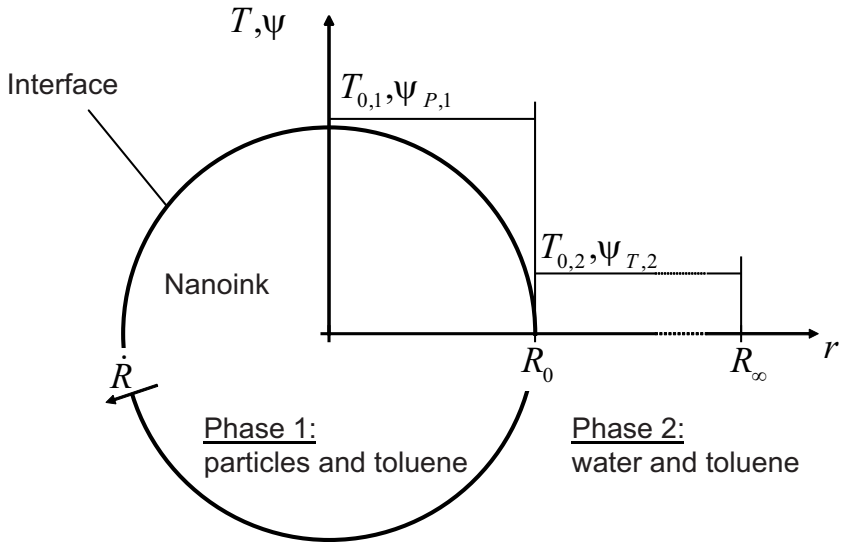

Figure 2.1: Schematic of the nanoink droplet: The nanoink droplet (phase 1) is initially surrounded by pure water (phase 2). Toluene is diffusing over the interface into the water; the droplet shrinks.

2.2 Problem Formulation

The physical system under consideration is presented in Figure 2.1. It consists of the two phases of a binary mixture. The nanoink (phase 1) is composed of gold nanoparticles and toluene. The initial particle concentration in the nanoink droplet is assumed to be 1% in volume. The nanoink droplet is separated by the moving in-

terface from phase 2. The latter is initially pure water and later, after the initiation of the diffusion process, a mixture of water and the diffused toluene. The radius of the nanoink droplet under consideration is 60 μm, resulting in a high surface-to-volume ratio (5×10^5 m^{-1}). These numerical values are in the typical range for nanoink applications and are chosen as such for the purpose of numerical calculations as well as in order to determine the importance of the various terms in the formulation of the mathematical model of the problem. From the very low Capillary and Weber numbers (order of magnitude 10^{-9} and 10^{-15}, respectively) it follows that surface tension effects dominate the problem. Small Reynolds numbers of 10^{-6} indicate a creeping flow regime (large viscous forces). Therefore convective cells inside the droplet can be neglected.

The problem can be modeled as spherical symmetric with sufficient accuracy. The fluids are treated as incompressible with no external body forces. The influence of gravity and natural convection can be regarded as negligible (the Bond and Rayleigh numbers are $\ll 1.0$). The nanoink in phase 1 is considered to be a dilute mixture with no chemical reactions [25]. This means that the presented model is only applicable for mixtures, where the particle concentration φ is less than 5% in volume. In this study this is the case until the nanoink droplet has shrunk to approximately 50 to 75% of its initial radius. Solutions for the temperature and particle/solvent concentration fields inside and outside the droplet for the different cases will be derived in the following.

2.2.1 Governing Equations

With the aforementioned assumptions the continuity equation for a spherical geometry reads:

$$\frac{\partial}{\partial r}\left(u_i r^2\right) = 0, \tag{2.1}$$

after integration Eq. 2.1 reduces to [28]:

$$u_i r^2 = f(t), \tag{2.2}$$

where u_i is the velocity of phase 1 or 2, respectively. The left hand side of Eq. 2.2 is only a function of time. The momentum equation is:

$$\frac{\partial u_i}{\partial t} + u_i \frac{\partial u_i}{\partial r} = -\frac{1}{\rho_i}\frac{\partial p_i}{\partial r} + \mu_i \left[\frac{1}{r}\frac{\partial^2 (r u_i)}{\partial r^2} - \frac{2u_i}{r^2}\right]. \tag{2.3}$$

Using Eq. 2.2, it can be shown that the viscous term in the momentum equation 2.4 vanishes for an incompressible fluid in the spherically symmetric case [30]:

$$\mu_i \left[\frac{1}{r}\frac{\partial^2 (r u_i)}{\partial r^2} - \frac{2u_i}{r^2}\right] = \mu_i f(t) \left[\frac{1}{r}\frac{\partial^2}{\partial r^2}\left(\frac{1}{r}\right) - \frac{2}{r^3}\right] = 0. \tag{2.4}$$

For the momentum equation it follows:

$$\frac{\partial u_i}{\partial t} + u_i \frac{\partial u_i}{\partial r} = -\frac{1}{\rho_i}\frac{\partial p_i}{\partial r}. \tag{2.5}$$

The nanoparticle continuity and energy equations in phase 1 are derived from Buongiorno [25]. Out of seven slip mechanisms (inertia, Brownian diffusion, thermophoresis, diffusiophoresis, Magnus effect, fluid drainage and gravity settling) Brownian diffusion and thermophoresis are the only relevant for nanoparticle transport. For the nanoparticle transport in the droplet it follows:

$$\begin{aligned}\frac{\partial \psi_{P,1}}{\partial t} + u_1 \frac{\partial \psi_{P,1}}{\partial r} = {} & D_{B,1}\left(\frac{2}{r}\frac{\partial \psi_{P,1}}{\partial r} + \frac{\partial^2 \psi_{P,1}}{\partial r^2}\right) + \frac{D_{T,1}}{T}\left(\frac{2}{r}\frac{\partial T}{\partial r} + \frac{\partial^2 T}{\partial r^2}\right) \\ & - \frac{D_{T,1}}{T^2}\left(\frac{\partial T}{\partial r}\cdot\frac{\partial T}{\partial r}\right),\end{aligned} \tag{2.6}$$

where $\psi_{P,1}$ denotes the particle volume fraction, $D_{B,1}$ the Brownian and $D_{T,1}$ the temperature dependent thermal diffusion coefficient in phase 1. Brownian diffusion and thermophoresis are described by the first term and the second and third term on the right hand side, respectively. The energy equation in phase 1 can be written as:

$$\begin{aligned}\rho_1 c_1 \left(\frac{\partial T}{\partial t} + u_1 \frac{\partial T}{\partial r}\right) = {} & \lambda_1 \left(\frac{2}{r}\frac{\partial T}{\partial r} + \frac{\partial^2 T}{\partial r^2}\right) \\ & + \rho_P c_P \left(D_{B,1}\frac{\partial \psi_{P,1}}{\partial r}\cdot\frac{\partial T}{\partial r} + D_{T,1}\frac{1}{T}\frac{\partial T}{\partial r}\cdot\frac{\partial T}{\partial r}\right) + q_s'''.\end{aligned} \tag{2.7}$$

where the second term on the right hand side accounts for thermal transport due to particle motion. The additional volumetric source term q_s''' is non-zero when the droplet is thermally heated. In the presence of a laser the particle-dependent source term is described by the Lambert-Beer law:

$$q_S''' = \kappa I_0'' \exp\left(-\kappa \psi_{P,1} \delta^S\right), \tag{2.8}$$

where δ^S is the penetration depth with respect to the position of the interface.

In phase 2 an additional equation for the toluene continuity is solved. According to [31] one can write:

$$\frac{\partial \psi_{T,2}}{\partial t} + u_2 \frac{\partial \psi_{T,2}}{\partial r} = D_{WT,2} \left(\frac{2}{r} \frac{\partial \psi_{T,2}}{\partial r} + \frac{\partial^2 \psi_{T,2}}{\partial r^2} \right). \tag{2.9}$$

Here, $\psi_{T,2}$ and $D_{WT,2}$ are the volume fraction of toluene and the constant diffusion coefficient of toluene in water. The energy equation in phase 2 is:

$$\begin{aligned} \rho_2 c_2 \left(\frac{\partial T}{\partial t} + u_2 \frac{\partial T}{\partial r} \right) = \lambda_2 & \left(\frac{2}{r} \frac{\partial T}{\partial r} + \frac{\partial^2 T}{\partial r^2} \right) \\ & + \rho_T c_T \left(D_{WT,2} \frac{\partial \psi_{T,2}}{\partial r} \cdot \frac{\partial T}{\partial r} \right). \end{aligned} \tag{2.10}$$

Again, Eq. 2.10 has an additional term to describe thermal transport due to the interdiffusion of the different species [31].

2.2.2 Velocity and Pressure Fields

To satisfy conservation of mass at the interface, the overall mass flux density to the interface in phase 1 (droplet) has to equal to the total mass flux density form the interface in phase 2 [32, 33]:

$$j_{total} = \rho_{1,IF} \left(u_1 (R) - \dot{R} \right) = \rho_{2,IF} \left(u_2 (R) - \dot{R} \right), \tag{2.11}$$

where $\dot{R}$ and $\rho_{i,IF}$ denotes the velocity of the moving interface and the corresponding density at the interface. The mass flux density of toluene at the interface is:

$$j_{T,2} = \rho_{T,2} \left(u_{T,2} (R) - \dot{R} \right), \tag{2.12}$$

with $\rho_{T,2} = \psi_{T,2}\rho_2$ being the partial density of toluene at the interface. The velocity of the toluene $u_{T,2}$, in 2.12 reads [31]:

$$u_{T,2} = u_2(R) - \frac{\rho_{2,IF}}{\rho_{T,2}} D_{WT,2} \frac{\partial}{\partial r}\left(\psi_{T,2}\frac{\rho_T}{\rho_2}\right)\bigg|_{r=R}. \tag{2.13}$$

By substituting 2.13 in 2.12 the mass flux density of toluene at the interface is derived [33]:

$$j_{T,2} = \psi_{T,2}\rho_T\left(u_2\left(R\right) - \dot{R}\right) - \rho_{2,IF} D_{WT,2} \frac{\partial}{\partial r}\left(\psi_{T,2}\frac{\rho_T}{\rho_2}\right)\bigg|_{r=R}. \tag{2.14}$$

The mass flux of particles and water at the interface is set to zero, as neither nanoparticles nor water are expected to cross the interface. The gold particles are stabilized by thiol-groups, as it was initially described by Brust et al. [34]. Due to the thiol-monolayer the gold particles become hydrophobic and only soluble in the non-polar organic toluene. The nanoink droplet, consisting of those hydrophobic nanoparticles and toluene, acts as a homogeneous non-polar and thus water-repellant system. Hence, practically no water is expected to diffuse into the nanoink drop. From an energy balance for a single particle, partially wetted by toluene and water, Levine et al. [35] concluded that particles are trapped in a deep energy well at the interface. Surface tension restricts the particles therefore to leave the nanoink droplet. An overall mass balance of the droplet states that the variation of the mass of the droplet equals the mass flux of toluene through the interface [28]:

$$\frac{d}{dt}\left(m_{total,droplet}\right) = -\dot{m}_T. \tag{2.15}$$

Only the mass of the toluene contained in the nanoink droplet changes with time. The density of the pure toluene ρ_T stays constant. In this case, the temporal variation of the volume of toluene equals the temporal variation of the total volume of the droplet:

$$\frac{dV}{dt} = \frac{d}{dt}\left(V_P + V_T\right) = \underbrace{\frac{d}{dt}\left(V_P\right)}_{=0} + \frac{d}{dt}\left(V_T\right), \tag{2.16}$$

where V_T is the Volume of the solvent. Combining equations 2.15 and 2.16,

$$\frac{dV}{dt} = \frac{d}{dt}\left(\frac{4}{3}\pi R^3\right) = -\frac{j_T}{\rho_T} 4\pi R^2, \tag{2.17}$$

one can derive the following expression for the mass flux density:

$$j_T = -\rho_T \dot{R}. \tag{2.18}$$

Substituting Eq. 2.18 into Eq. 2.14 yields an expression for the velocity at the interface in phase 2:

$$u_2(R) = \left(1 - \frac{\rho_T}{\rho_{T,2}}\right)\dot{R} + D_{WT,2}\frac{\rho_{2,IF}}{\rho_{T,2}}\frac{\partial}{\partial r}\left(\psi_{T,2}\frac{\rho_T}{\rho_2}\right)\Big|_{r=R}. \tag{2.19}$$

The combination of Eqs. 2.18, 2.19 and 2.11 results in an expression for the velocity of the interface:

$$\dot{R} = \frac{\rho_{2,IF}}{\rho_T}\frac{D_{WT,2}}{\left(1 - \psi_{T,2}\frac{\rho_T}{\rho_{2,IF}}\right)}\frac{\partial}{\partial r}\left(\psi_{T,2}\frac{\rho_T}{\rho_2}\right)\Big|_{r=R}. \tag{2.20}$$

This indicates that the velocity of the interface of the nanoink droplet only depends on the diffusion coefficient of toluene in water and the concentration gradient of toluene at the interface of the surrounding water-toluene mixture (phase 2). Substituting the velocity of the interface in Eq. 2.19 and using Eq. 2.2, an expression for the velocity field in phase 2 and phase 1 (by combining equations 2.11 and 2.20) is derived:

$$u_i(r) = \frac{R^2}{r^2}\left(1 - \frac{\rho_T}{\rho_{i,IF}}\right)\dot{R}. \tag{2.21}$$

Substituting Eq. 2.21 into the momentum equation 2.5 and accounting for the fact that the velocity of the interface is only dependent on time we obtain:

$$\frac{1}{r^2}\left(R^2\frac{d}{dt}\left(u_2(R)\right) + 2\dot{R}Ru_2(R)\right) - \frac{2u_2(R)^2R^4}{r^5} = -\frac{1}{\rho_2}\frac{\partial p_2}{\partial r} \tag{2.22}$$

Eq. 2.22 can now be integrated from the droplet interface to infinity:

$$\int_R^\infty \frac{1}{r^2}\left(R^2\frac{d}{dt}\left(u_2(R)\right)\right)dr + \int_R^\infty \frac{1}{r^2}\left(2\dot{R}Ru_2(R)\right)dr - \int_R^\infty \frac{2u_2(R)^2R^4}{r^5}dr = -\int_R^\infty \frac{1}{\rho_2}\frac{\partial p_2}{\partial r}dr. \tag{2.23}$$

The density of phase 2, ρ_2, is considered to be constant because it only changes marginally. The densities of water and toluene are in the same range and the

maximal solubility of toluene is 3.30×10^{-3}, resulting in a maximal density variation of 0.05%. For the solution for the pressure at the interface in phase 2 it follows:

$$p_2(R) = \rho_{2,IF}\left(R\frac{d}{dt}(u_2(R)) + 2u_2(R)\dot{R} - \frac{1}{2}u_2(R)^2\right) + p_\infty. \tag{2.24}$$

Evaluating Eq. 2.21 at the interface yields the interfacial pressure in phase 2:

$$p_2(R) = (\rho_{2,IF} - \rho_T)\left[\ddot{R}R + \frac{1}{2}\left(3 + \frac{\rho_T}{\rho_{2,IF}}\right)\dot{R}^2\right] + p_\infty. \tag{2.25}$$

The momentum conservation at the interface results in:

$$\rho_{1,IF}u_1(R)\left(u_1(R) - \dot{R}\right) - \rho_{2,IF}u_2(R)\left(u_2(R) - \dot{R}\right) - \tau_1 + \tau_2 - \frac{2}{R}\sigma = 0, \tag{2.26}$$

where τ_i denotes the stresses imposed on the interface. Assuming constant density and employing Eq. 2.21 we obtain at the interface in phase 1:

$$\begin{aligned} p_1 = p_2 &+ \rho_T^2\left(\frac{1}{\rho_{2,IF}} - \frac{1}{\rho_{1,IF}}\right)\dot{R}^2 \\ &+ \frac{4\dot{R}}{R}\left[\mu_2\left(1 - \frac{\rho_T}{\rho_{2,IF}}\right) - \mu_1\left(1 - \frac{\rho_T}{\rho_{1IF}}\right)\right] + \frac{2}{R}\sigma, \end{aligned} \tag{2.27}$$

where μ_i is the dynamic viscosity.

2.2.3 Boundary Conditions

Having derived explicit expressions for the velocity field, Eq. 2.21, the pressures and the velocity of the interface, Eqs. 2.20, 2.25 and 2.27, only the equations for nanoparticle transport, toluene transport and the energy equation for both liquids need to be solved numerically. In order to solve these 4 coupled equations, boundary conditions at the center of the droplet, the interface and at $r \to \infty$ are needed. For the center of the droplet the usual symmetry condition of a horizontal tangent for the temperature and the concentration profiles are applied:

$$\frac{d}{dr}(T_1)\bigg|_{r=0} = 0, \tag{2.28}$$

$$\frac{d}{dr}\left(\psi_{P,1}\frac{\rho_P}{\rho_1}\right)\bigg|_{r=0} = 0. \tag{2.29}$$

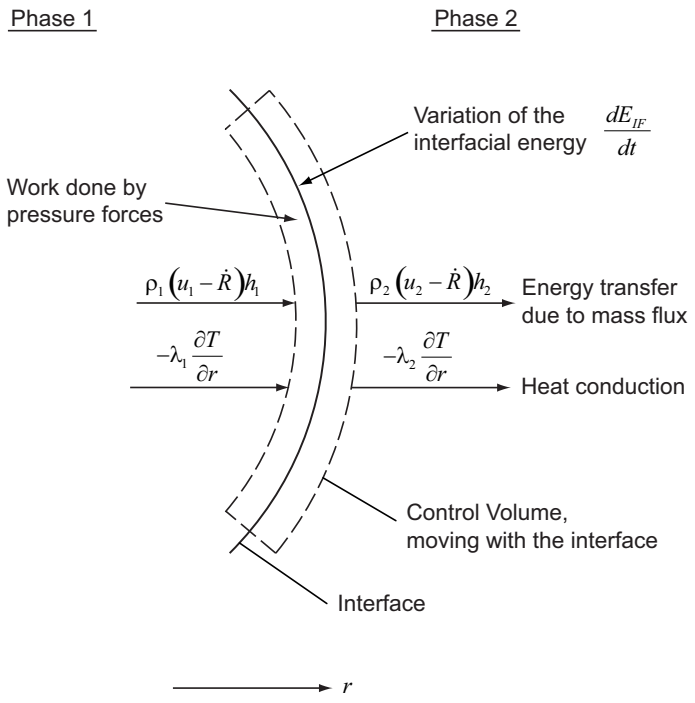

Figure 2.2: Schematic of the thermal conditions at the liquid-liquid interface.

For the temperature and the concentration at the domain boundary ($r \to \infty$) the following conditions are employed:

$$\frac{d}{dr}\left(T_2\right)\Big|_{r\to\infty} = 0, \tag{2.30}$$

$$\frac{d}{dr}\left(\psi_{T,2}\frac{\rho_T}{\rho_2}\right)\Big|_{r\to\infty} = 0. \tag{2.31}$$

The boundary conditions at the moving interface are more involved. The interface is assumed at every instant of the process to be in local thermal quasi-equilibrium, because the convective and diffusive time scales are large compared to the timescale required to reach local quasi-equilibrium. This implies that the temperature on both sides of the interface is the same (no contact resistance):

$$T_1(R) = T_2(R). \tag{2.32}$$

The second thermal condition can be derived from an overall energy balance of the interface, see Figure 2.2. Thermal boundary conditions for two-phase flows with a

moving interface and mass flux through the interface can be found in [32, 33, 36]. They differ in the assumptions adopted and, therefore, in complexity. Herein, the temporal variation of the interfacial energy is equal to the imbalance in energy transfer due to mass flux over the interface, heat conduction and the work done by pressure forces per unit time:

$$\begin{aligned}\frac{dE_{IF}}{dt} = \frac{d}{dt}\left(\sigma A\right) = \rho_{2,IF} A \left(u_2(R) - \dot{R}\right)\left(h_1 - h_2\right) \\ + \lambda_2\, A \frac{\partial T}{\partial r}\bigg|_{r=R} - \lambda_1 A\, \frac{\partial T}{\partial r}\bigg|_{r=R} + p_1 A\dot{R} - p_2 A\dot{R}.\end{aligned} \tag{2.33}$$

In Eq. 2.33 the enthalpy h is used to account for the flow work, i.e. the energy required to push (extract) mass into (from) the interface. The last two terms on the right hand side account for the volumetric work per unit time needed to move the interface with a velocity $\dot{R}$ against a pressure difference. Dissipation, kinetic energies and the influence of the heat of solution (the amount of transferred mass is very low) are neglected. Substituting $h_i = e_i + \frac{p_i}{\rho_i}$, with e_i as the internal energy, and $\rho_2\left(u_2(R) - \dot{R}\right) = -\rho_T \dot{R}$ results in:

$$\begin{aligned}\dot{\sigma} + \sigma\frac{2\dot{R}}{R} = -\rho_T \dot{R}\left(e_{T,1} - e_{T,2}\right) + \left(1 - \frac{\rho_T}{\rho_{1,IF}}\right)\dot{R}\, p_1 \\ - \left(1 - \frac{\rho_T}{\rho_{2,IF}}\right)\dot{R}\, p_2 + \lambda_2 \frac{\partial T}{\partial r}\bigg|_{r=R} - \lambda_1 \frac{\partial T}{\partial r}\bigg|_{r=R}.\end{aligned} \tag{2.34}$$

Only the internal energy of the toluene, e_T, is taken into account, because it is the only species traveling over the interface. Considering that the internal energy of the toluene does not change during the transport over the interface ($e_{T,1} = e_{T,2}$) as the interface is in local thermal equilibrium and with the help of Eq.2.21 one can write for the heat flux boundary condition:

$$\dot{\sigma} = u_1(R)p_1 - u_2(R)p_2 + \lambda_2 \frac{\partial T}{\partial r}\bigg|_{r=R} - \lambda_1 \frac{\partial T}{\partial r}\bigg|_{r=R} - \sigma\frac{2\dot{R}}{R}. \tag{2.35}$$

The volumetric concentration at the interface is set equal to the solubility of toluene ϕ_T in water which is temperature dependent.

$$\psi_{T,2}\left(R\right) = \phi_T\left(T_2\right). \tag{2.36}$$

In addition, one has to ensure that the mass flux of toluene from phase 1 to the interface is the same as the mass flux from the interface into phase 2 (no mass accumulation at the interface possible). An equivalent but simpler condition is to set the mass flux of nanoparticles across interface to zero since the nanoparticles do not diffuse over the interface into phase 2. With the help of Eq. 2.21 this leads to:

$$\begin{aligned} D_B \left.\frac{\partial \psi_{P,1}}{\partial r}\right|_{r=R} + D_B \psi_{P,1} \frac{\rho_{1,IF}}{\rho_P} \left.\frac{\partial}{\partial r}\left(\frac{\rho_P}{\rho_1}\right)\right|_{r=R} \\ = -\psi_{P,1}\frac{\rho_T}{\rho_{1,IF}}\dot{R} - \frac{\rho_{1,IF}}{\rho_P} D_T \frac{1}{T} \left.\frac{\partial T}{\partial r}\right|_{r=R}. \end{aligned} \tag{2.37}$$

It should be emphasized that the second term on the left hand side of Eq. 2.37 accounts for the variation of the bulk density ρ_1 at the interface, which is not negligible. In all other equations spatial density changes are very low and can be neglected.

2.3 Numerical Method

The energy equations, 2.7, 2.10, and the species conservation Equations, 2.6, 2.9, can now be solved with respect to the boundary conditions (2.27, 2.30, 2.35-2.37) as well as the symmetry condition at the origin. One obtains a solution for the temperature field as well as the particle and toluene concentration fields within the droplet (phase 1) and the surrounding water (phase 2), respectively. Knowing the concentration fields, the interface velocity and location can be computed in a second step with Eq. 2.20.

The following dimensionless concentration, time, radial coordinate, temperature, pressure and position of the interface are introduced for the numerical simulation:

$$\begin{aligned} &\varphi_i = \frac{\psi_i}{\psi_0}; \quad \tau = \frac{D_0 t}{R_0^2}; \quad x = \frac{r}{R_0}; \quad \theta_i = \frac{T_i - T_\infty}{\Delta T} \\ &X = \frac{R}{R_0}; \quad \wp = \frac{p R_0^2}{\rho_W D_0^2}. \end{aligned} \tag{2.38}$$

ψ_0 ,R_0 ,D_0 ,ΔT are the initial concentration of toluene at the interface, the initial position of the interface, the diffusion coefficient of toluene in water and a reference

temperature difference, respectively. X is the non-dimensional position of the moving interface. In order to facilitate the numerical solution of the moving boundary problem, a new coordinate system with fixed spatial boundaries is introduced. The transformation was initially proposed by Landau [29] and since then it was widely used in problems involving moving boundaries in a spherically symmetric setup, e.g. [37–40]. The Landau-coordinates are:

$$\eta_1(x,\tau) = \frac{x}{\delta_1(\tau)} = \frac{x}{X(\tau)} \quad \eta_2(x,\tau) = \frac{x - X(\tau)}{\delta_2(\tau)} = \frac{x - X(\tau)}{X_\infty - X(\tau)}, \tag{2.39}$$

with the time dependent position of the moving interface $X(\tau)$ and thickness of phase 1 and 2, $\delta_1(\tau)$ and $\delta_2(\tau)$, respectively. The two phases are now defined as:

$$\text{Phase 1: } 0 \leq \eta_1 \leq 1 \quad \text{Phase 2: } 0 \leq \eta_2 \leq 1.$$

Although the Landau transformation introduces more complexity in the governing equations it has the advantage that standard numerical discretization techniques can be employed. The energy equations for phases 1 and 2 are:

$$\begin{aligned}\frac{\partial\theta_1}{\partial\tau} = &\left[\frac{\eta_1\dot{X}}{X} - \left(1 - \frac{\rho_T}{\rho_1}\right)_{r=R}\frac{\dot{X}}{\eta_1^2 X} + \frac{\lambda_1}{D_0\rho_1 c_1}\frac{2}{\eta_1 X^2}\right]\frac{\partial\theta_1}{\partial\eta_1} \\ &+ \frac{\rho_P c_P}{\rho_1 c_1}\frac{D_{B,1}\psi_0}{D_0}\frac{\partial\varphi_{P,1}}{\partial\eta_1}\frac{1}{X^2}\frac{\partial\theta_1}{\partial\eta_1} \\ &+ \frac{\rho_P c_P}{\rho_1 c_1}\frac{D_{T,1}}{D_0}\frac{\Delta T}{(\theta_1\Delta T + T_\infty)}\frac{1}{X^2}\frac{\partial\theta_1}{\partial\eta_1}\frac{\partial\theta_1}{\partial\eta_1} \\ &+ \frac{\lambda_1}{D_0\rho_1 c_1}\frac{1}{X^2}\frac{\partial^2\theta_1}{\partial\eta_1^2} + \frac{R_0^2}{D_0}\frac{1}{\rho_1 c_1}\frac{q_s}{\Delta T}\end{aligned} \tag{2.40}$$

$$\begin{aligned}\frac{\partial\theta_2}{\partial\tau} = &\left[\frac{(1-\eta_2)\,\dot{X}}{\delta_2} - \left(1 - \frac{\rho_T}{\rho_2}\right)_{r=R}\frac{X^2\dot{X}}{(\eta_2\delta_2 + X)^2\,\delta_2}\right]\frac{\partial\theta_2}{\partial\eta_2} \\ &+ \left[\frac{\lambda_2}{D_0\rho_2 c_2}\frac{2}{(\eta_2\delta_2 + X)\,\delta_2} + \frac{\rho_T c_T}{\rho_2 c_2}\frac{D_{WT,2}\psi_0}{D_0}\frac{1}{\delta_2^2}\frac{\partial\varphi_{T,2}}{\partial\eta_2}\right]\frac{\partial\theta_2}{\partial\eta_2} \\ &+ \frac{\lambda_2}{D_0\rho_2 c_2}\frac{1}{\delta_2^2}\frac{\partial^2\theta_2}{\partial\eta_2^2}.\end{aligned} \tag{2.41}$$

The equations for particle transport in the nanoink droplet (phase 1) and toluene transport in the surrounding fluid (phase 2) are:

$$\begin{aligned}\frac{\partial \varphi_{P,1}}{\partial \tau} &= \left[\frac{\eta_1 \dot{X}}{X} - \left(1 - \frac{\rho_T}{\rho_1}\right)_{r=R} \frac{\dot{X}}{\eta_1^2 X}\right] \frac{\partial \varphi_{P,1}}{\partial \eta_1} + \frac{D_{B,1}}{D_0} \frac{2}{\eta_1 X^2} \frac{\partial \varphi_{P,1}}{\partial \eta_1} \\ &+ \frac{D_{B,1}}{D_0} \frac{1}{X^2} \frac{\partial^2 \varphi_{P,1}}{\partial \eta_1^2} + \frac{\Delta T}{(\theta_1 \Delta T + T_\infty)} \frac{D_{T,1}}{D_0 \psi_0} \frac{2}{X^2 \eta_1} \frac{\partial \theta_1}{\partial \eta_1} \\ &+ \frac{\Delta T}{(\theta_1 \Delta T + T_\infty)} \frac{D_{T,1}}{D_0 \psi_0} \frac{1}{X^2} \frac{\partial^2 \theta_1}{\partial \eta_1^2} - \frac{(\Delta T)^2}{(\theta_1 \Delta T + T_\infty)^2} \frac{D_{T,1}}{D_0 \psi_0} \frac{1}{X^2} \left(\frac{\partial \theta_1}{\partial \eta_1}\right)^2,\end{aligned} \tag{2.42}$$

$$\begin{aligned}\frac{\partial \varphi_{T,2}}{\partial \tau} &= \left[\frac{(1-\eta_2)\,\dot{X}}{\delta_2} - \left(1 - \frac{\rho_T}{\rho_2}\right)_{r=R} \frac{X^2 \dot{X}}{(\eta_2 \delta_2 + X)^2\, \delta_2}\right] \frac{\partial \varphi_{T,2}}{\partial \eta_2} \\ &+ \frac{D_{WT,2}}{D_0} \frac{2}{(\eta_2 \delta_2 + X)\, \delta_2} \frac{\partial \varphi_{T,2}}{\partial \eta_2} + \frac{D_{WT,2}}{D_0} \frac{1}{\delta_2^2} \frac{\partial^2 \varphi_{T,2}}{\partial \eta_2^2}.\end{aligned} \tag{2.43}$$

These equations are not only coupled through the concentration and temperature dependent terms in the energy equations and species conservation, but also through the boundary conditions at the interface which are:

$$\varphi_{T2,1} = \varphi_0(T) \tag{2.44}$$

and

$$\begin{aligned}\left.\frac{\partial \varphi_{P,1}}{\partial \eta_1}\right|_{\eta_1=1} &= \varphi_{P,1} \left(-\frac{D_0}{D_B} \frac{\rho_T}{\rho_1} \dot{X}\, X + \frac{1}{\rho_1} \frac{\partial \rho_1}{\partial \eta_1}\right)_{\eta_1=1} \\ &- \frac{D_T}{D_B} \frac{\rho_1}{\rho_P} \frac{1}{\psi_0} \frac{\Delta T}{(\theta\, \Delta T + T_\infty)} \left.\frac{\partial \theta_1}{\partial \eta_1}\right|_{\eta_1=1}.\end{aligned} \tag{2.45}$$

for the concentration equations. The transformed interfacial boundary conditions for the energy equation are:

$$\theta_2(\eta_2 = 0) = \theta_1(\eta_1 = 1) \tag{2.46}$$

and

$$\begin{aligned}\left.\frac{\partial \theta_1}{\partial \eta_1}\right|_{\eta_1=1} &= \frac{\lambda_2}{\lambda_1} \frac{X}{\delta_2} \left.\frac{\partial \theta_2}{\partial \eta_2}\right|_{\eta_2=0} + \left[\left(1 - \frac{\rho_T}{\rho_1}\right) \wp_1 - \left(1 - \frac{\rho_T}{\rho_2}\right) \wp_\infty\right] \frac{X D_0^2}{\rho_w R_0^2} \frac{D_0}{\Delta T} \frac{\dot{X}}{\lambda_1} \\ &- \frac{1}{\lambda_1} \frac{X}{\Delta T} \frac{D_0}{R_0} \frac{d\sigma}{d\tau} - \frac{\sigma}{\lambda_1} \frac{2}{R_0} \frac{D_0}{\Delta T} \dot{X},\end{aligned} \tag{2.47}$$

where $\frac{d\sigma}{d\tau}$ is the temporal variation in surface tension. The pressure at the interface $\wp_1$ is calculated as follows:

$$\begin{aligned}\wp_1 = \wp_\infty + \left(\frac{1}{\rho_2} - \frac{1}{\rho_1}\right)\frac{\rho_T^2}{\rho_W}\dot{X}^2 \\ + \frac{4}{X}\frac{1}{\rho_W D_0}\dot{X}\left(\mu_2\left(1 - \frac{\rho_T}{\rho_2}\right) - \mu_1\left(1 - \frac{\rho_T}{\rho_1}\right)\right) + \frac{2R_0\sigma}{X\rho_W D_0^2}.\end{aligned} \tag{2.48}$$

The velocity and the position of the interface are updated according to:

$$\dot{X} = \left[\frac{D_{WT,2}}{D_0}\frac{\psi_0}{\left(1 - \frac{\rho_T}{\rho_2}\varphi_{T,2}\psi_0\right)}\frac{1}{\delta_2}\frac{\partial\varphi_{T,2}}{\partial\eta_2}\right]_{\eta_2=0} \tag{2.49}$$

and

$$\frac{dX}{d\tau} = \dot{X}. \tag{2.50}$$

The concentration and temperature fields are numerically solved by means of a finite difference scheme with uniform grid spacing. For the convective and diffusive terms a second order central differencing scheme is used. Fictitious nodes are introduced at the boundaries to allow for order consistency [41]. An implicit Euler scheme is used for the discretization in time of the concentration and temperature fields. The position of the interface is updated employing a fourth order Adams-Bashforth scheme [42]. The coupled equations are solved iteratively. In every time step the procedure is:

1. Solution of the toluene concentration in the surrounding water (phase 2), Eq. 2.43 with 2.44 as boundary conditions at the interface.

2. Calculation of the velocity of the interface and update of the new position of the interface, Eqs 2.49 and 2.50.

3. Solution of the temperature field in the nanoink droplet (phase 1) and phase 2, Eqs 2.40 and 2.41. These equations are coupled through the thermal boundary conditions 2.46 and 2.47.

4. Solution of the nanoparticle concentration in the droplet (phase 1), 2.42 with boundary condition 2.45.

The iteration within every time step is executed until the residuals are below a certain limit (max. 10^{-14}).

The simulation program was thoroughly validated in test cases. Results of calculations with a fixed droplet radius and the absence of thermophoresis and Brownian diffusion were compared with analytical solutions and showed excellent agreement. The analytical solutions for the equation of thermal conduction for a sphere (phase 1) and a hollow spherical body (phase 2) with constant boundary conditions can be found in the textbook by Carslaw and Jaeger [43]. Overall mass conservation was monitored throughout all calculations, showing practically no mass leakage. Values of the error are in the range between 5.71×10^{-5} and 4.10×10^{-3} for the isothermal and the non-isothermal case, respectively. Grid independence was ensured in parametric studies, resulting in an optimal number of 200 grid points for both phases. Further results of the validation can be found in Appendix A. The time step is varied throughout the calculation depending on the convergence rate, with a maximal time step size of 1.0×10^{-3}. The calculated position of the interface was compared to an analytical solution, derived from Eq. 2.25 by assuming constant pressure p_∞ and density in phase 2. With $p_2 = p_\infty$ Eq. 2.25 reduces to:

$$0 = (\rho_2 - \rho_T) \left[\ddot{R}R + \frac{1}{2} \left(3 + \frac{\rho_T}{\rho_2} \right) \dot{R}^2 \right]. \tag{2.51}$$

With

$$n = \frac{1}{2} \left(3 + \frac{\rho_T}{\rho_2} \right) \tag{2.52}$$

and the substitution $g = \dot{R} = \frac{dR}{dt}$ as well as $\frac{d^2R}{dt^2} = g\frac{dg}{dt}$ it follows:

$$g \frac{dg}{dR} R + ng^2 = 0. \tag{2.53}$$

After integration one obtains:

$$\frac{\dot{R}}{\dot{R}_0} = \left(\frac{R}{R_0} \right)^{-n}. \tag{2.54}$$

This yields the following expression for the position of the interface in dimensionless coordinates:

$$X = X_0 \left(\frac{\dot{X}_0}{\dot{X}} \right)^{1/n}, \tag{2.55}$$

with $n = 0.5\,(3 + \rho_T/\rho_2)$.

2.4 Results and Discussion

Calculations were performed using typical values for density, conductivity and viscosity for the pure components [44]. Density, heat capacity, viscosity and thermal conductivity of the nanoink (phase 1) and the water-toluene mixture (phase 2) were calculated using standard mixture laws [25]. The interfacial tension was estimated by comparing own measurements of the surface tension of nanoink-air with literature values of the surface tension of water-air and water-toluene [45, 46]. The measured surface tension of nanoink lies in the same range as the surface tension of toluene. To obtain values for the interfacial tension of nanoink-water, these values were compared to those of toluene-water.

The initial volume fraction of gold nanoparticles in the droplet was set to 1% for all cases. The concentration of toluene in water (phase 2) was initially set to zero, with the maximal temperature-dependent solubility of toluene in water as a boundary condition at the interface. This jump condition in the numerical model, theoretically causing an infinite interface velocity at the beginning, is smoothed out during the calculations. Values of the solubility of toluene are ranging from 3.05×10^{-4} to 3.30×10^{-3} per volume, depending on the initial temperature of the interface (for 0° to 80 °Celsius) [27]. In a first step, isothermal conditions were applied and the radius of the outer phase was varied. In the non-isothermal conditions, either the temperature of the surrounding water was set to a higher value than the one of the droplet, or the nanoink droplet was heated. The radius of the droplet was initially set to $X_0 = 1$ with zero velocity.

The shrinking process of the droplet was investigated for different domain sizes and thermal conditions. First, isothermal calculations were performed, where the diffusive processes inside and outside the droplet were investigated for different thick-

nesses X_∞ of phase 2 (cases 1 to 3). The thickness of the domain was varied between 10 and 40-times of the initial droplet radius X_0, Table 2.1.

Table 2.1: Initial temperature of phase 2, $T_{2,0}$, extension of phase 2, X_∞, and the source term for thermal heating or laser heating of phase 1, q'''_S and I''_0. The isothermal standard case 2 is marked in bold. The time to shrink the droplet to 75% of its original radial extension τ_{75} is given in the last column. The initial temperature of phase 1, $T_{1,0}$, was set to 20° Celsius throughout all calculations.

Case	$T_{2,0}$ (°C)	X_∞ (-)	q'''_S ($\mathrm{W\,m^{-3}}$)	I''_0 ($\mathrm{W\,m^{-2}}$)	τ_{75} (-)
1	20	10	-	-	-
2	**20**	**20**	**-**	**-**	**442**
3	20	40	-	-	409
4	50	20	-	-	163
5	60	20	-	-	114
6	70	20	-	-	80
7	20	20	1.0×10^{10}	-	217
8	20	20	1.5×10^{10}	-	146
9	20	20	-	2.0×10^{5}	168

It can be seen that the time to shrink a nanoink droplet can be lowered slightly when the domain size is doubled (case 2 compared to case 3). In case 1 the domain extension is too small to allow for the shrinking of the droplet within a reasonable time. A restriction of the domain size is, strictly speaking, not valid for the non-isothermal calculations. In these cases, a solution of the pressure field in phase 2 (Eq. 2.24) is needed, which in turn requires an infinite boundary. However, if the thickness of the phase 2 remains larger than the classical expression for the diffusion length, $x_D = 2\sqrt{D_{WT}/D_0\tau}$ throughout the process, the artificial limitation of the domain will have, even in the non-isothermal cases, only a minor effect. It has to be noted that this length also determines the minimal distance nanoink droplets have to have if equations formulated in the spherical symmetric coordinate system are to

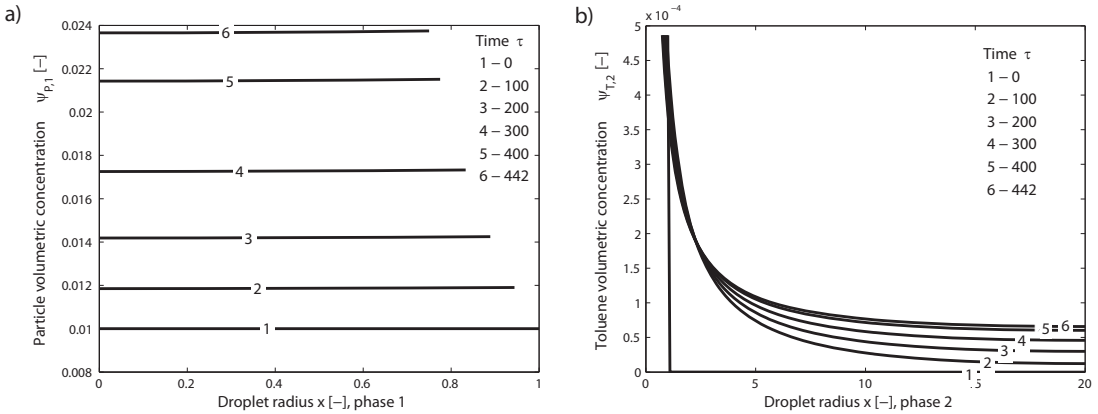

Figure 2.3: Radial particle and toluene volume fraction for different τ in the isothermal case 2. a) Particle volume fraction in phase 1 vs. droplet radius b) Toluene volume fraction in phase 2 vs. droplet radius.

remain valid.

The concentration fields of the nanoparticles within the droplet for an isothermal case (case 2) are given in Figure 2.3a as a function of the non-dimensional coordinate x . Calculations were performed until the droplet shrank to 75% of its initial radius. At this point, the peak concentration of particles in the droplet reaches about 2.4% in volume. The non-linear increase in nanoparticle concentration results from the spherical shape of the nanoink droplet. However, the concentration profile along the radial coordinate is practically uniform. In Figure 2.3b results are shown for the toluene concentration in the adjacent water (phase 2). The concentration profiles exhibit steep gradients at the interface, in particular at the beginning of the process ($\tau = 0$). These gradients are smoothed out during the diffusion process of the toluene into the water. The toluene concentration in the water rises gradually with time. Non-zero values of concentration at the outer boundary $x = 20$ indicate that an increase in domain extension would allow the water to absorb more toluene, resulting in a faster shrinkage.

In a second step the temperature in the second phase (water) was initially set to

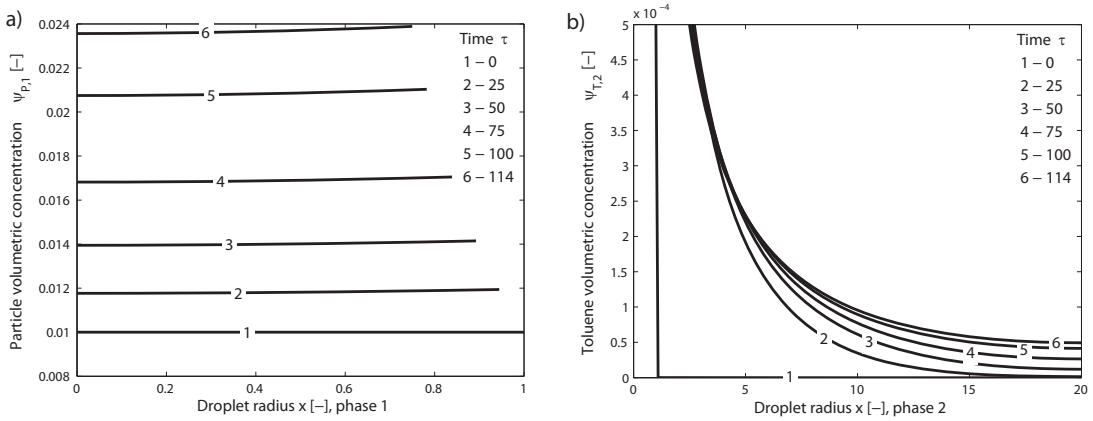

Figure 2.4: Radial particle and toluene volume fraction for different τ in the non-isothermal case 5 ($T_{2,0} = 60°C$). a) Particle volume fraction in phase 1 vs. droplet radius b) Toluene volume fraction in phase 2 vs. droplet radius.

a higher value than the one in the nanoink droplet, with values for $T_{2,0}$ ranging from 50 to 70 °C (cases 4 to 6). This is followed by cases where the droplet was heated with a constant heat source of 1×10^{10} and $1.5 \times 10^{10}\,\mathrm{W\,m^{-3}}$) (case 7 and 8). This corresponds to 9 and 13.5 mW for the entire volume of the droplet. Finally the droplet was treated with a laser (case 9). In this case the laser intensity I_0'' was set to $2.0 \times 10^5\,\mathrm{W\,m{-}2}$. In the last three cases, the amount of thermal energy was chosen such that the temperature of the droplet stays well below the boiling temperature of toluene. The initial conditions are listed in Table 2.1.

The concentration profiles for the non-isothermal case 5 are depicted in Figure 2.4. Here, the nanoink droplet is initially at 20 °C and is surrounded by water with a temperature of 60 °C. After $\tau = 114$ the droplet diameter is reduced to 75% of its initial value. Due to the velocity increase of the moving interface (compared to the isothermal case), the particle concentration rises slightly in the vicinity of the interface, Figure 2.4a. Higher solubility of toluene at the interface results in an increased toluene concentration at the interface compared to the isothermal case 2 (1.8‰ instead of 0.5‰) and a faster diffusion of toluene into the water phase. This is directly connected to an increase in interfacial velocity and an augmentation of

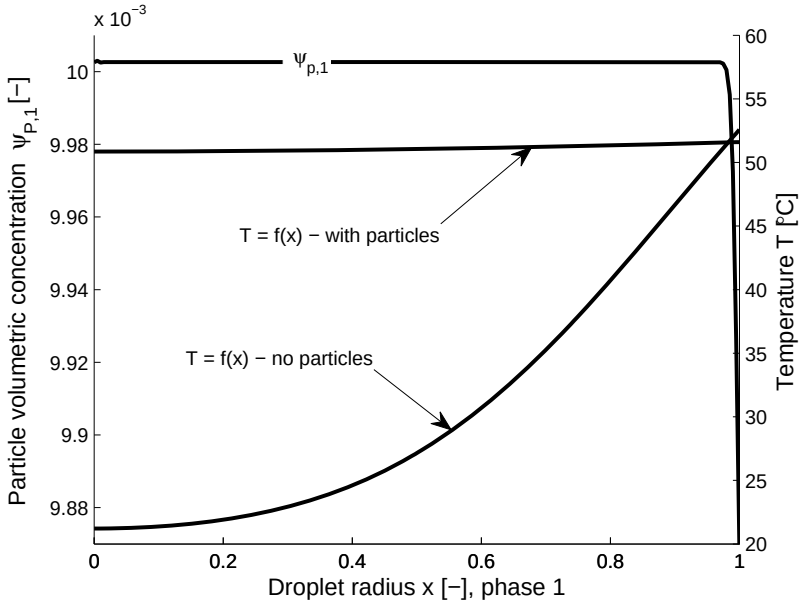

Figure 2.5: Temperature in the nanoink droplet and its surrounding phase at the beginning of the calculation,$\tau = 4.6 \times 10^{-4}$ with and without nanoparticles in the droplet.

the shrinking process by a factor of 4.

The temperature in the nanoink droplet and its surrounding phase at the beginning of the calculation ($\tau = 4.6 \times 10^{-4}$) is depicted in Figure 2.5 for two different scenarios: A droplet including nanoparticles (case 5) and a droplet consisting of pure toluene. One can identify only a slight temperature difference of 1 K from the center of the droplet to the interface if nanoparticles are present. Hence, the temperature in the nanoink droplet is already equilibrated at this point. In the case where no nanoparticles are present, the initially steep gradient still prevails with temperature values from 22° to 53 °C. The thermal relaxation time in the presence of nanoparticles is significantly lower, emphasizing the importance of nanoparticles in enhancing the thermal transport. The nanoparticle concentration is plotted in Figure 2.5 as well, showing a gradient of the concentration at the interface. Under the influence of the thermal gradient between the surrounding phase and the droplet, the particles

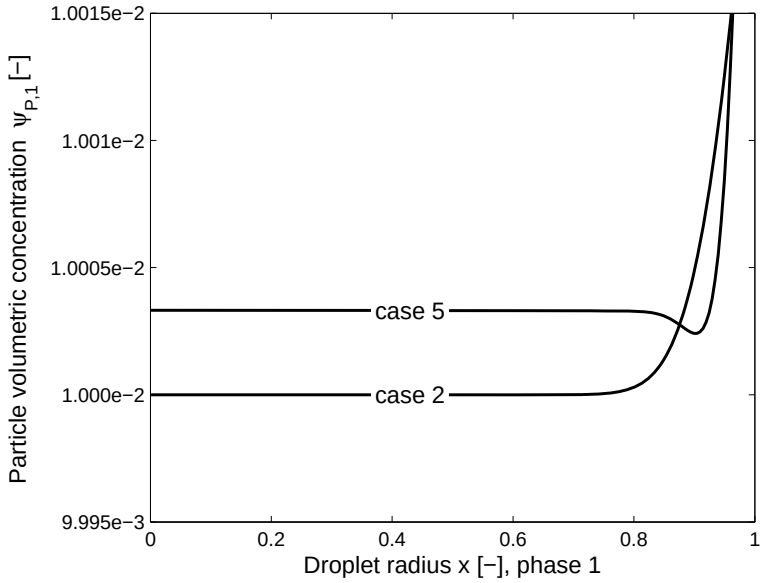

Figure 2.6: Particle Volume fraction in phase 1 for the isothermal and the non-isothermal case (case 2 and 5 respectively) at $\tau = 0.02$.

experience a thermophoretic force, pushing them toward the colder regions of the droplet. This effect is sufficiently strong such that the particle concentration decays towards the interface. The particle concentration is slightly increased towards the center of the droplet, to compensate for this effect.

In Figure 2.6, the particle concentration shortly after the initiation of the process ($\tau = 0.02$) is plotted for the isothermal and the non-isothermal cases (case 2 and 5 respectively). Two effects can be identified. The receding motion of the interface and the toluene diffusion through the interface result in an accumulation of particles at the interface. This effect can bee seen for both cases. In the non-isothermal case, however, a dent can be observed in the vicinity of the interface ($x = 0.93$). This is a result of the initially strong thermophoretic force, mentioned above.

The nanoparticle concentration and the temperature distributions in a heated nanoink droplet (case 7) are shown in Figure 2.7 for different times. The droplet is heated with a constant heat source $q_S = 10^{10}\,\mathrm{W\,m^{-3}}$, corresponding to 9 mW for the entire

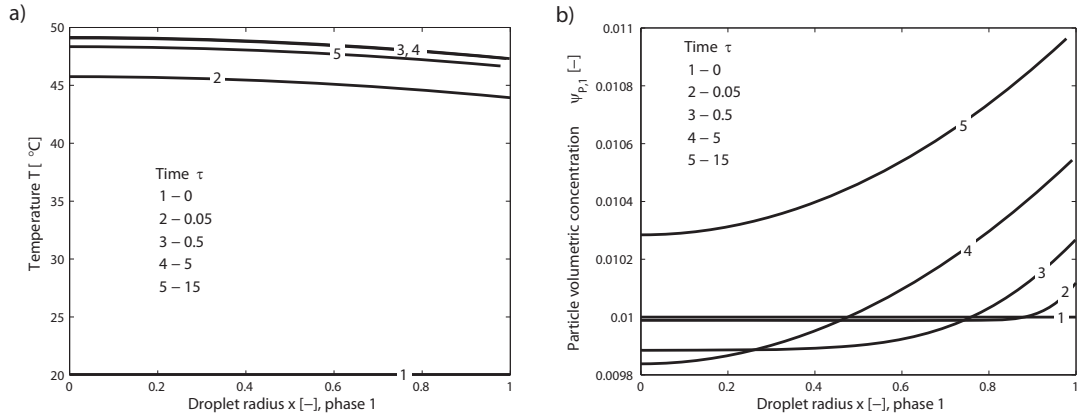

Figure 2.7: Radial particle volume fraction and temperature distribution, when the droplet is thermally heated (case 7). a) Particle volume fraction in phase 1 vs. droplet radius b) Temperature field in phase 1 vs. droplet radius.

volume of the droplet. This value was chosen to keep the temperature below the boiling temperature of toluene. The temperature rises rapidly at the beginning of the process to about 48 °C and drops slightly for later times ($\tau > 15$). The particle concentration is plotted in Figure 2.7b revealing a strong gradient from the center of the droplet towards the interface. This gradient is caused by two different phenomena. On the one hand, the nanoparticles accumulate at the interface due to the receding motion of the interface. On the other hand, the particles react on the thermophoretic force, pushing them towards the colder interface. In this situation, the effect of thermophoresis surpasses the counteracting Brownian diffusion, tending to smooth out strong concentration gradients.

In Figure 2.8 similar profiles are depicted for the case when the water is heated with a laser (case 9). Here the laser light absorption is dependent on the particle concentration and the penetration depth with respect to the interface, as stated in 2.8. The particle concentration still exhibits a gradient towards the interface. Contrary to the case when the droplet is heated with a constant heat source (cases 7 and 8) this gradient is less step.

Figure 2.9 shows the velocity of the interface for the different cases; negative values

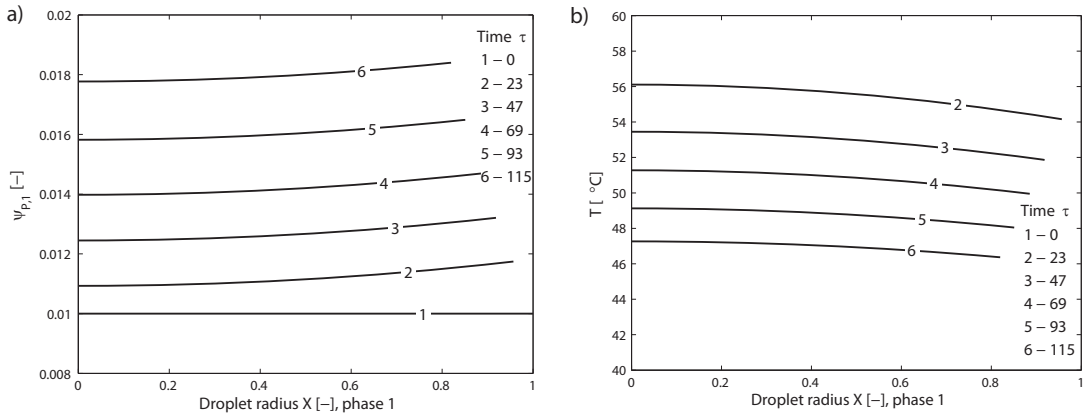

Figure 2.8: Evolution of the concentration field (a) and the temperature field (b) for phase 1 when the droplet is heated with a laser.

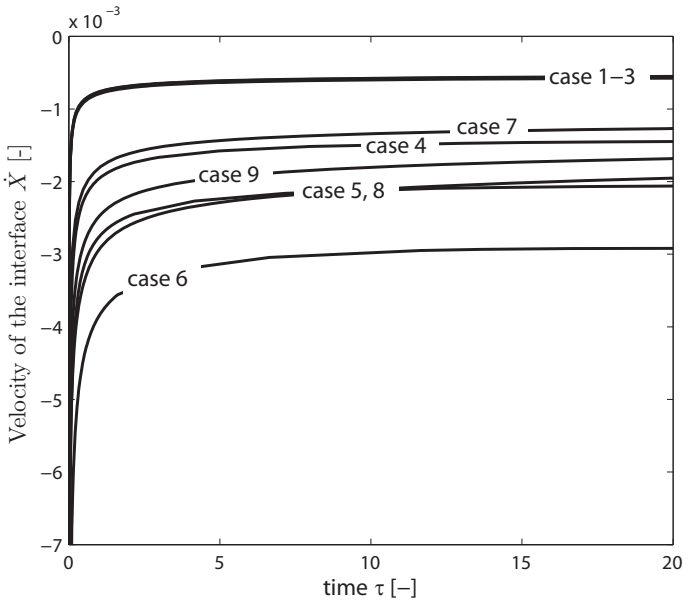

Figure 2.9: Temporal variation of the velocity of the interface for different cases.

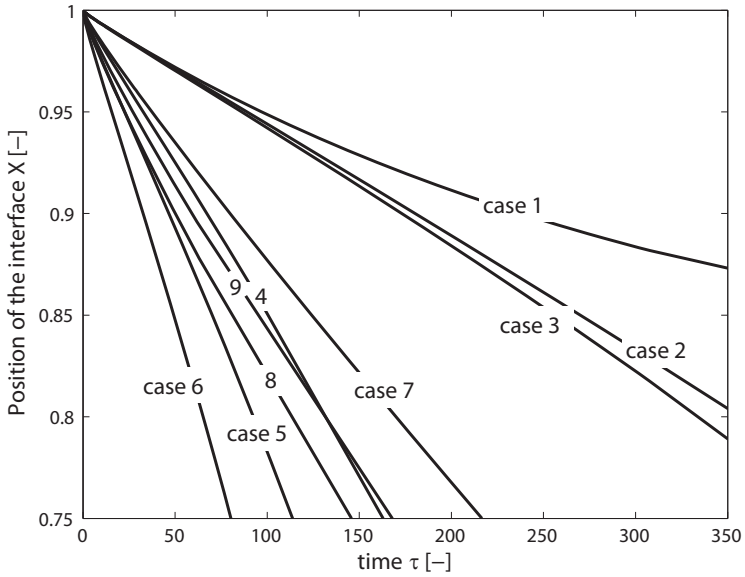

Figure 2.10: Temporal evolution of the droplet radius for different cases.

of the velocity indicate shrinkage of the nanoink droplet. The absolute value of the velocity is at the beginning of the process quite high which is a result of the steep concentration gradient at the interface as suggested by Eq. 2.20. Initial peak values of -1.4 $\times 10^{-2}$ to -7.0 $\times 10^{-3}$ are reached. The absolute value of the velocity decays rapidly and after $\tau = 5$ it is nearly constant. At this stage of the process the absolute values for the non-isothermal cases are an order of magnitude higher compared to the ones obtained in the isothermal case (3×10^{-3} compared to 3×10^{-4}) and show a clear difference, depending on the initial temperature of phase 2 (case 3 to 6). In the case of a heated droplet (case 7-9) the velocity is still higher than in the isothermal case. A clear difference in the velocity values for the isothermal cases cannot be detected.

In Figure 2.10 the position of the interface vs. time is depicted for the different cases. It can be seen that the time required to shrink a nanoink droplet can be reduced by 50 to 80% depending on the initial temperature of the surrounding phase. To exemplify, it takes 5 times longer until the droplet shrinks to 75% of its original radius in case 2 (isothermal) compared to case 6 (water is initially at 70 °C). When

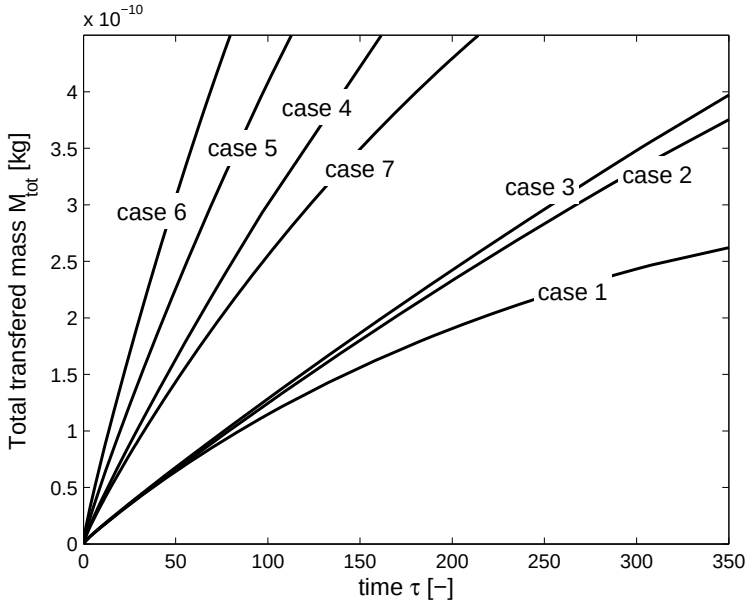

Figure 2.11: Total mass transferred over the interface as a function of dimensionless time τ for cases 1 - 7.

the nanoink droplet is heated (case 7) the shrinkage time can be lowered by a factor of 2 compared to case 2. The shrinkage times are also listed in the last column of Table 1. The rate of radial decrease in Figure 2.10 is nearly linear in the cases 2 to 9. In case 1 ($X_0 = 10$) the behavior is non-linear. In this case the extent of phase 2 is limited to only 10 times of the initial radius. This means that the toluene accumulation in the water phase reaches a level where the concentration gradients and therefore the toluene transport rate are decreasing significantly. Hence, the further toluene transport away from the interface is not taking place effectively.

The total amount of toluene diffused over the interface is plotted in Figure 2.11 as a function of time. It can be seen that the mass transfer is accelerated by a factor of 2 to 5 in cases where the water is initially set to a higher temperature or where the droplet is heated (cases 4 to 7). Therefore, an initial water temperature of 70 °C gives the best performance, but a temperature of 50 °C or heating the droplet still accelerate the shrinking process significantly. An increased mass transfer compared to the isothermal cases is directly related to the higher solubility of toluene

in water. As mentioned above, another possibility to increase the mass transfer and the amount of toluene absorbed by the water is to increase the thickness X_∞ of the surrounding water layer (cases 1 to 3). However, this is only possible to a certain extent. Whereas an improvement can still be seen between case 1 and case 2 ($X_0 = 10, 20$ respectively), the difference in total transferred mass between case 2 and case 3 ($X_0 = 40$) is marginal, indicating that only for values of $X_\infty > 20$ the condition of an infinite phase 2 is fulfilled in the numerical calculations. The diffusion length for the non-isothermal cases lies in the range of $x_D = 20$. For higher values of X_∞ the amount of toluene absorbed in the water would not increase.

2.5 Conclusions

In order to investigate the shrinking process of a nanoink droplet surrounded by water, a symmetric model was derived in this chapter a spherical .

At first, the extent of the outer phase was varied between 10 and 40-times of the initial droplet radius whereas the temperature was kept constant. It was seen that the extent of the outer phase has an effect on the shrinking dynamics if the thickness of the outer phase becomes smaller than the relevant diffusion length.

The outer phase was then set to an initial temperature in the range between 50 to 70 °C and the strong effect of the thermal energy on the shrinking was demonstrated. It was seen that the shrinking process is directly connected to the increasing solubility of toluene with temperature and the concentration gradient at the interface with the surrounding water (phase 2). Hence, the shrinkage can be significantly accelerated by heating the surrounding phase. The velocity of the interface was found to increase by a factor of 2-3 and the shrinkage time could be reduced by 50-80%, compared to isothermal conditions.

When the nanoink droplet is heated, the shrinkage time can be reduced by a factor of 2 to 3 compared to the isothermal case. For laser heating similar shrinkage

times could be detected. In the presence of a heat source a strong gradient of particle concentration was detected near the interface, which was mainly caused by the thermophoretic force, pushing the particles towards the colder interface. In this situation thermophoresis dominates over the counteracting Brownian diffusion which typically smoothes out strong concentration gradients.

The influence of thermophoresis and Brownian diffusion of nanoparticles on the thermal transport and the particle distribution was demonstrated by comparing a nanoink droplet and a pure toluene droplet without particles. A clearly enhanced thermal transport in the nanoink droplet was found.

Chapter 3

Dissolution of Oxygen Bubbles in Blood

Parts of this chapter will be published in:
M. Fischer, I. Zinovik, and D. Poulikakos. Diffusion and reaction controlled dissolution of oxygen microbubbles in blood. *International Journal of Heat and Mass Transfer*. accepted for publication.

3.1 Introduction

In this chapter the dissolution of oxygen bubbles into blood is numerically investigated. Gas bubbles can form in the blood stream as a result of the specific physiological conditions or therapeutic and surgical interventions [47, 48]. Those are for example the decompression sickness of divers or the generation of microbubbles during non-invasive lithotripter procedures to eliminate kidney stones. Microbubbles originated in a cardiopulmonary bypass or in other extracorporeal tubing can be infused into the blood stream during invasive procedures. It is known that the presence of a large amount of gas in the blood circulation results in serious medical

complications. The uncertainty about the fate of the bubbles stipulates extensive experimental and modeling efforts to develop methods for the control and management of bubbles in blood circulation [48].

Numerous models to describe the dissolution of bubbles in a stream of fluid have been developed. In blood flow, these models assume spherical symmetry and adopt solutions of the Rayleigh-Plesset equation, extended to model the non-Newtonian behavior of blood [49]. In cases where the dissolution of the bubble is induced by the diffusion of gas from the surface of the bubble into blood, the simulations utilize the Epstein-Plesset model suggested in [50]. An extension of the Epstein-Plesset model for the simulation of multi-component gas bubbles in blood is suggested in [51]. If the blood pressure changes rapidly, the Epstein-Plesset solution is applied together with the Rayleigh-Plesset equation, which describes the pressure field around the bubble [52, 53].

The diffusion of the gas into blood is accompanied by the chemical reaction of oxygen with hemoglobin. The hemoglobin combines reversibly with molecular oxygen and forms oxyhemoglobin. In problems dealing with dissolving bubbles, the reaction of oxygen with hemoglobin is simulated as a simple binding process with constants defining the kinetic rates of forward and backward reactions [54, 55]. The life time of bubbles in blood is usually much smaller than the half-time of oxygen uptake. The size of bubbles circulating in blood flow lies within the range of $1\,\mu$m to $250\,\mu$m [52, 53, 56, 57] and the dissolution times of such bubbles may vary from 1 s to 600 s. The characteristic time of the shrinking process under consideration is significantly higher than the half-time of the reaction of oxygen uptake. From this follows that the binding of oxygen can be treated as an instant reaction thus avoiding the uncertainty that comes from the choice of the kinetic constants. The results shown in [58–60] indicate that this approach accurately predicts the concentration of oxygen in the blood-gas exchange devices.

The objective of the present work is to support the development of medical pro-

cedures and biomedical devices requiring the understanding of the physics and the control of the dynamics of microbubbles in blood circulation. The goal of the model herein is to analyze the dynamics of the diffusion-induced collapse of bubbles of oxygen in blood. The simulations employ a "facilitated" diffusion model. Unlike earlier simulations of bubbles in blood, the present model accounts for oxygen-hemoglobin interaction which has been shown to be important in experiments. The results of the simulations provide an insight into the oxygen transport in blood, caused by the dissolution of microbubbles.

3.2 Governing Equations

The physical system under consideration is presented in Figure 3.1. The bubble is assumed to be spherical and surrounded by blood at rest. Inertial and temperature effects within the bubble and in the blood are neglected due to the relatively small size of the simulated bubbles. The gas in the bubble is oxygen, which is modeled as an inviscid ideal gas. The pressure within the bubble is assumed to be spatially uniform. Earlier simulations [50, 61] of microbubbles dissolving in water and in blood indicate that the effect of surface tension decreases the collapse time by less than 3%. Therefore, the surface tension is not modeled in the present simulations, and it is assumed that the gas pressure within the bubble does not change over time. The last assumption implies that the dynamics of the surface of the bubble is controlled solely by the diffusion of gas through the interface into the blood. To this end, the model is limited to cases where dissolved gases other than oxygen do not significantly affect the dynamics of the bubble collapse.

The oxygen in the blood includes the physically dissolved oxygen and the hemoglobin bound oxygen inside red blood cells. The mass diffusion of the dissolved oxygen is governed by Fick's law with a constant diffusivity coefficient D. It is also assumed that the concentration of the dissolved oxygen at the gas-blood interface is governed

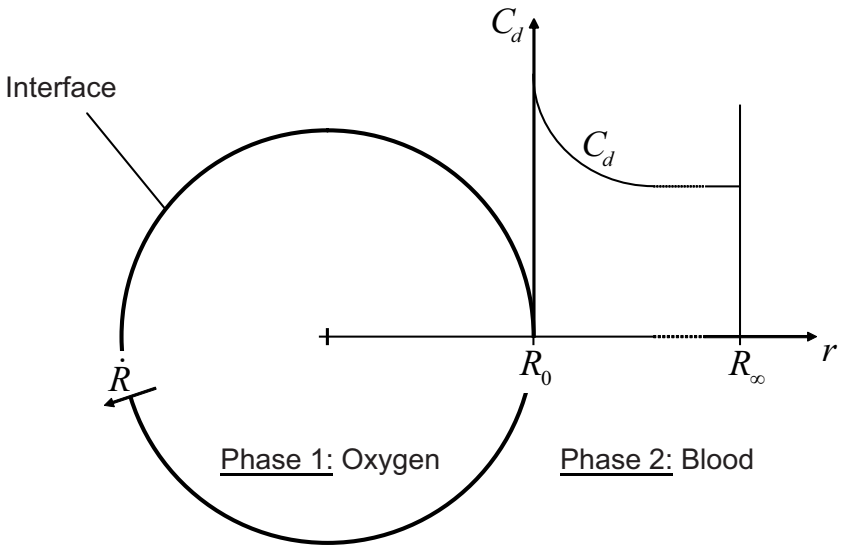

Figure 3.1: Schematic of the oxygen bubble surrounded by blood. Oxygen diffuses over the interface, the bubble starts to shrink.

by Henry's law with a constant solubility α. The hemoglobin bound oxygen is assumed to be in equilibrium with the dissolved oxygen. The degree of oxygen bound to hemoglobin in the blood is expressed using the Hill equation as the oxygen saturation S [54]:

$$S(P_{O_2}) = \frac{(P_{O_2}/P_{50})^n}{1 + (P_{O_2}/P_{50})^n}, \tag{3.1}$$

where P_{O2} is the partial pressure of the dissolved oxygen. Both P_{50} and n are constant parameters that depend on the physiological conditions of the blood and are usually derived from fitting experimental data. The total volumetric content of oxygen in blood V_{O2} is usually calculated as a sum of the concentrations of free physically dissolved oxygen and oxygen bound to hemoglobin as follows:

$$\mathrm{V_{O2}}=\alpha \mathrm{P_{O2}}+\mathrm{c_H S}, \tag{3.2}$$

where c_H=0.166 $(\mathrm{ml\,O_2})(\mathrm{ml\,blood})^{-1}$ and α=0.3 $(\mathrm{ml\,O_2})(\mathrm{ml\,blood})^{-1}(\mathrm{mmHg})^{-1}$ are the hemoglobin binding capacity and the physical solubility of oxygen respectively [60]. The density of oxygen dissolved in blood is much less than the density of blood

thus the total mass fraction C_t of oxygen in blood can be calculated as follows:

$$\mathrm{C_t}{=}\frac{\rho_{\mathrm{STP}}}{\rho_{\mathrm{b}}}\mathrm{V_{O2}}{=}\frac{\rho_{\mathrm{STP}}}{\rho_{\mathrm{b}}}\left(\alpha \mathrm{P_{O2}} + c_H S\right) = \mathrm{C_d}{+}\mathrm{C_b}, \tag{3.3}$$

where ρ_{STP} is the density of oxygen under standard conditions of atmospheric pressure and temperature of 273 K, ρ_b is the density of blood, and $\mathrm{C_d} = (\rho_{\mathrm{STP}}/\rho_{\mathrm{b}})\,\alpha \mathrm{P_{O2}}$, $\mathrm{C_b} = (\rho_{\mathrm{STP}}/\rho_{\mathrm{b}})\,cS$ denote the mass fractions of dissolved and bound oxygen respectively.

Under normal physiological conditions, the molecules of bound oxygen are attached to the hemoglobin of the red blood cells (RBC), which have a diameter of about 10 μm. The diffusivity coefficient of the cells in blood is much lower than the diffusivity of the molecular dissolved oxygen. Thus in a control volume of blood, the diffusive fluxes of bound oxygen can be neglected compared to the fluxes of dissolved oxygen. The diffusion equation for total mass fraction of oxygen in blood can be written as follows:

$$\frac{\partial C_t}{\partial t} = D\Delta C_d. \tag{3.4}$$

The substitution of 3.3 into 3.4 yields:

$$\frac{\partial C_d}{\partial t} + c_H \frac{\rho_{STP}}{\rho_b}\frac{\partial S}{\partial t} = D\Delta C_d. \tag{3.5}$$

If the saturation S defined by 3.1 is written as a function of the concentration of dissolved oxygen utilizing the Henry's law, equation 3.5 becomes:

$$\frac{\partial C_d}{\partial t} + c_H \frac{\rho_{STP}}{\rho_b}\frac{dS(C_d)}{dC_d}\frac{\partial C_d}{\partial t} = D\Delta C_d. \tag{3.6}$$

The mass balance of dissolved oxygen in a control volume of blood 3.6 can be rewritten as an equation with a facilitated diffusivity coefficient D_F:

$$\frac{\partial C_d}{\partial t} = D_F\Delta C_d, \tag{3.7}$$

where $D_F = D(1 + \lambda_S)$. The slope λ_S of the saturation curve is a function of the unknown mass fraction of the dissolved oxygen:

$$\lambda_S{=}\,\mathrm{c_H}\frac{\rho_{\mathrm{STP}}}{\rho_{\mathrm{b}}}\frac{\mathrm{n}}{C_{50}}\left(\frac{\mathrm{C_d}}{C_{50}}\right)^{\mathrm{n}-1}\Bigg/\left(1+\left(\frac{\mathrm{C_d}}{C_{50}}\right)^{\mathrm{n}}\right)^{2}. \tag{3.8}$$

The equation for the shrinkage rate of the dissolving bubble is derived from a mass balance of the gas bubble. The mass of oxygen inside the bubble changes due to the flux j of gas through the surface of the bubble:

$$\rho_{STP}\frac{d}{dt}\left(\frac{4}{3}\pi R^3\right) = -4\pi R^2 j, \tag{3.9}$$

where R is the radius of the bubble. This yields an expression of the velocity of the interface:

$$\frac{dR}{dt} = -\frac{j}{\rho_{STP}}. \tag{3.10}$$

The flux j at the bubble-blood interface is calculated as follows:

$$j = -\rho_b D\left(\frac{\partial C_d}{\partial r}\right)_R, \tag{3.11}$$

where the normal derivative is calculated at the bubble surface and the mass fraction C_d is obtained from the solution of the facilitated diffusion equation 3.7. A radius-time relation for the dissolving bubbles is found by solving equations 3.7, 3.9 and 3.11 together with appropriate boundary and initial conditions.

It is worth pointing out that the flux calculation is based on the physical diffusivity coefficient, while in the facilitated diffusion equation the coefficient D_F depends on the concentration of oxygen in blood. In the mass balance equation 3.7, the facilitated diffusivity coefficient combines the mass flux caused by the physical diffusion and the mass sink ($-\partial \mathrm{C_b}/\partial t$) due to the oxygen uptake reaction. Strictly speaking, equation 3.7 is not the diffusion transport equation with a concentration-dependent diffusivity coefficient. On this account a problem-specific numerical algorithm will be developed for the solution of this equation.

Simulations of microbubbles in blood reported in the literature usually employ the Epstein-Plesset model, which assumes a decoupling of the facilitated diffusion and the bubble radius-time relation. In the Epstein-Plesset model, the gradient of the concentration of dissolved gas on the shrinking surface of the bubble is computed based on the solution of the diffusion problem with a prescribed non-moving boundary. This gradient is then substituted into the equation for the radius-time relation.

Compared to Eppstein-Plesset, the present simulations utilize a numerical solution of the coupled system 3.7-3.11 where the shrinking of the bubble induces a moving boundary problem for equation 3.7. The obtained solution of the coupled problem allows an analysis of the assumption of the Epstein-Plesset model for microbubbles dissolving in blood.

3.3 Numerical Solution

The Finite Difference Method is applied to solve equations 3.7 and 3.10 simultaneously. For this purpose the algorithm, developed in Chapter 2, is adapted to the problem of a bubble dissolving in blood.

The facilitated diffusion equation is solved in the spherical coordinate system assuming spherical symmetry for the mass fraction distribution of the dissolved oxygen:

$$\frac{\partial C_d}{\partial t} = D_F \left[\frac{2}{r} \frac{\partial C_d}{\partial r} + \frac{\partial^2 C_d}{\partial r^2} \right], \tag{3.12}$$

where r is the radial coordinate. The following initial and boundary conditions are imposed at the outer boundary of the computational domain and at the bubble-liquid interface:

$$C_d(t=0) = C_0 \quad C_d(\infty, t) = C_0 \quad C_d(R, t) = C_R. \tag{3.13}$$

The mass balance equation for the gas in the bubble is written as follows:

$$\frac{dR}{dt} = \frac{\rho_b}{\rho_{STP}} \frac{D}{1+\lambda_S} \left(\frac{\partial C_d}{\partial r} \right)_R. \tag{3.14}$$

In order to develop an efficient numerical algorithm, the following non-dimensional concentration, time and radial coordinate are introduced:

$$\Phi = \frac{C_d}{C_0} \quad \tau = \frac{Dt}{R_0^2} \quad x = \frac{r - R_0}{R_0}. \tag{3.15}$$

The solution of the moving boundary problem requires a second transformation of the variables which is carried out using coordinates introduced by Landau [29]. The

Landau coordinates are:

$$\eta(x,\tau) = \frac{x - X(\tau)}{\delta(\tau)} = \frac{x - X(\tau)}{X_\infty - X(\tau)}, \tag{3.16}$$

where $X(\tau)$ is the moving non-dimensional position of the bubble-liquid interface and $X(\infty)$ is the fixed boundary of the computational domain. In the Landau variables, the facilitated diffusion equation is written as follows:

$$\frac{\partial \Phi}{\partial \tau} = A\frac{\partial \Phi}{\partial \eta} + B\frac{\partial^2 \Phi}{\partial \eta^2}, \tag{3.17}$$

where the coefficients A and B are defined as:

$$A = \frac{1}{\delta}\left(\frac{2}{(1+\lambda_S)(1+\eta\delta+X)} + (1-\eta)\frac{dX}{d\tau}\right) \tag{3.18}$$

$$B = \frac{1}{1+\lambda_S}\frac{1}{\delta^2}. \tag{3.19}$$

The mass balance of the gas in the bubble takes the form:

$$\frac{dX}{d\tau} = \frac{1}{(1+\lambda_S)}\frac{C_0}{\delta}\frac{\rho_b}{\rho_{STP}}\left(\frac{\partial \Phi}{\partial \eta}\right)_{\eta=0}. \tag{3.20}$$

A second order central differencing scheme in space and an implicit Euler scheme for the temporal discretization are utilized. The discretized facilitated diffusion equation is written as follows:

$$\frac{\Phi_i^{n+1} - \Phi_i^n}{\Delta\tau} = A\frac{\Phi_{i+1}^{n+1} - \Phi_{i-1}^{n+1}}{2\Delta\eta} + B\frac{\Phi_{i+1}^{n+1} - 2\Phi_i^{n+1} + \Phi_{i-1}^{n+1}}{(\Delta\eta)^2}. \tag{3.21}$$

The position of the interface is updated using a first order approximation:

$$X^{n+1} = X^n + \left(\frac{dX}{d\tau}\right)^{n+1} d\tau. \tag{3.22}$$

Accurate coupling of the interface velocity ($dX/d\tau$) and the gradient of the concentration at the interface is of crucial importance for the solution. Once the oxygen bubble at atmospheric pressure is introduced into blood, the concentration of oxygen at the blood-gas interface is one order of magnitude higher than the concentration of the dissolved oxygen. This high ratio causes a steep gradient of the concentration which in turn strongly affects the results of the computation of the radius-time

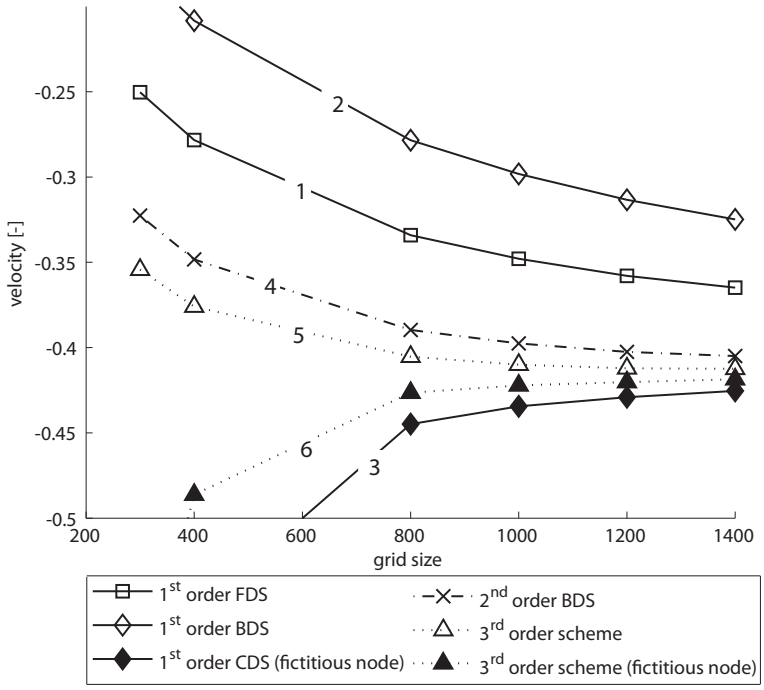

Figure 3.2: Velocity of the interface vs. grid size for different discretization schemes, with or without a fictitious node. The discretization schemes shown here are the forward- (FDS), backward- (BDS) and central-difference (CDS) scheme. Scheme 5 and 6 can be found in Reference [42].

relation and the collapse time. For this reason a higher order discretization scheme was used for the calculation of the concentration gradient. Figure 3.2 shows results of the velocity of the interface vs. the number of grid points applying different discretization methods. It can be seen that first order difference schemes (cases 1 to 3) fail to accurately predict the velocity of the interface for a reasonable number of grid points. Only higher order discretization schemes show sufficient accuracy. A third order discretization scheme (case 6) [42] for the calculation of the concentration gradient was added to the original algorithm [62]. This ensures an accurate approximation of the velocity of the interface:

$$\left(\frac{dX}{d\tau}\right) = \frac{1}{(1+\lambda_S)}\frac{\rho_b C_0}{\rho_{STP}}\frac{-\Phi_3 + 6\Phi_2 - 3\Phi_1 - 2\Phi_0}{6\delta\Delta\eta}. \tag{3.23}$$

In equation 3.23 Φ_0 is the dimensionless concentration in a fictitious node, which

is can be evaluated from equations 3.18, 3.19 and the discretized diffusion equation 3.21 as follows:

$$\Phi_0 = \frac{-\frac{1}{1+\lambda_S}\frac{4}{\delta\Delta\eta}\Phi_1 + \left(\frac{2}{(1+\lambda_S)(1+X)} + \frac{dX}{d\tau}\right)\Phi_2 + \frac{1}{1+\lambda_S}\frac{2}{\delta\Delta\eta}\Phi_2}{\left(\frac{2}{(1+\lambda_S)(1+X)} + \frac{dX}{d\tau}\right) - \frac{1}{1+\lambda_S}\frac{2}{\delta\Delta\eta}}. \tag{3.24}$$

Preliminary tests showed that if the value of interface velocity appearing in the coefficient A of equation 3.21 is computed using the value from the previous time step, the solution shows spurious oscillations towards the end of the shrinking process. In order to remedy this deficiency, the interface velocity is obtained solving a quadratic equation, which is derived by substituting equation 3.24 into 3.21 and 3.23 at the boundary of the domain:

$$\begin{aligned}\frac{\rho_{STP}}{\rho_b C_0} 6\delta\Delta\eta \left(\frac{dX}{d\tau}\right) &= \frac{(-3\Phi_1 + 4\Phi_2 - \Phi_3)\frac{dX}{d\tau}}{\frac{dX}{d\tau} + \frac{2}{(1+\lambda_S)(1+X)} - \frac{2}{(1+\lambda_S)\delta\Delta\eta}} \\ + \frac{(-6\Phi_1 + 8\Phi_2 - 2\Phi_3)\frac{1}{(1+\lambda_S)(1+X)}}{\frac{dX}{d\tau} + \frac{2}{(1+\lambda_S)(1+X)} - \frac{2}{(1+\lambda_S)\delta\Delta\eta}} &+ \frac{(14\Phi_1 - 16\Phi_2 + 2\Phi_3)\frac{1}{(1+\lambda_S)\delta\Delta\eta}}{\frac{dX}{d\tau} + \frac{2}{(1+\lambda_S)(1+X)} - \frac{2}{(1+\lambda_S)\delta\Delta\eta}}.\end{aligned} \tag{3.25}$$

After further simplification one obtains the quadratic equation:

$$\left(\frac{dX}{d\tau}\right)^2 + D\left(\frac{dX}{d\tau}\right) + E = 0, \tag{3.26}$$

with the coefficients D and E as:

$$\begin{aligned} D &= \frac{2}{1+\lambda_S}\left(\frac{1}{1+X} - \frac{1}{\delta\Delta\eta}\right) + \frac{\rho_b C_0}{\rho_{STP}}\frac{3\Phi_1 - 4\Phi_2 + \Phi_3}{6\delta\Delta\eta} \\ E &= \frac{\rho_b C_0}{\rho_{STP}}\frac{1}{3\,(1+\lambda_S)\,\delta\Delta\eta}\left(\frac{3\Phi_1 - 4\Phi_2 + \Phi_3}{1+X} + \frac{-7\Phi_1 + 8\Phi_2 - \Phi_3}{\delta\Delta\eta}\right) \end{aligned} . \tag{3.27}$$

The solution of equation 3.26 results in an expression for the velocity of the interface:

$$\left(\frac{dX}{d\tau}\right) = -\frac{1}{2}D - \sqrt{\frac{1}{4}D^2 - E}. \tag{3.28}$$

Using equation 3.27 to compute the velocity in the coefficient A of equation 3.21 results in a stable solution of the velocity throughout the whole shrinking process.

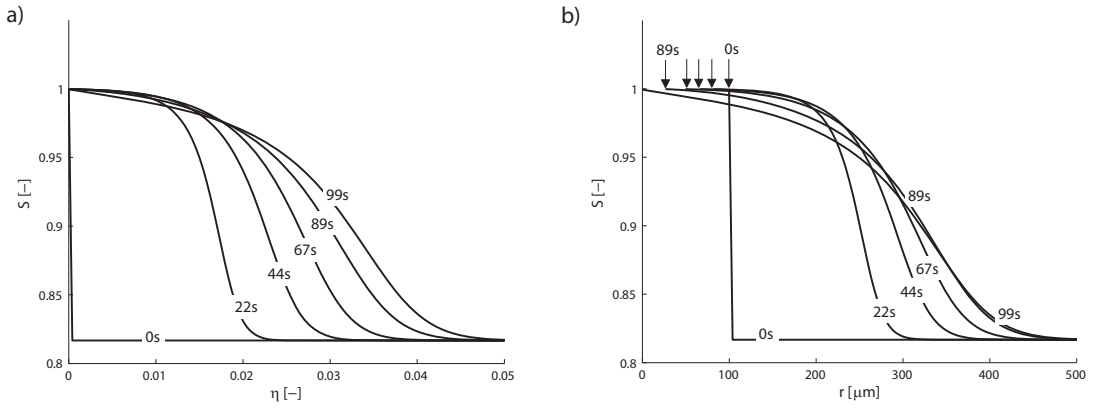

Figure 3.3: Radial profiles of blood saturation around an oxygen bubble with initial radius of 100 μm, D= 1.8×10^{-5} cm^2 s^{-1}, n=2.7, P_0=51 mmHg, P_R=760 mmHg. On the left side the profiles are shown in fixed Landau coordinates (a) whereas the right Figure (b) depicts the profile in physical coordinates.

3.4 Results and Discussion

The profiles of blood saturation around a bubble with initial radius R=100 μm is shown in Figure 3.3. The following set of model parameters is chosen for the base case simulation: the pressure of oxygen inside the bubble is specified to be 760 mmHg and the initial concentration of oxygen in blood equals 51 mmHg; the parameters of the Hill's equation are set to be n=2.7 and P_{50}=28 mmHg. The diffusivity is assumed to be 1.8×10^{-5} cm^2 s^{-1} [54]. In this case neglecting the effect of surface tension is a reasonable approximation because the increase of pressure inside the bubble due to surface tension is comparable with the initial pressure when the radius is about 1 μm, i.e. the size of the bubble decreases by two orders of magnitude.

In Figure 3.3a, the profiles are shown in the Landau coordinates in a fixed computational domain. The last curve corresponds to the saturation profile at the moment of the bubble collapse. The results indicate that the saturation front rapidly propagates into blood in the first 22 s, and then the velocity of the front drops by 3-4 times and slows down until the full dissolution of the bubble. The fast initial velocity of

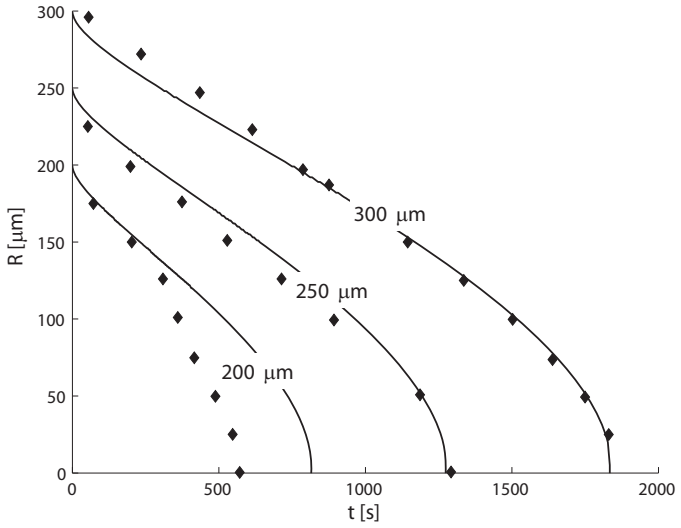

Figure 3.4: Temporal evolution of the radius of dissolving bubbles in degassed blood. Experimental data are obtained from [64]. Numerical values: D=$0.7 \times 10^{-5}\,\mathrm{cm^2\,s^{-1}}$, n=2.7, P_0=51 mmHg, pressure in bubble: P_R=760 mmHg. The value of the initial radius is shown next to the corresponding curve. The Diamonds denote the experimental results from [63].

the oxygenation front is qualitatively similar to rapid oxygenation of a thin layer of blood adjacent to the bubble observed in the experiments [63]. The same set of profiles as in Fig. 3.3a is illustrated in Figure 3.3b in physical coordinates where the left endpoint of the profile coincides with the instant position of the interface. As oxygen diffuses into blood, the surface is shrinking towards its center. The shrinking is slightly accelerated over time. At the moment of collapse, oxygen from the bubble diffuses into a blood volume which is bounded by a sphere with a radius about three times greater than the initial radius of the bubble.

The results of earlier experiments [63] are used to validate the model of bubble dissolution presented in this work. In the experiments, radius-time relations of oxygen bubbles dissolving in degassed blood are recorded for bubbles with radii from 200 μm to 300 μm. In Figure 3.4, the experimental data is compared with the

results of the simulations. The parameters of blood under the conditions of the tests in [63] are not reported. In the simulations, the value of diffusivity D has been chosen to serve as a fitting parameter, while the Hill's constants are assumed to be the same as for Figure 3.3. The best fit has been found with D=$0.7 \times 10^{-5}\,\mathrm{cm}^2\,\mathrm{s}^{-1}$. This value is in the lower part of the physiological range as reported in [64]. The results of the simulations deviate less than 10% from the data for the bubbles with radii 250 μm and 300 μm. For the smaller bubbles, the calculations overestimate the collapse time by about 20%. Two additional factors in addition to the uncertainty regarding the blood parameters could cause this deviation: 1) the bubbles in the tests are reported to be non-spherical and are attached to a wall; 2) the reported value of the initial radius is not measured directly at the beginning of the experiment but is extrapolated from the measurements at later times. The overall agreement of the data and the simulations shows that the proposed model is capable of predicting the radius-time relations for the dissolving microbubbles.

The collapse time as a function of the initial content of oxygen in blood is shown in Figure 3.5. In the simulations, the initial content of oxygen in blood is varied within the physiological conditions with an oxygen partial pressure from 25 mmHg to 77 mmHg. For comparison purposes, the calculated time is plotted together with a test computation where the uptake of oxygen is excluded from the model and with the results which are obtained using the Epstein-Plesset model.

In the Epstein-Plesset model, the flux of oxygen from the bubble at a given instance is computed neglecting the movement of the bubble interface at the same instance. In the present simulations, the interface movement and the diffusion problem are coupled. Thus, the shrinking of the bubble surface towards its center leads to a decrease of the gradient of dissolved gas at the liquid side of the interface. As a consequence the related slow down of the collapse process is predicted by the present model. The results shown in Figure 3.5 indicate that the quasi-steady approach of the Epstein-Plesset model leads to a shorter collapse time compared to the model

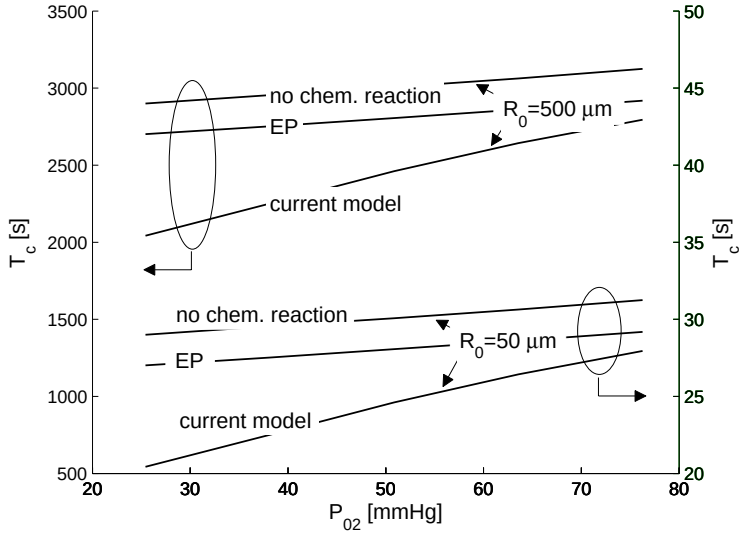

Figure 3.5: Collapse time T_c as a function of the initial content of oxygen for two different radii, R_0=500 μm (top) and R_0=50 μm (bottom); EP denotes the results of the Epstein-Plesset model.

coupling the calculations of diffusion and radius change. In the test cases with an initial bubble radius 50 μm and 500 μm, the same 8% difference in the simulated collapse times is observed regardless of the initial concentration of oxygen in blood.

Including the oxygen uptake reaction into the simulations causes a reduction of the collapse time due to the sink term which is incorporated into the facilitated diffusion coefficient. The time decreases by 31% for low initial concentrations of oxygen and by 11% for high concentrations. The impact of the reaction of oxygen binding is higher at a low oxygen concentration due to the lower fraction of oxygen bound to hemoglobin. Thus a higher capacity for the oxygen uptake in the initial phase of the collapse exists. The curves for different bubbles shown in Figure 3.5 are parallel, because the calculated collapse time is proportional to the second power of the initial radius R_0.

Different physiological factors including diseases may affect the ability of blood to diffuse and to bound oxygen. For example, the diffusivity coefficient D decreases

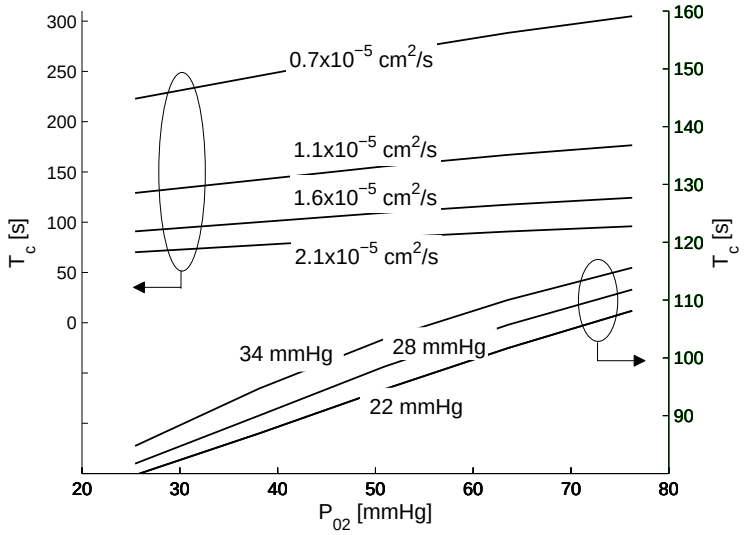

Figure 3.6: Collapse time as a function of the initial content of oxygen for different physical conditions. The diffusion coefficient (shown next to curve) is varied between $0.7 \times 10^{-5}\,\mathrm{cm^2\,s^{-1}}$ and $2.1 \times 10^{-5}\,\mathrm{cm^2\,s^{-1}}$ (top). The Hill's parameter P_{50} (shown next to curve) is varied between 34 mmHg and 28 mmHg (bottom).

with the increase of concentration of hemoglobin in RBC [65], and is highly sensitive to the concentration of albumin in plasma [54]. The physiological variables can also trigger a shift in the saturation curve. An increase of the concentration of dissolved carbon dioxide or temperature requires a higher concentration of oxygen for a given saturation level. On the contrary, a rise in pH-concentration promotes the steepness of the saturation curve [54]. The shift of the saturation curve leads to a change of the fitting coefficients in Hill's equation.

The impact of various physiological conditions on the collapse time is illustrated in Figure 3.6. The plots show the results of a parametric study where the values of the diffusivity D and the Hill's equation parameter P_{50} were changed within the physiological ranges reported in [54, 65]. A shift of the saturation curve causes the collapse time to change by approximately 20%, while the decrease of the diffusivity coefficient results in an almost four times slower dissolution. The collapse time shown

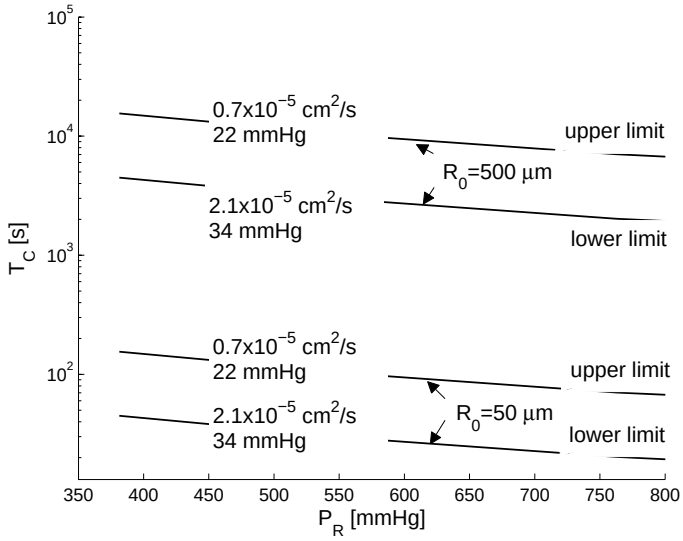

Figure 3.7: Collapse time as a function of oxygen pressure inside the bubble P_R for different physiological conditions: diffusivity coefficient and the Hill's parameter P_{50} are shown next to the corresponding curve.

in the upper part of Figure 3.6 is calculated with a constant incremental change of the diffusivity coefficient. The uneven shift of the corresponding curves points out that the collapse time is inversely proportional to the diffusivity coefficient as it follows from the dimensional analysis of the problem.

The collapse time shown in Figures. 1 to 4 is calculated assuming that the oxygen pressure in the bubble is atmospheric. If the bubble is introduced into the blood stream in cardiopulmonary bypass or as a result of cavitiation in an artificial heart, the pressure of oxygen inside the bubble may differ from the atmospheric pressure. In the presented model, the pressure inside the bubble is a free parameter which was varied to estimate the influence of the gas pressure on the collapse time. In Figure 3.7, the curves delineate regions of the collapse time for the bubbles with an initial radius of 50 μm and 500 μm. The data is computed for the values of diffusivity D and the Hill's parameter P_{50} which provide the upper and the lower bounds of the collapse time [54]. The simulations show that smaller bubbles with high oxygen

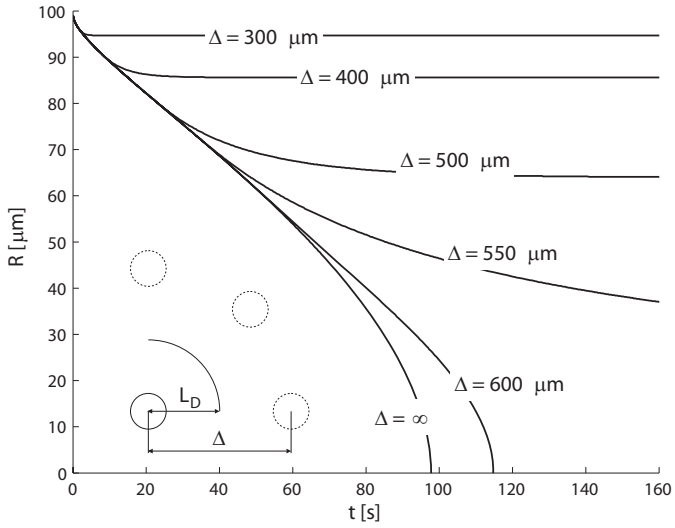

Figure 3.8: Radius-time relations for a bubble surrounded by multiple bubbles. The surrounding bubbles are located at distance Δ from the center of the dissolving bubble. The initial radius of the bubbles was set to 100 μm and D=1.8 $\times$ 10^{-5} cm^2 s^{-1}.

pressure should collapse in about 10 seconds. Larger bubbles with low gas pressure may last in blood for several hours.

In the simulations, the bubble is assumed to be surrounded by a relatively large volume of blood such that the bubble collapses before the dissolved oxygen reaches the outer boundary of the simulated blood volume. The profile of the dissolved oxygen at the collapse moment shown in Figure 3.3 indicates that oxygen from a bubble diffuses up to three initial radii from the center of the bubble. If a second bubble with the same initial radius is located at a distance less than six radii from the first bubble, the concentration profile of oxygen should be affected by the interference of the dissolved gas diffused from the different bubbles. The interference should increase the collapse time due to a higher amount of gas that has to be absorbed by the same blood volume.

While the analysis of clusters of bubbles is beyond the scope of the present study, the boundary conditions of the model with a single bubble can be modified to

obtain an estimate of the impact of multiple bubbles on the collapse time. If two identical bubbles dissolve simultaneously, the symmetry of the problem implies that the gradient of the concentration of dissolved gas in the midpoint between the two bubble centers equals zero. Consequently the diffusion problem for two bubbles can be solved in the semi-space with Neumann boundary conditions imposed at the plane of symmetry. A series of simulations has been conducted, enforcing zero-gradient conditions at the domain boundary. The calculated collapse time is shown in Figure 3.8 for different lengths L_D of the computational domain. The simulations may be interpreted as an approximation of the diffusion problem for a bubble which is surrounded by multiple bubbles of the same size which are equally spaced at the distance $\Delta = 2L_D$ from the center of the bubble.

The radius-time relations shown in Figure 3.8 illustrate the increase of the collapse time due to the shielding effect of the bubbles in the cluster. If the distance between the central bubble and the surrounding bubbles decreases below 6 initial radii, the bubble shrinks only by a fraction and then stabilizes.

The presence of other bubbles is one of several factors which may affect the accuracy of the prediction of collapse time. To this end, in blood circulation in the human body bubbles take a more elongated shape [48]. The change of the shape may cause more than a 50% increase of the dissolution time as compared with the spherical bubble [47]. When the gas composition is not oxygen, the bubble collapse time may increase as well due to low diffusivity of the mixture components. A layer of denaturated proteins formed at the bubble blood interface results in additional slowdown of the dissolution [47].

At the late stage of the dissolution, the assumption of a constant gas pressure in the bubble has to be revised to take the effect of surface tension into account. Moreover when the bubble radius decreases to approximately $10\,\mu$m, the bubble becomes comparable with the size of RBC. In these conditions, the assumption that blood around the bubble can be modeled as a uniform fluid is not acceptable any more.

It could be concluded that the presented model is expected to underestimate the actual life span of the microbubbles in blood. Nevertheless, the computed collapse time may serve as a viable estimate of the lower bound of the dissolution time of single bubbles.

3.5 Conclusions

In this chapter the diffusion controlled dissolution of oxygen microbubbles into surrounding blood was numerically investigated. A spherical symmetric model based on the finite difference method was introduced and extended to account for the oxygen uptake by the hemoglobin.

The derived method has been validated using radius-time relations reported from experiments and was compared to the approximate solution of the Epstein-Plesset model. It was shown that the quasi-steady assumption of the Epstein-Plesset model leads to an approximate 8% shorter collapse time as compared to the present fully coupled numerical algorithm. In cases when the oxygen uptake reaction is included the calculated collapse time is about 30% lower than the predictions of the Epstein-Plesset model that neglects chemical reactions.

A parametric study on different physiological conditions has been conducted revealing that the collapse time strongly depends on the size of the bubbles and on the parameters which specify the blood conditions. Small bubbles with an initial diameter of 50 μm collapse in about ten seconds, whereas larger bubbles with an diameter of 500 μm may last in blood for several hours.

The limitations of the model have been discussed. It was concluded that the calculated collapse time gives a valuable estimate of the lower bound of the dissolution time of a spherical bubble in blood if the collapse is controlled by the facilitated diffusion of oxygen. Such estimates are useful and alleviate the need for tedious experiments in certain situations.

Chapter 4

Heat Transfer in Microchannel Flow

Parts of this chapter have been submitted for publication in:
M. Fischer, D. Juric, and D. Poulikakos. Large convective heat transfer enhancement in microchannels with a train of co-flowing immiscible or colloidal droplets. *International Journal of Heat and Mass Transfer*

4.1 Introduction

Thermal management of micro electronic devices becomes more important and challenging as size is reduced and power density (converted to heat) increases. The demand of fast removal of the produced heat in microscale devices such as microprocessors or even micro fuel cells stimulates growing research activities in the field of liquid cooling [12–15]. Among various techniques to improve the cooling performance in micro channels, we mention two promising approaches.

One is, using engineered fluids, such as colloids consisting of a base fluid in which solid particles of grain sizes of 10 to 50 nm are dissolved. In this case the thermal transport properties can be significantly improved compared to the base fluid at

concentrations of a few percent per volume, however, at the expense of a corresponding increase in viscosity. Depending on particle size and concentration, the effective thermal conductivity of those fluids can be increased by as much as 10 to 40% [20, 21]. For example, Lee et al. [21] report in their study a 10% heat transfer enhancement using a suspension of Al_2O_3 particles of 38 nm in diameter at a concentration of 4.5% in distilled water. For detailed reviews on the thermal transport connected to nanofluids see Keblinski [66] and Wang [67].

Another option to improve cooling exploits the fact, that the heat removal rate from the channel wall in multiphase flows is higher than in single phase flows. In the presence of immersed bubbles, the thermal transport is augmented by a blockage effect in front of the bubbles and recirculation in their wake. Lakehal et al. [16] and Fukagata et al. [17] showed numerically that in the case of gas liquid flow, the heat transfer is three to four times higher than in pure water flow. Recently, a numerical study by Urbant et al. [18] on liquid-liquid flow indicated a similar trend. The number of experimental studies on heat transfer augmentation in two-liquid flows but also on two phase gas-liquid flows in microchannels is limited. Only Monde and Mitsutake [19] reported experiments on enhanced heat transfer in bubbly flow through small scale channels.

The present work aims at taking advantage of both of the above mentioned approaches, by introducing immiscible colloidal droplets into the liquid flow in a microchannel. In addition to a significant increase in the cooling performance, this approach is expected to result in a decrease in the undesirable pressure drop associated with the colloidal suspensions (nanoliquids). The effect of non-colloidal droplets is also investigated.

Spherical or elongated nanofluid droplets are introduced at the entrance region of the channel into the base fluid. The flow around the droplets develops as they travel further downstream. There exist different methods to experimentally establish liquid-liquid droplet laden flows. Those are for example flow or hydrodynamic

focusing techniques [68,69], T- and Y-Junctions [70–72] or concentric injection [73]. Cubaud and Mason [69] used a flow focusing device, to produce liquid emulsions in a 100 μm wide micro channel. They report on different flow patterns, based on the capillary number of each fluid. The flow parameters and channel sizes in the presented study are in the range of the above mentioned experiments.

In this chapter all important aspects related to immiscible and colloidal droplet-laden two-fluid flow through heated microchannels are numerically investigated. Parametric studies assess the influence of different flow conditions (e.g. velocity and radius), liquid systems of water in oil and oil in water emulsions and the presence of nanoparticles on the cooling performance of the channel. This is reported by the calculated local and overall Nusselt number. The model presented includes all relevant thermophysical phenomena such as Marangoni effects caused by variable surface tension due to temperature gradients at the liquid-liquid interface as well as nanoparticle motion within the droplet.

A two component mixture model is applied to account for the convective and diffusive nanoparticle transport within the nanofluid droplet [25,62]. This model includes thermophoresis due to temperature gradients and Brownian diffusion which are the major slip mechanisms causing nanoparticle transport relative to the embedding liquid.

In order to keep track of the interface between the droplets and the base fluid, a Front Tracking method is employed [74]. There exist several methods for dealing with two phase flows, such as volume of fluid [75], level set [76], phase field [77] or front tracking methods [78]. Lakehal et al [16] and Fukagata et al [17], for example, employed a level set approach to calculate thermal two-phase flow in micro channels. Urbant et al [18] used the volume of fluid method, although by applying interfacial tension values of only 5 mN m^{-1}.

Rather high interfacial tension values (40 mN m^{-1}) resulting in Capillary numbers of O(-4) as well as high viscosity ratios in the present simulation dictate the need for an

accurate and reliable algorithm for calculating the interfacial forces. The accurate calculation of surface tension force becomes a major issue especially in flows, where capillary forces are the dominant physical mechanism [79]. In conventional volume of fluid methods, applying the continuous surface force model (CSF) [80], this can lead to non-physical, spurious currents [79]. In Front tracking, spurious currents remain a rather small issue. However, to further suppress those numerical artifacts and to be able to calculate at even smaller Capillary numbers, a hybrid surface tension calculation method is applied [74]. In this method, the solution of the interface curvature is based on the classical Lagrangian front tracking approach and the surface tension force is calculated based on the Eulerian approach used in level set and volume of fluid methods.

In the following section, the physical model and the governing transport equations for multiphase flow as well as an additional equation describing the convective and diffusive transport of nanoparticles in the colloid are introduced. The solution procedure and dimensionless groups relevant for thermal transport in micro channels are presented in Section 4.3. Results of the calculations as well as parametric studies on the heat transfer can be found in Section 4.4, followed by concluding remarks in Section 4.5.

4.2 Problem Definition

The microchannel under investigation is presented in Figure 4.1. Liquid droplets of different size and elongation are immersed into the base fluid at the entrance region. In the first part of the channel, the flow around the droplets develops as they are moving with the base fluid further downstream. Once the flow field is fully developed, the droplets enter the "thermal section" in the second part of the channel. Here, the channel wall is heated and the heat transfer to the two fluid flow is investigated. For a single fluid, the flow through the cylindrical channel would

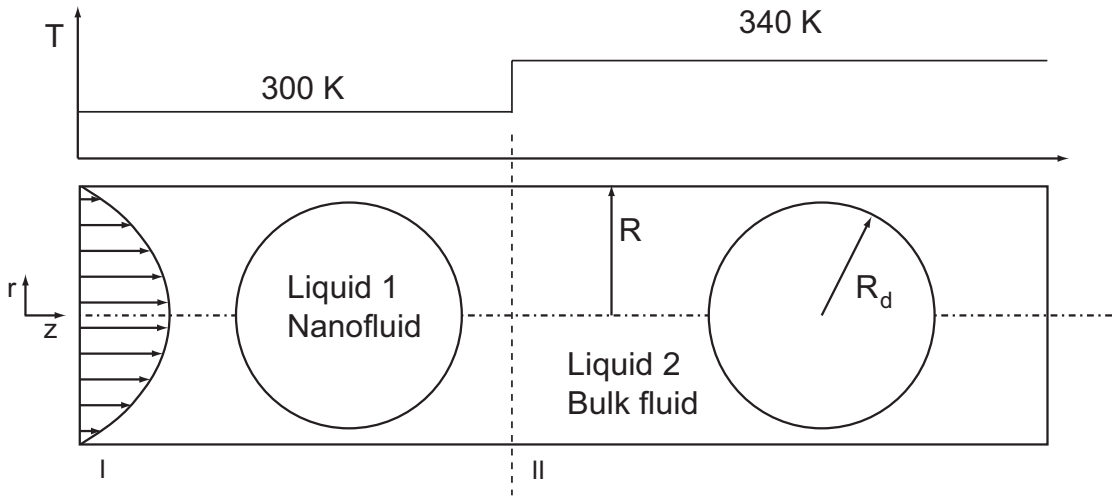

Figure 4.1: The physical system under consideration. In the isothermal section of the microchannel, the droplets (liquid 1) are immersed into the base fluid (liquid 2).

follow the well known Graetz Problem of a thermally developing and hydrodynamically fully developed laminar flow [81]. To conserve computational time, we set the boundary conditions at the inlet to a fully developed Hagen-Poiseuille flow profile. The temperature distribution along the channel wall follows a step function. In the first, isothermal section, the wall temperature is equal to the temperature of the liquid and after six channel radii it is increased to 340 K and is kept at this value afterwards. The length of the channel is 26 radii to assure fully developed conditions and to capture all phenomena present in the thermal entrance region.

The fluid inside the droplet is either pure silicon oil, water or a nanofluid consisting of nanoparticles and a solvent, in our case either polyalphaolefine (PAO) or water. The droplets are surrounded by the bulk fluid, which is, depending on the liquid within the droplet, either pure water or silicon oil. In the following, the fluid inside the droplets will be denoted as liquid 1, the bulk fluid as liquid 2. The channel diameter is varied between 100 μm and 1 mm. The mean velocity in the channel ranges from 1 to 10 cm/s. These values are in the same range as reported in experiments of liquid-liquid flow [68–73]. The resulting Reynolds number ($\mathrm{Re}_i = v_0 \rho_i R_0 / \mu_i$)

between 1.0×10^{-2} and 100 indicate the purely laminar regime of the fluid flow. The strong influence of surface tension on the flow can be seen by the Weber number ($We_i = \rho_i R_0 v_0^2/\sigma_0$) being as low as 1.1×10^{-4} to 1.9×10^{-1}. The Peclet number ($Pe_i = Re_i\, Pr_i$) varies between 3.5 and 700.

The problem is solved using one set of continuity equations for the entire domain both inside and outside the droplets and is modeled as 2D axisymmetric. Both liquids are treated as incompressible with no external body forces, as the influence of gravity can be regarded as negligible. This is justified by Bond numbers well below unity ($\Delta\rho g R_0^2/\sigma \ll 1$). With the above mentioned assumptions, the continuity and Navier-Stokes equations for the entire physical domain read:

$$\nabla \cdot \mathbf{v} = 0, \tag{4.1}$$

$$\rho\left[\frac{\partial \mathbf{v}}{\partial t} + \mathbf{v}\cdot\nabla\mathbf{v}\right] = -\nabla p + \nabla\cdot\mu\left[\nabla\mathbf{v} + \nabla\mathbf{v}^T\right] + \mathbf{F}, \tag{4.2}$$

where ρ and μ are the density and viscosity of the liquids. The last term in equation 4.2 accounts for the interfacial tension force, which can be calculated as:

$$\mathbf{F} = \int_{S'(t)} (\sigma\kappa\mathbf{n} + \nabla s\sigma)\delta(\mathbf{x} - \mathbf{x}')dS. \tag{4.3}$$

In equation 4.3 σ and κ denote the temperature-dependent interfacial tension and the curvature of the interface.$\mathbf{n}$ is the normal to the interface, ∇s is the tangential gradient operator and the Dirac distribution, $\delta(\mathbf{x} - \mathbf{x}')$ localizes the effects of the surface tension to the interface, $S'(t)$ defined by $\mathbf{x}'$. Contrary to the CSF method, the calculated curvature κ is related to the actual physical curvature of the Lagrangian interface [74]. The interfacial tension is calculated assuming a linear dependency on temperature:

$$\sigma(T) = \sigma_0 + \sigma_T T, \tag{4.4}$$

where σ_0 denotes the interfacial tension at a given temperature T_0 and $\sigma_T = -d\sigma/dT$ the temperature coefficient.

The nanoparticle continuity and energy equations are derived from Buongiorno [25]. Here, the mixture of nanoparticles and its solvent is treated as a single phase and

the nanofluid is considered to be a dilute mixture. Brownian diffusion and thermophoresis, which is the particle motion under the influence of a thermal gradient, are the only relevant slip mechanisms for nanoparticle transport in laminar flow. They are incorporated into the nanoparticle transport equation as follows:

$$\frac{\partial \psi}{\partial t} + \mathbf{v} \cdot \nabla \psi = \nabla \cdot \left[D_B \nabla \psi + D_T \frac{\nabla T}{T} \right], \tag{4.5}$$

where ψ denotes the particle volume fraction. Brownian diffusion and thermophoresis are described by the first and second term on the right hand side, respectively. D_B and D_T are the Brownian and the temperature dependent thermal diffusion coefficient, respectively. In the nanofluid, the coefficients can be calculated as:

$$D_B = \frac{k_B T}{3\pi \mu d_p} \qquad D_T = \beta \frac{\mu}{\rho} \psi, \tag{4.6}$$

where k_B denotes Boltzmann's constant and β is a proportionality factor. In the bulk fluid (liquid 2) both diffusion coefficients are set to zero.

In the presence of nanoparticles the energy equation takes the form:

$$\rho\, c \left[\frac{\partial T}{\partial t} + \mathbf{v} \cdot \nabla T \right] = \nabla \cdot \lambda \nabla T + \rho_p c_p \left[D_B \nabla \psi \cdot \nabla T + D_T \frac{\nabla T \cdot \nabla T}{T} \right]. \tag{4.7}$$

Here, ρ_p and c_p are the nanoparticle density and specific heat. The entire term in brackets on the right hand side accounts for thermal transport due to particle motion. An order of magnitude analysis reveals that this term is negligible and the energy equation becomes identical to the one of a pure fluid [25]. From this follows that the nanoparticles affect the heat transfer in the nanofluid only by their influence on the thermophysical properties.

The spatial distribution of the property fields in the entire physical domain can be calculated using the indicator function I. The calculation of I is presented in reference [74]. This function is 1 inside the droplet and zero in the bulk fluid. For example, for the density field it follows:

$$\rho\,(\mathbf{x}, t) = \rho_2 + (\rho_1 - \rho_2)\, I\,(\mathbf{x}, t)\,, \tag{4.8}$$

where ρ_1 and ρ_2 are the densities of the nanofluid and the bulk fluid, respectively. The dynamic viscosity, thermal conductivity and specific heat can be determined using the same approach. The spatial distribution of the diffusion coefficients is calculated using the same approach. By setting the diffusion coefficients in liquid 2 identical to zero and following equation 4.8 one obtains:

$$\begin{aligned} D_B(\mathbf{x},t) &= D_{B,1} I(\mathbf{x},t), \\ D_T(\mathbf{x},t) &= D_{T,1} I(\mathbf{x},t). \end{aligned} \tag{4.9}$$

The property field varies not only between the two liquids but also within the nanofluid (liquid 1), as it is a function of particle concentration. The density and specific heat of the nanofluid can be calculated using standard mixture laws:

$$\begin{aligned} \rho_1 &= \psi\rho_p + (1-\psi)\rho_s, \\ c_1 &= \frac{\psi c_p \rho_p + (1-\psi) c_s \rho_s}{\rho_1}. \end{aligned} \tag{4.10}$$

ρ_s and ρ_p denote the density of the solvent and the particles, respectively. There is still a lack of accurate theoretical models for the prediction of the viscosity and thermal conductivity of nanofluids. From measurements by Pak and Cho [82] the following correlations for the viscosity and thermal conductivity of alumina nanoparticles, dissolved in water can be derived [25]:

$$\mu_1 = \mu_s\left(1 + 39.11\psi + 533.9\psi^2\right), \tag{4.11}$$

$$\lambda_1 = \lambda_s\left(1 + 7.47\psi\right). \tag{4.12}$$

For Alumina particles in PAO the viscosity and thermal conductivity can be correlated as follows:

$$\mu_1 = \mu_s\left(1 + 18.8\psi\right), \tag{4.13}$$

$$\lambda_1 = \lambda_s\left(1 + 4.97\psi\right). \tag{4.14}$$

4.3 Numerical Solution

In order to facilitate the numerical simulation and to investigate the influence of the different characteristic groups, the following dimensionless scales are introduced:

$$\begin{aligned} \mathbf{u} = \frac{\mathbf{v}}{v_0} \quad \phi = \frac{\psi}{\psi_0} \quad \theta = \frac{T - T_0}{\Delta T} \\ \wp = \frac{P}{\rho_2 v_0^2} \quad x = \frac{r}{R} \quad \tau = t\frac{v_0}{R}. \end{aligned} \tag{4.15}$$

where v_0, ψ_0 ,R ,T_0 and ΔT are the mean velocity at the inlet of the channel, the initial nanoparticle concentration in the nanofluid, the channel radius, the initial temperature and a temperature scale, respectively. With those transformations the governing equations 4.1,4.2,4.5 and 4.7 read:

$$\nabla \cdot \mathbf{u} = 0 \tag{4.16}$$

$$\frac{\partial \mathbf{u}}{\partial \tau} + \mathbf{u} \cdot \nabla \mathbf{u} = -\frac{1}{\rho^*}\nabla p + \frac{1}{\rho^* \mathrm{Re}_2}\nabla \cdot \mu^* \left[\nabla \mathbf{u} + \nabla \mathbf{u}^T\right] + \frac{\mathbf{F}}{\rho^* We_2} \tag{4.17}$$

$$\frac{\partial \phi}{\partial \tau} + \mathbf{u} \cdot \nabla \phi = \frac{1}{\mathrm{Re}_2 Sc_2}\left[\nabla \cdot I \nabla \phi + \nabla \cdot \frac{I}{N_T}\nabla \theta\right] \tag{4.18}$$

$$\frac{\partial \theta}{\partial \tau} + \mathbf{u} \cdot \nabla \theta = \frac{1}{\mathrm{Re}_2 \mathrm{Pr}_2}\frac{1}{\rho^* c^*}\nabla \cdot \lambda^* \nabla \theta. \tag{4.19}$$

The physical properties in equations 4.16 to 4.18 are brought in dimensionless form with the values of the continuous phase (liquid 2). The following dimensionless groups were introduced: the Reynolds, Schmidt, Prandtl and Weber number as well as N_{BT} , which is the characteristic number for thermophoretic particle motion:

$$\begin{aligned} \mathrm{Re}_i = \frac{v_0 \rho_i R_0}{\mu_i} \qquad Sc_i = \frac{\mu_i}{\rho_i D_B} \qquad \underset{i}{\mathrm{Pr}} = \frac{c_i \mu_i}{\lambda_i} \\ N_{BT} = \frac{\rho_i D_B T_0}{\beta \mu_i \Delta T} \qquad We_i = \frac{\rho_i R_0 v_0^2}{\sigma_0}. \end{aligned} \tag{4.20}$$

Two additional dimensionless numbers are used later on. Those are the Capillary number and the Peclet number:

$$Ca_i = \frac{v_0 \mu_i}{\sigma_0} \qquad \mathrm{Pe}_i = \frac{\rho_i v_0 c_i R_0}{\lambda_i}. \tag{4.21}$$

Following [74], equations 4.16-4.19 are solved on a regular staggered MAC grid [83], where the pressure, temperature and particle concentration are located at the cell centers. The u- and v- velocity are located at the face centers. The diffusive terms are approximated using second order central differences. For the convective terms a second order ENO scheme is applied [84]. A second order implicit scheme is used for the temporal discretization. For the solution of the transport equations the bi-conjugate gradient stabilized algorithm (BiCGStab) is applied. The convergence criterion on the maximal residuals was set to 1.0×10^{-7}. The update of the Navier-Stokes equation is done by using Chorin's projection method [85]. In this method, the momentum equation is split into two parts. First a prediction velocity $\tilde{\mathbf{u}}$ is calculated. For example, in a first order time integration the prediction velocity is updated in time step $n+1$ as:

$$\tilde{\mathbf{u}} = \mathbf{u}^n + \frac{\Delta\tau}{\rho^{*,n+1}} \left(\frac{1}{\rho^* \mathrm{Re}_2} \nabla\mu^* \left[\nabla\mathbf{u} + \mathbf{u}^T \right] + \frac{\mathbf{F}}{\rho^* We_2} \right)^n, \tag{4.22}$$

where $\Delta\tau$ is the time step size. In a second step the velocity field is corrected with the solution of the Poisson equation,

$$\nabla \left(\frac{1}{\rho^{*,n+1}} \nabla p \right) = \frac{\nabla\tilde{\mathbf{u}}}{\Delta\tau}, \tag{4.23}$$

as follows:

$$\mathbf{u}^{n+1} = \tilde{\mathbf{u}} - \frac{\Delta\tau}{\rho^{*,n+1}} \nabla p. \tag{4.24}$$

In the Front Tracking method the transport equations for the fluid flow are solved on a regular stationary Eulerian grid, but the interface between the two phases is explicitly tracked with a moving interface mesh in a Lagrangian manner. At each time step, information such as the velocity and curvature of the interface must be interpolated to the stationary Eulerian mesh on which the transport equations are solved. In addition, variables from the stationary mesh (such as temperature and velocity) have to be passed from the stationary mesh to the moving interface mesh as well. This transfer of information (mapping) is done by applying Peskin's immersed boundary method [86].

While the Lagrangian interface mesh moves with the flow it gets distorted. To maintain accuracy, elements must either be deleted, when their size is getting too small, or have to be added to the interface mesh. There exist two different approaches to maintain uniformly distributed element sizes: The classical approach, where elements are removed and added, as well as the approach of periodic reconstruction of the interface (level contour reconstruction method). In the classical approach, the logical element connectivity between discrete elements has to be maintained. This makes the code more complex, especially in cases where droplets and bubbles frequently breakup and coalesce. Nevertheless, the classical method shows highest accuracy. In the level contour reconstruction method (LCRM) the interface elements are periodically discarded and then reconstructed on a level contour of the indicator function I [74, 87]. This method has the advantage that the logical element connectivity has no longer to be maintained. In the present simulation both approaches were applied. For the calculation of the surface tension force a hybrid calculation method is used. This method combines the conventional Lagrangian Front Tracking and the Eulerian VOF-CSF approach to calculate surface tension. A detailed description of the calculation of the surface tension force can be found in reference [74]. The Front Tracking program and numerical algorithms used herein were previously thoroughly validated in different numerical studies [74,88]. Further results of the validation can be found in Appendix B. Grid independence was insured in parametric studies, resulting in an optimal number of 30×990 grid cells, as can be seen in Figure 4.2. Here, the velocity of a single droplet moving through a microchannel is plotted for different grid sizes. The fluid within the droplet is 5 cs silicon oil. It is surrounded by water. It can be seen that 3×10^4 grid cells (30×990) give sufficiently accurate results of the droplet velocity. In order to save computational costs, the time step size was varied during the calculations.

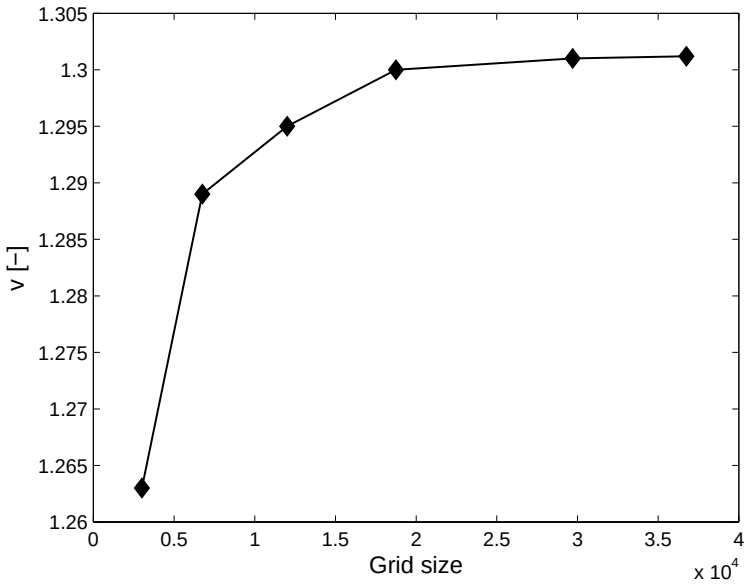

Figure 4.2: Dimensionless velocity of a single spherical silicon oil droplet moving through a microchannel for different grid sizes. The velocity is scaled by the mean velocity of the base fluid, which is water.

4.4 Results and Discussion

The heat transfer in the fluid was investigated for different flow conditions and fluid systems. The fluids used in this study are water, 5 cs silicon oil and polyalphaolefine (PAO). The nanofluid in the droplet is a mixture of Al_2O_3 nanoparticles either suspended in water or PAO. The initial volumetric concentration of particles in the solvent is 3%. The fluid properties used herein are presented in Table 4.1. Interfacial tension values of the water-silicon oil system were estimated based on the model of Girifalco and Good [89] combined with literature values of the pure and combined phases [90], [91]. This results in an interfacial tension of $38\,\mathrm{mN\,m^{-1}}$ at 300 K and a temperature coefficient σ_T of $0.06\,\mathrm{mN\,m^{-1}\,K^{-1}}$. Due to the lack of clear data for interfacial tension, the same values were chosen for water-PAO as well. Reliable data does not exist for the interfacial tension between nanofluids of Al_2O_3 particles and water or silicon. However, Murshed et. al. measured experimentally

the temperature dependent interfacial tension of TiO_2-water nanofluids in oil [92]. In their study, they reported a significantly reduced interfacial tension in the presence of nanoparticles. Following their results, the interfacial tension in the presence of nanoparticles was reduced by 25%.

Table 4.1: Physical properties of the liquids and the Al_2O_3 -nanoparticles used in the calculations. ρ, μ, λ and c are the density, dynamic viscosity, thermal conductivity and specific heat.

Fluid/Solid	ρ ($\mathrm{kg\,m^{-3}}$)	μ (Pa s)	λ ($\mathrm{W\,m^{-1}\,K^{-1}}$)	c ($\mathrm{J\,kg^{-1}\,K^{-1}}$)	Ref.
Water	1.0×10^3	1.0×10^{-3}	6.0×10^{-1}	4.2×10^3	-
Silicon Oil (5 cs)	9.1×10^2	4.6×10^{-3}	1.2×10^{-1}	1.5×10^3	[91]
PAO	8.0×10^2	5.0×10^{-3}	1.3×10^{-1}	2.3×10^3	[93]
Al_2O_3	4.0×10^3	-	4.0×10^1	7.7×10^2	[94]

We identified the Reynolds number, the Capillary number ($Ca_i = We_i/Re_i$) and the Peclet number ($Pe_i = Re_i\,Pr_i$) in both liquids as well as the viscosity ratio μ_1/μ_2 as being the relevant dimensionless groups, which determine the thermal transport in micro channels. The heat transfer can be expressed in terms of the local Nusselt number in the axial direction, which is defined as:

$$Nu_z = \frac{2R_0\; q|_{wall,z}}{\lambda\,(T_b - T_{wall,z})} = \frac{2\;\frac{\partial\theta}{\partial x}\big|_{wall,z}}{(\theta_{wall,z} - \theta_b)}. \tag{4.25}$$

R_0 T_b and θ_b are the pipe radius and the dimensional and dimensionless local bulk mean temperature, respectively. The local bulk mean temperature can be calculated in accordance with [95] as:

$$\theta_b = \frac{\int_0^1 \rho^* c^* u_z \theta\, x\, dx}{\int_0^1 \rho^* c^* u_z x\, dx}. \tag{4.26}$$

In equation 4.26 all fluid properties as well as the temperature and the axial velocity are a function of the radial position. The calculated local Nusselt number for single liquid flow can be validated with an approximated solution of the Graetz problem. In the case of constant wall temperature, the Nusselt number in the early part of

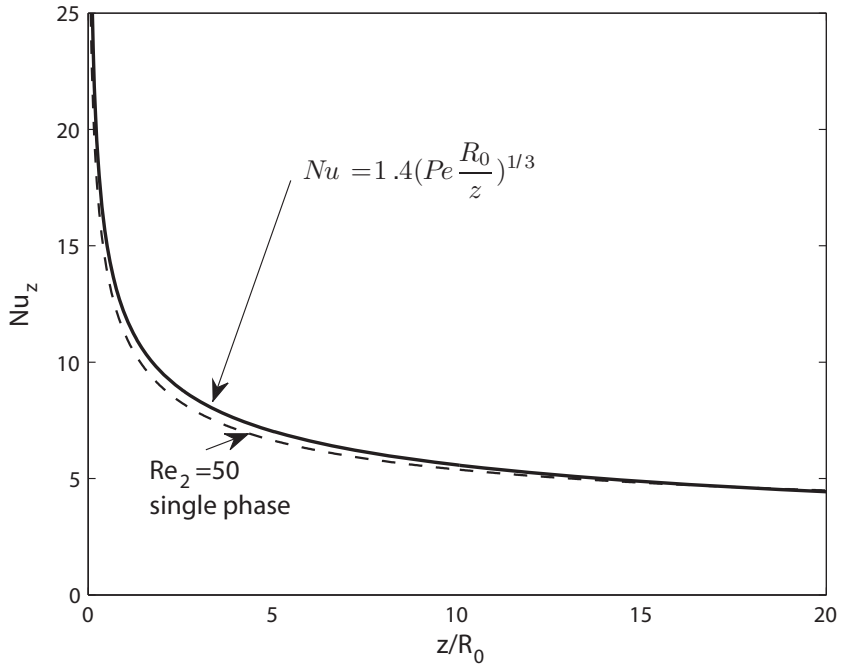

Figure 4.3: The calculated local Nusselt number distribution, compared to the approximated solution, Eq.4.27.

the thermal entrance region can be approximated as, [96]:

$$Nu = 1.357 \left(Pe \frac{R_0}{z} \right)^{1/3}. \tag{4.27}$$

The calculated results and the Nusselt number obtained from equation 4.27 are plotted in Figure 4.3, showing good agreement. Slight differences at the entrance region are caused by the fact that the approximated solution is obtained by neglecting axial diffusion and by linearizing the velocity near the wall.

The local Nusselt number in the axial direction for a point in time along with the temperature distribution for a flow of nanofluid droplets (PAO and Al_2O_3 particles) in water is depicted in Figure 4.4. Here, the mean inlet velocity v_0 was set to 10 cm/s and the channel radius is 500 μm. This results in a Reynolds number of 50 and a Capillary number of 3.6×10^{-3} in the bulk fluid. Compared to single liquid flow, the Nusselt number is significantly higher in the present two liquid flow arrangement.

In the presence of liquid droplets, the local Nusselt number exhibits two peaks; in

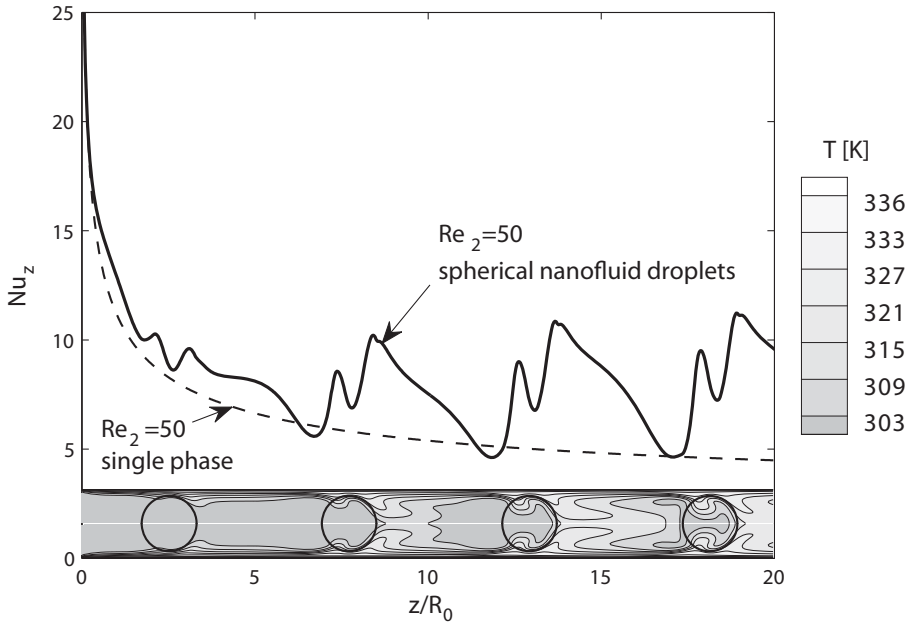

Figure 4.4: Local Nusselt number and temperature field (in Kelvin) in axial direction for liquid-liquid flow with spherical droplets. The dashed line compares to the Nusselt number of a single fluid flow.

the bulk liquid in front of the droplet and in the rear of the droplet. The droplets are moving 1.2 times faster than the bulk fluid. Thus, a recirculation zone develops between the droplets. In the wake of the droplets the Nusselt number decays, as cold fluid is pulled towards the tail. In front of the droplets a blockage effect occurs and hot fluid is transported from the wall towards the center of the channel. In this region the Nusselt number increases and exhibits the maximum value of 12. The second, lower peak in the rear of the droplets is caused by slight recirculation within the droplet, as is shown in Figure 4.5.

To explore the influence of the recirculation on the wall thermal layer, streamlines and the temperature distribution of both cases are depicted in Figure 4.5. The wall temperature was set to 340 K. Dark areas represent low temperature values. The streamlines are plotted in a reference frame moving with the fluid flow (Figure 4.5b). In Figure 4.5a it can be seen that the wall thermal layer is affected at two distinct positions. In front of the droplet hot fluid from the wall is dragged with the

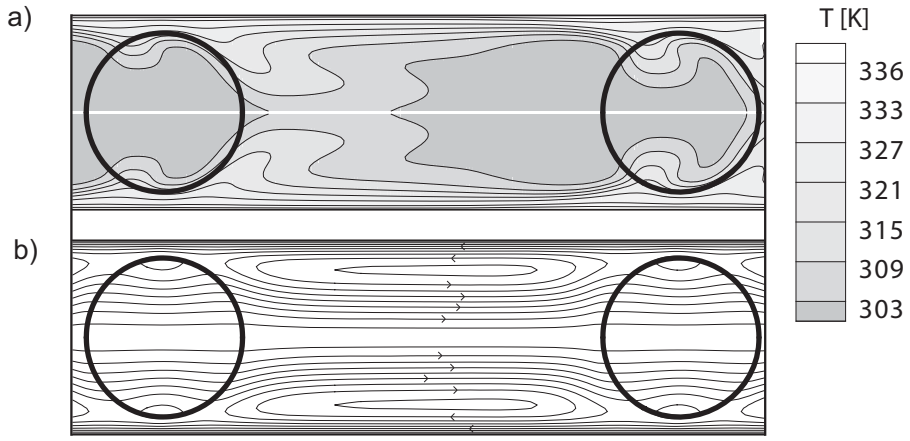

Figure 4.5: Temperature field in Kelvin (a) and streamlines in a moving reference frame (b) for nanofluid droplet-laden flow. The liquids used are water as the base fluid and PAO and Al_2O_3-nanoparticles as the suspended liquid.

circulating flow towards the center of the channel. Here, the circulating flow between the two droplets (indicated by the velocity vectors) affects the thermal transport. Within the droplet, the recirculation is less pronounced. However, the wall thermal layer is disturbed in the rear of the droplets, where convective transport away from the channel wall takes place.

The Nusselt number can be further increased by establishing an elongated droplet or slug flow in the channel, Figure 4.6. As in the previous case, the liquids are chosen to be water (main flow) and a nanofluid of PAO and Al_2O_3. The velocity and the channel radius are the same as in Figures 4.4 and 4.5. Compared to the case with only spherical droplets, a further rise of the Nusselt number can be verified. The Nusselt number triples compared to single liquid flow. Peak values are as high as 25. Due to the higher blockage effect, the recirculation inside and between the slugs is more pronounced. The profile exhibits again two peaks in front and in the wake of the slugs, where the wall thermal layer is affected. The decreased heat transfer within the droplets is a reason of the lower specific heat and thermal conductivity of the nanofluid compared to the aqueous bulk fluid.

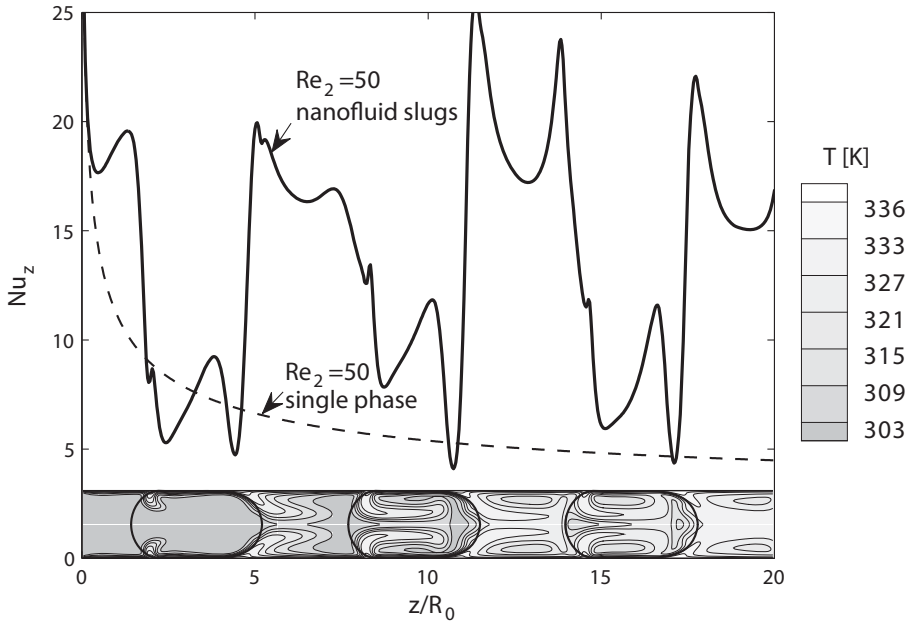

Figure 4.6: Local Nusselt number and the temperature field in Kelvin in axial direction for liquid-liquid flow with elongated droplets. The dashed line compares to the Nusselt number of a single liquid flow.

In slug flow, vortices within and between the droplets are more pronounced, Figure 4.7b. The wall thermal layer is affected at the same positions as in the case of spherical droplets (Figure 4.7a). However, the convective thermal transport is noticeably higher. The particle distribution within the slugs is depicted in Figure 4.7c. High particle concentrations are illustrated by dark colors. Two effects can be identified: The particles are transported in a convective manner along the fluid flow in the droplet. In addition, the particles experience a thermophoretic force, pushing them towards colder regions of the droplet. This effect can be seen in the very center of the droplet where particles accumulate due to lower temperatures. Since concentration gradients are smoothed out by the counteracting Brownian diffusion, both effects are rather small. Depending on the position of the slug, the particle concentration is only changed by 0.5 to 5%.

The influence of varying Reynolds numbers on the heat transfer is shown in Figure 4.8, where the local Nusselt number, averaged over time, $\overline{Nu_z}$ in the axial direction

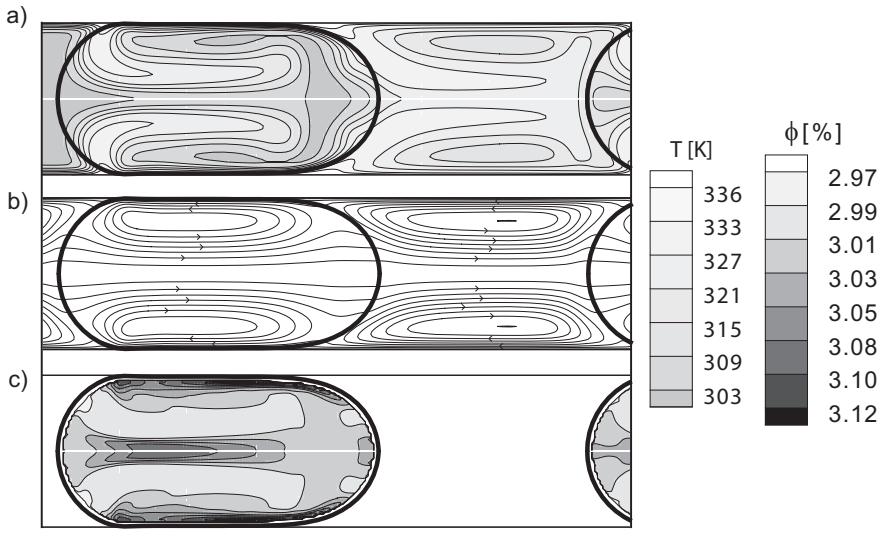

Figure 4.7: Temperature field in Kelvin (a), streamlines in a moving reference frame (b) and the particle concentration (c) for liquid slug flow. The liquids used, are water as the base fluid and PAO and Al_2O_3-nanoparticles as the suspended liquid.

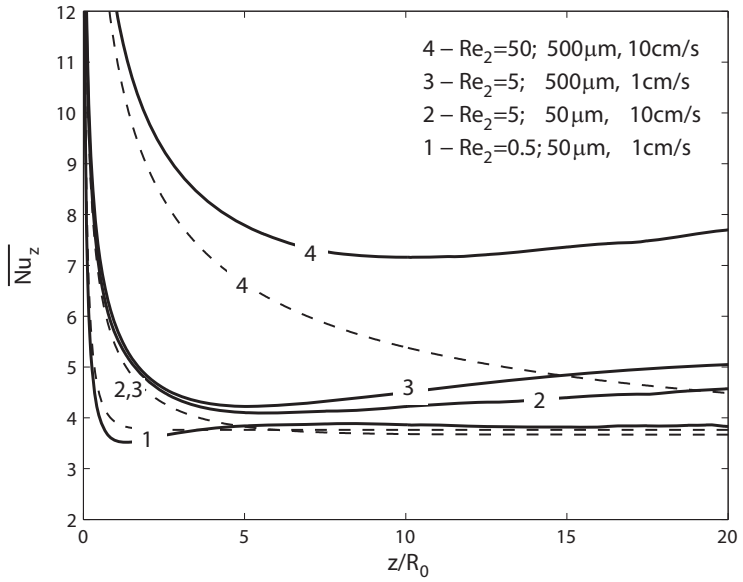

Figure 4.8: Temporally averaged Nusselt number for different radii and velocities. The liquid in the droplet is 5 cs silicon oil. It is surrounded by water. The dashed lines indicate the solution for aqueous single liquid flow.

for different flow conditions is depicted. The Nusselt number is averaged over the time period a train of 10 droplets needs to move through the channel. For the cases shown here, the liquid within the droplets is 5 cs silicon oil surrounded by water. The mean inlet velocity and the radius are varied between 1 and 10 cm/s and 50 μm and 500 μm, respectively. Compared to single liquid flow (dashed lines) a higher cooling performance can be detected for all cases. At high Reynolds numbers (Re_2=50) the Nusselt number nearly doubles. Also for lower Reynolds numbers a significant augmentation can be detected. Cases 2 and 3 reveal that not only the Reynolds and Peclet numbers have an influence on the heat transfer performance of the microchannel. Both the Peclet and Reynolds numbers are identical in these cases (Re_2=5, Pe_2=35). Different Capillary numbers ($Ca_2=2.7\times10^{-4}$ for case 2, $Ca_2=2.7\times10^{-3}$ for case 3) show that the influence of the surface tension cannot automatically be neglected in micro scale heat transfer devices. For the cases 2 to 4 the Nusselt number increases and reaches a plateau value at the end of the channel (z/R_0=20). This non-monotonic behavior is caused by the fact that the droplet flow is affecting the thermal wall layer. As will be seen later, this effect is even stronger for slug flow, Figure 4.12. For low Reynolds numbers, Re_2=0.5 in the bulk fluid and Re_1=0.1 in the droplet, the profile exhibits an initial dent at the thermal entrance region, case 1 in Figure 4.8. This dent can be explained by Marangoni effects. The initially high surface tension gradients, along the interface between the liquids at the entrance region results in a Marangoni force. This force acts against the circulating flow at the interface of the droplets, as fluid is pushed towards regions with lower temperature. The low Capillary numbers for the droplet ($Ca_1=1.2\times10^{-3}$) and the bulk fluid ($Ca_2=2.7\times10^{-4}$) emphasize this strong influence of surface tension Marangoni forces.

For higher Reynolds numbers, the Marangoni effect cannot be neglected either. This can be seen in Figure 4.9, where calculations applying constant interfacial tension are compared to runs with temperature dependent interfacial tension. In all cases the Nusselt number is higher, when constant interfacial tension is assumed.

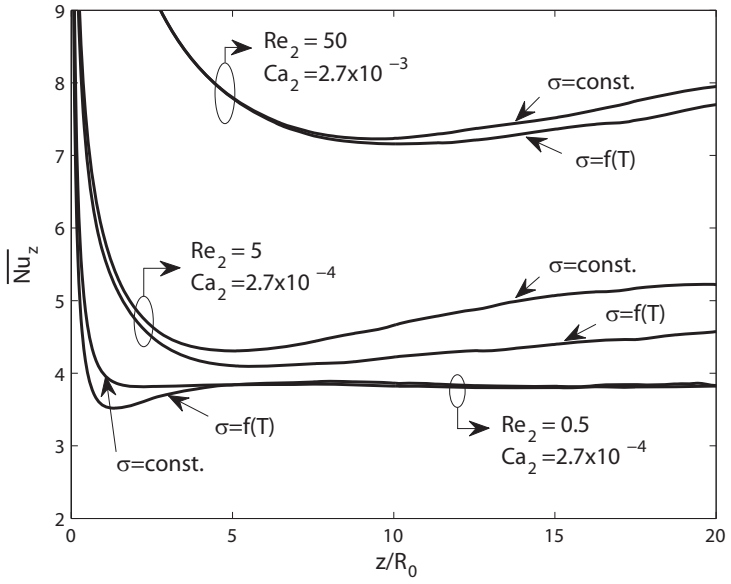

Figure 4.9: Nusselt number distribution for different cases with constant surface tension compared to calculations where the Marangoni effect is included ($\sigma = f(T)$). The liquid in the droplet is 5 cs silicon oil, surrounded by water.

It follows that the Marangoni effect, i.e. the dependency of interfacial tension on temperature, decreases the heat transfer performance of microchannel two liquid flow. The Marangoni force resulting form temperature gradients at the interface counteracts the swirling motion of the fluid flow.

This effect can be explained with the help of Figure 4.10. The temperature gradient near the channel centerline in front and at the rear of the droplet, results in a variation of the temperature-dependent surface tension (bottom half of Figure 4.10). At both ends of the droplet the gradient in surface tension causes a Marangoni force at the interface, which is directing fluid towards the centerline of the channel. In front of the droplet this force aids the rotational motion of the fluid outside the droplet (top half of Figure 4.10). However, in the rear of the droplet a steeper temperature gradient results in a higher Marangoni force counteracting the rotational motion of the surrounding fluid towards the channel wall. The net result of both effects is a decreased rotational motion of the fluid in between two sequential droplets. For

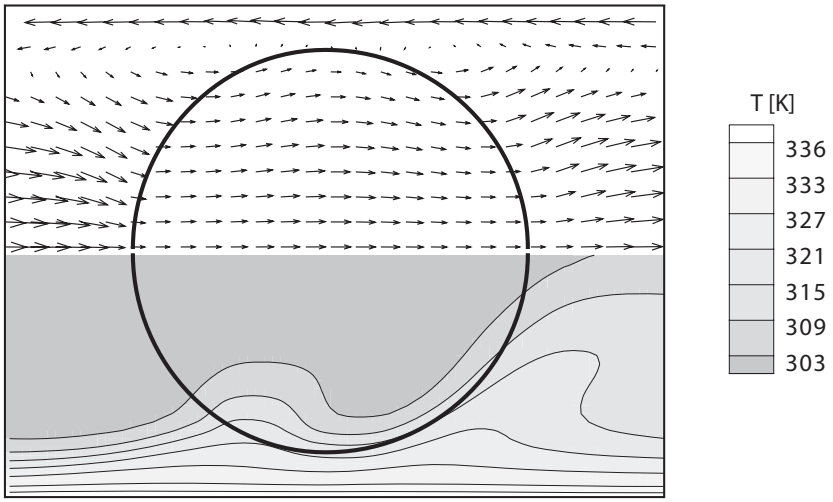

Figure 4.10: Velocity vectors in a moving reference frame (top) and the temperature field (bottom) around a single spherical droplet.

moderate Reynolds numbers of 5 this effect is rather high; here the Nusselt number changes by 13%. For Reynolds numbers of 50 a 4% change can still be detected. In the case of low Reynolds numbers (Re_2=0.5) the temperature gradients decrease already after 4 to 5 radii. Therefore, the Marangoni force only plays a role at the very beginning of the entrance region. In all cases shown here the Nusselt number remains significantly higher than that of single liquid flow.

The positive influence of nanoparticles on the heat transfer performance in microchannels is shown in Figure 4.11. In Figure 4.11a the bulk fluid is 5cs silicon oil, in which spherical water droplets are immersed. In Figure 4.11b similar results are shown for slugs of polyalaphaolefine in water. In both cases the Reynolds numbers are chosen to vary between 5 and 50. To asses the influence of nanoparticles, Al_2O_3 particles are suspended into the droplet liquid. In Figure 4.11a it can be seen that in the presence of nanoparticles the local Nusselt number increases by 3 to 5% compared to the case of pure fluids. Here, the augmentation effect of nanoparticles increases for higher Reynolds numbers. As already mentioned earlier, the surface tension of nanofluids is smaller compared to pure fluids. This results in somewhat higher Capillary numbers, supporting the effect of nanoparticles on the

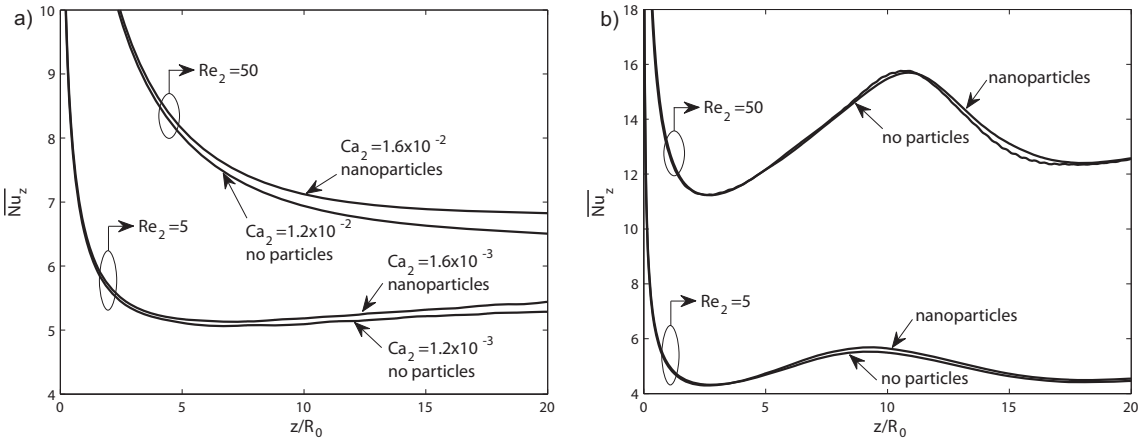

Figure 4.11: The effect of nanoparticles on the temporally averaged local Nusselt number. In (a) the carrier liquid is 5 cs silicon oil, the liquid in the droplets is water with and without nanoparticles. In (b) similar results are shown for slug flow, where the carrier liquid is water and the liquid in the droplet is PAO with and without nanoparticles.

heat transfer. To further investigate this phenomenon calculations were performed, where the surface tension was kept constant, Figure 4.11b. Here the Nusselt number only increases by 1.5% in the presence of nanoparticles. It can be concluded, that the nanoparticles mainly improve the thermal transport by lowering the effective interfacial tension of the droplets. The positive effect caused by increased thermal properties, such as thermal conductivity or specific heat is marginal.

The peaks in the profile of the temporally averaged Nusselt number in Figure 4.11b is caused by the strong impact of slug flow on the wall thermal layer. First, when entering the heated section of the channel, the colder slug pushes the hot liquid of the wall thermal layer away. Due to the strong recirculation within and between subsequent slugs, hot liquid is transported to the centerline of the flow. At the same time, cold fluid from the centerline region flows towards the hot wall, causing steep temperature gradients at the channel wall. This effect goes on until the first warm fluid particle in the vertex reaches the wall again (Figure 4.6).

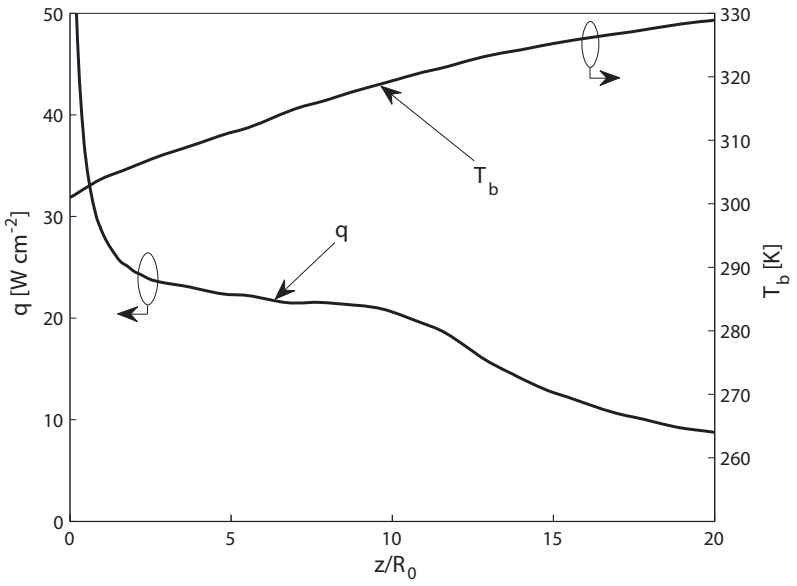

Figure 4.12: Bulk mean temperature and the heat flux from the wall in axial direction, as defined by Eqs.(21) and (22).

This is the case after the slug has covered a distance of 11 radii. After this position, the temperature gradient (and the Nusselt number) decreases. This can be seen in Figure 4.12, where the temporally averaged heat flux q as well as the temporally averaged mean bulk temperature, Eq. 4.26 are plotted. The heat flux shows a slightly decreasing plateau until $z/R_0 = 11$, which is caused by the near constant temperature gradient at the wall. After $z/R_0 = 11$, the temperature gradients and in turn the heat flux decreases. Since the bulk mean temperature is constantly increasing, while the heat flux is nearly constant in the first part of the heated section, the Nusselt number, Eq.4.25, increases as well exhibiting a peak value at $z/R_0 = 11$.

Another possibility for considerably increasing the thermal performance of the microchannel flow is to use droplets of higher viscosity, as is shown in Figure 4.13. Here, the viscosity of the droplets is changed by using different types of silicon oil. The bulk fluid is water. The viscosity of the oil is 0.5, 5 or 50 cs. This results in

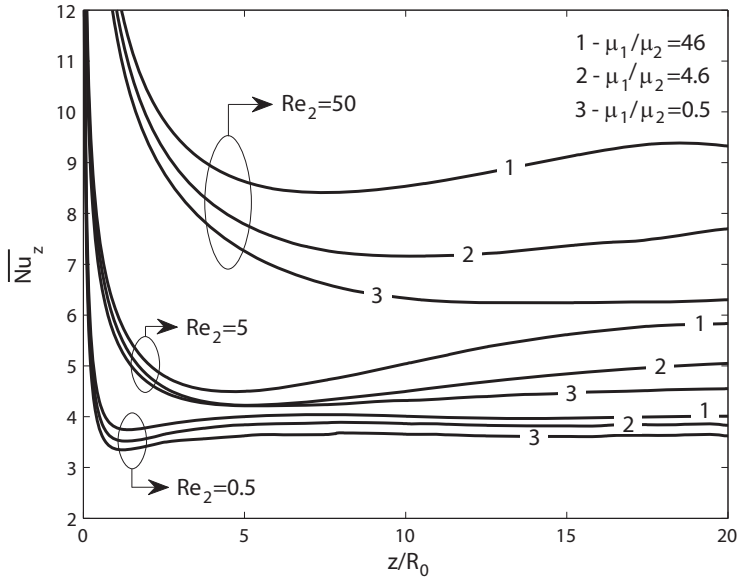

Figure 4.13: Temporally averaged Nusselt number distribution for different viscosity ratios μ_1/μ_2 and Reynolds numbers of the bulk fluid Re_2.

viscosity ratios μ_1/μ_2 of 0.5, 4.6 and 46 for high viscous silicon oils. It can be seen that the Nusselt number strongly depends on the viscosity ratio of the two phases. In the case of higher Reynolds numbers of the bulk fluid (Re_2=50), the influence is particularly strong. Here, the Nusselt number more than doubles compared to single liquid flow. For low Reynolds (Re_2=0.5) the influence is lower, but high viscosity ratios still increase the heat transfer performance of the liquid-liquid flow by 5%. High viscosity droplets move slower, compared to droplets with low viscosity. The velocity of the less viscous droplets is 1.4 times higher than the mean velocity of the carrier liquid. Highly viscous droplets move only 1.2 times faster then the bulk fluid. However, due to the high viscosity ratio between the two liquids, the circulating motion of the fluid is significantly increased. As will be seen later, this results in a slightly increased pressure drop (Figure 4.15).

From previous research on gas-liquid flow it is known that the heat transfer of slug flow is considerably higher compared to bubbly flow [16]. In two-liquid flow similar

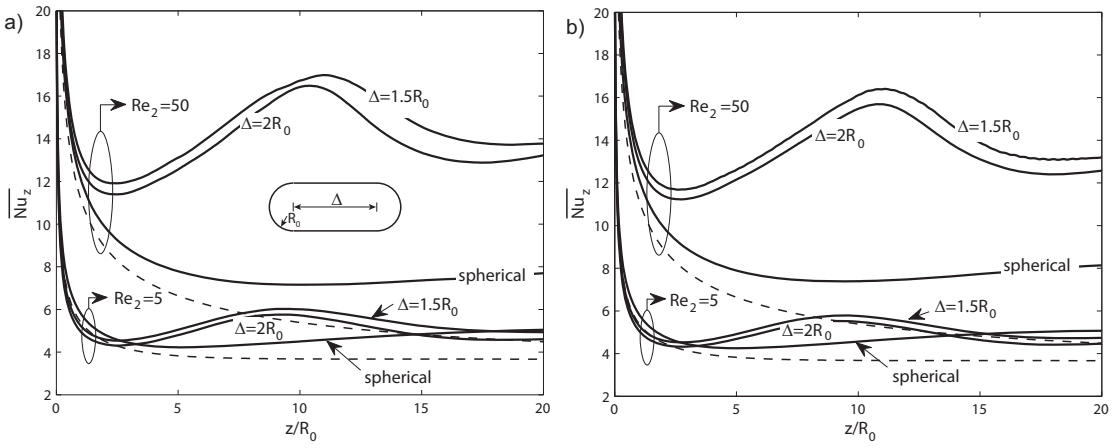

Figure 4.14: Temporally averaged Nusselt number distribution for differently shaped droplets. The fluids used for the droplet liquid are 5 cs silicon oil (a) and nanofluid of PAO and Al_2O_3 particles (b). In both cases, the base fluid is water. The dashed line compares to the Nusselt number of single liquid flow.

results can be obtained, as is shown in Figure 4.14. Here, the temporally averaged Nusselt number distribution is shown for differently shaped droplets. In Figure 4.14a results are presented for droplets of 5 cs silicon oil; in Figure 4.14b polyalphaolefine and Al_2O_3 nanoparticles are used. In both cases, the base fluid is water. For both liquid configurations the heat transfer is strongly increased in the case when the Reynolds number is 50. Peak values of 17 for the Nusselt number can be achieved when the elongation of the slug is $1.5\,R_0$. For longer slugs ($2\,R_0$) the Nusselt number drops again, as the amount of the suspended liquid (liquid 1) increases. The thermal properties of the suspension liquid are less adequate for thermal transport compared to the surrounding water. For low Reynolds numbers (Re_2=5) the influence of capillary forces is higher compared to viscous forces, resulting in a minor influence of the droplet shape.

The increase in thermal transport in slug flow is mainly caused by stronger recirculation between and within the slugs, which is in turn caused by the velocity difference between slugs and the carrier liquid. In slug flow, the mean velocity of the bulk

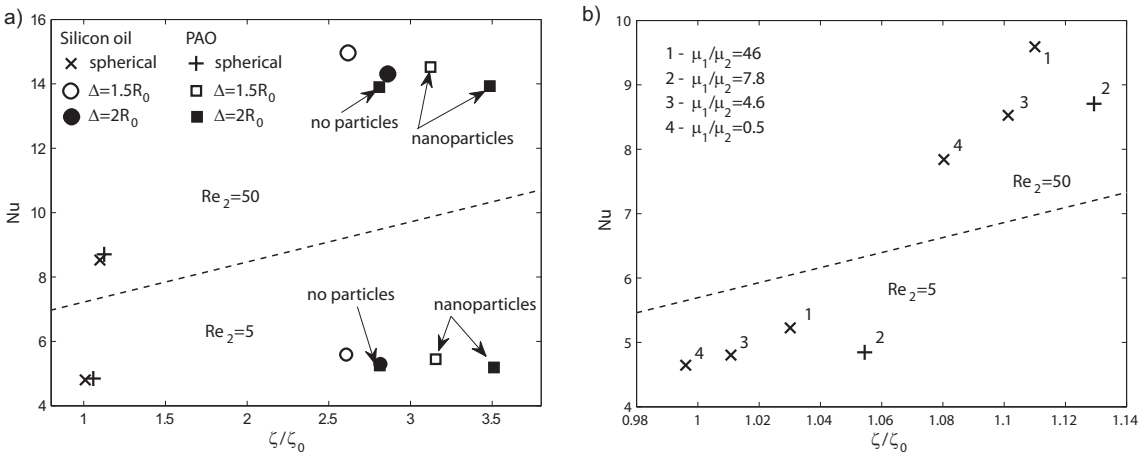

Figure 4.15: Nusselt number vs. pressure drop normalized by the pressure drop of one liquid flow. a) Nusselt number for differently shaped droplets, with and without nanoparticles. b) Nusselt number for spherical droplets with different viscosity ratios μ_1/μ_2 . In b), the liquids are either PAO (+) or silicon oil (×). The dashed line separates high Reynolds number flow (Re_2=50) from lower Reynolds number flow (Re_2=5).

fluid experiences a further drop. It follows that the increase in heat transfer in slug flow is achieved at the expense of a higher pressure drop. In the present study the pressure drop along the channel triples for slug flow compared to spherical droplet laden flow, as is shown in Figure 4.15.

In Figure 4.15 the mean Nusselt number over the non-dimensional pressure drop ($\zeta = \Delta p/0.5\rho_2 v_0^2$), normalized by the pressure drop of a single liquid ζ_0 (water) is depicted for two different scenarios. The Nusselt number is averaged over the length of the heated section of the channel and the time period needed so that 10 subsequent droplets move through the channel. In Figure 4.15a the friction losses of differently shaped droplets of different liquids are compared. It can be seen that the heat transfer in slug flow is considerably higher compared to single liquid flow (increase of the Nusselt number is nearly 400%). The best cooling performance is obtained for slugs of 5 cs silicon oil. Here, the Nusselt number is 15 for a channel

with a radius of 500 μm. However, higher Nusselt numbers in slug flow are strongly connected to an increased pressure drop, which triples for slug flow compared to spherical droplet flow. Figure 4.15a reveals that the pressure drop further increases in the presence of nanoparticles, even though the positive effect of nanoparticles on the thermal performance is minor.

Another possibility for increasing the thermal performance of a microchannel is to use higher viscosity droplets. Figure 4.15b shows that the Nusselt number can be increased to 9.6, when using 50 cs Silicon oil ($\mu_1/\mu_2 = 46$) as the droplet liquid. The pressure drop increases by only 11% compared to a single fluid whereas the Nusselt number more than doubles. Again, in Figure 4.15 it can be seen that the use of a nanofluid (PAO with nanoparticles) increases the Nusselt number at the expense of a significant pressure drop increase.

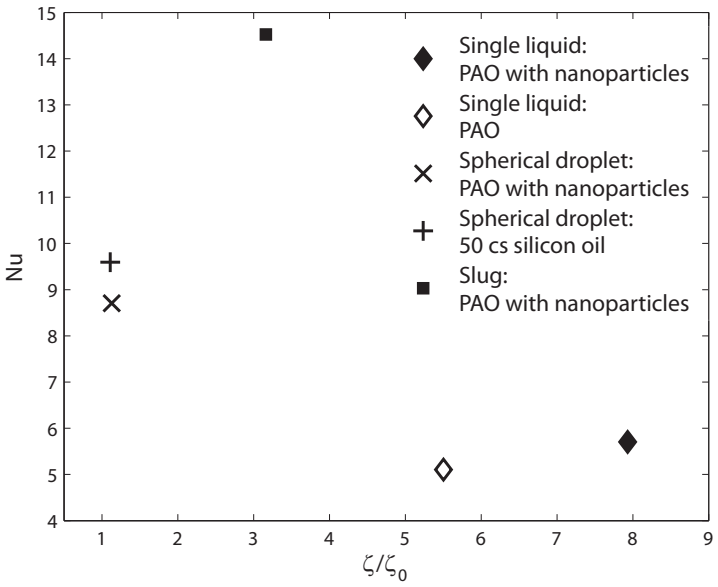

Figure 4.16: Nusselt number vs. pressure drop normalized by the pressure drop of one liquid flow (water).

To further elaborate on the effect of nanoparticles on the friction losses, the Nusselt number of single and two liquid flow is plotted in Figure 4.16. As expected, Figure 4.16 reveals that suspended nanoparticles in single liquid flow of polyalphaolefine

(PAO) increase the Nusselt number by nearly 12 %. However, when using PAO as a coolant liquid, the pressure drop is augmented by a factor of 5.5 compared to the case when the cooling liquid is water. This is caused by the higher viscosity of PAO. In the presence of nanoparticles the pressure drop rises even further by as much as 44%. By comparing to the results of spherical droplet or slug flow, it can be seen that the use of a second, suspended liquid (with and without nanoparticles) is an efficient way to increase the thermal performance without unacceptable pressure losses. Moreover, using nanofluids as an immiscible suspended liquid in a two liquid flow configuration instead of a one liquid flow of nanofluids, eliminates the unwanted fouling effect which is present in every particle laden flow.

4.5 Conclusions

In this chapter, the thermal transport of liquid-liquid flow through micro channels was investigated for different flow conditions. A comprehensive model was presented, combining nanoparticle transport and nanofluidic heat transfer with a Front Tracking algorithm to capture multiphase flow and interfacial effects.

It was observed that the influence of surface tension strongly affects the thermal transport mechanisms present in low Reynolds number flow. It was shown that the Marangoni effect, decreases the heat transfer performance of microchannel two liquid segmented flow. The Marangoni force resulting form temperature gradients at the interface counteracts the swirling motion of the fluid flow. Depending on the flow conditions the Nusselt number decreases by as much as 13%.

A positive effect of nanoparticles on the heat transfer performance in microchannels was detected. In the presence of nanoparticles the thermal transport was increased by only 3 to 5%. This is mainly caused by the fact, that nanoparticles lower the effective interfacial tension of the fluids. Lower surface tension results in a higher Capillary number, which supports the marginal effect of increased thermal properties

of the nanofluid on the heat transfer.

In a second step the influence of differently shaped droplets on the heat transfer was investigated. It was observed that the Nusselt number considerably increases in the presence of slug flow compared to flow of spherical droplets. This effect is primarily dominant for higher Reynolds numbers (Re=50). Here, the best performance was detected for 5 cs silicon oil, where the Nusselt number reached the vaue of 15. For lower Reynolds numbers (Re=5) the increase in thermal transport is less pronounced. It was seen that the increase in heat transfer in slug flow is generally achieved at the expense of a higher pressure drop. When the two effects need to be considered together, desirable operation regimes can be designed.

The most promising approach to considerably increase the thermal performance of microchannel flow with a moderate increase in friction losses is to use droplets of higher viscosity. The strong influence of the viscosity ratio between the two liquids on the Nusselt number was shown. In the case of higher Reynolds numbers, the influence is particularly strong. Here, for a viscosity ratio of 50 the Nusselt number more than doubles compared to single liquid flow. In this case, the pressure drop increases by only 11%. For low Reynolds numbers the influence of the viscosity is lower, but high viscosity ratios still increase the thermal transport within the flow. In the case of nanofluids, the segmented "droplet train" approach showed clear advantages over forced convection of only the nanofluid in the microchannel.

Chapter 5

Conclusions

This work presented theoretical and numerical investigations on the underlying thermophysical phenomena in microfluidic appliances. In order to study the different physical effects present in small scales, the diffusive shrinking of nanoink droplets into a surrounding liquid, the dissolution of oxygen bubbles in blood and the thermal transport in droplet laden liquid-liquid flow through microchannels were investigated.

In chapter 2 the shrinking process of a gold nanoink droplet surrounded by a secondary liquid (water) was investigated for different thermal conditions. A spherically symmetric model was presented and analytical solutions for the velocity and pressure field were derived. A numerical scheme based on the Finite Difference Method was introduced in order to solve the temperature and concentration fields in a moving computational domain.

The strong effect of thermal energy on the shrinking process was demonstrated by heating the surrounding water phase. It was observed that the shrinking process is directly related to the increased solubility of toluene at higher temperatures and to the concentration gradients at the interface with the surrounding liquid phase. Consequently, the shrinking can be significantly accelerated by heating up the surrounding phase. When the outer phase was set to an initial temperature in the range

of 50 to 70 °C, the velocity of the interface was found to increase by a factor of two to three and the shrinking time could be reduced by 50 to 80% when compared to isothermal conditions.

Another way to enhance the shrinking is the heating of the nanoink droplet. Here the shrinking time can be reduced by a factor of two to three when compared to the isothermal case. When the droplet is heated with a laser, similar shrinking times could be detected. In the presence of a heat source, a strong gradient of particle concentration was detected near the interface, which was mainly caused by the thermophoretic force pushing the particles towards the colder interface. In this situation thermophoresis dominates the counteracting Brownian diffusion which typically smoothes out strong concentration gradients.

The influence of thermophoresis and Brownian diffusion of nanoparticles on the thermal transport and the particle distribution was demonstrated by comparing a nanoink droplet to a pure toluene droplet without particles. A clearly enhanced thermal transport in the nanoink droplet was observed.

The model introduced in Chapter 2 was adopted and extended in order to describe the dissolution of oxygen microbubbles in blood in Chapter 3. The derived methodology was validated by radius-time relationships reported in literature for the collapse of similar microbubbles.

The results of the simulations were used to examine the quasi-steady assumption of the Epstein-Plesset model, which is commonly employed in the analysis of bubble dissolution. Compared to the herein introduced fully coupled numerical model, the Epstein-Plesset solution leads to an approximately 8% shorter collapse time. The simulation of the oxygen uptake reaction results in reduced collapse time of about 30%, when compared to the predictions of the Epstein-Plesset model which neglects chemical reactions.

A parametric study was conducted to model the dissolution of microbubbles under

various physiological conditions, showing that the collapse time may vary from ten seconds to two or three hours, depending on the size of the bubbles and the parameters which specify the blood conditions. It was shown that the calculated collapse time gives a valuable estimate of the lower bound dissolution time of a spherical bubble in blood.

Finally, in Chapter 4 the thermal transport of liquid-liquid flow through micro channels was investigated for different flow conditions. The presented model combined nanoparticle transport and nanofluidic heat transfer with a Front Tracking algorithm to capture multiphase flow dynamics, as well as interfacial effects.

Parametric studies revealed the strong effect of interfacial tension on the radial heat transfer in microscale applications. It was observed that the influence of surface tension strongly affects the thermal transport mechanisms present in low Reynolds number flow. Depending on the flow conditions, the Nusselt number decreases by as much as 13% under the influence of the Marangoni effect. The Marangoni force, caused by temperature gradients at the interface, reduces the heat transfer performance of a slug or droplet flow by counteracting the swirling motion of the fluid flow.

A positive, but rather small effect of nanoparticles on the heat transfer performance in microchannels was detected. In the presence of nanoparticles the thermal transport was increased by only 3 to 5%. This is mainly due to the fact that nanoparticles lower the effective interfacial tension of fluids. Lower surface tension results in a higher Capillary number, which supports the marginal effect of increased thermal properties of a nanofluid on heat transfer.

Another possibility for increasing the thermal performance of two liquid flow is to increase the flow rate of the suspended liquid. The Nusselt number considerably increases in the presence of slug flow when compared to a flow of spherical droplets. This effect is primarily dominant at higher Reynolds numbers (Re=50). The best performance was detected for 5 cs silicon oil, where the Nusselt number reaches a

value of 15. For low Reynolds numbers (Re=5) the increase in thermal transport is less pronounced. It was shown that the increase in heat transfer in slug flow is generally achieved at the expense of a higher pressure drop, which more than doubles.

The most promising approach to considerably increase the thermal performance of microchannel flow, accepting a moderate increase in friction losses, is to use droplets of higher viscosity. A strong influence of the viscosity ratio between the two liquids on the Nusselt number was shown. In the case of high Reynolds numbers, the influence is particularly strong. Here, for a viscosity ratio of 50 the Nusselt number more than doubles when compared to single liquid flow, while the pressure drop only increases by 11%. For low Reynolds numbers the influence of viscosity is lower, but high ratios may still increase the thermal transport within the flow.

Nomenclature

Latin Letters

A	Droplet surface (m^2)
c	Heat capacity ($J\,kg^{-1}\,K^{-1}$)
C_b	Mass fraction of bound oxygen (-)
C_d	Mass fraction of dissolved oxygen (-)
C_t	Mass fraction of oxygen in blood (-)
c_H	Hemoglobin binding capacity $(ml\,O_2)(ml\,blood)^{-1}$
D	Diffusivity coefficient ($m^2\,s^{-1}$)
D_B	Brownian diffusion coefficient ($m^2\,s^{-1}$)
D_F	Facilitated diffusivity coefficient ($m^2\,s^{-1}$)
D_T	Thermal diffusion coefficient ($m^2\,s^{-1}$)
D_{WT}	Diffusion coefficient, water in toluene ($m^2\,s^{-1}$)
E	Energy (J)
e	Internal energy ($J\,kg^{-1}$)
$\mathbf{F}$	Interfacial tension force per unit volume ($N\,m^{-3}$)
h	Enthalpy ($J\,kg^{-1}$)
j	Mass flux density ($kg\,m^{-2}\,s^{-1}$)
L	Length scale (m)
L_D	Length of the computational domain (m)
$\dot{m}$	Mass flow ($kg\,s^{-1}$)
m	Mass (kg)
n	Parameter of Hill's equation (-)
P_{50}	Parameter of Hill's equation (mmHg)
p ,$\wp$	Pressure (Pa), (-)
q_S	Source term ($W\,m^{-3}$)
r ,x	Radial coordinate (m), (-)
R ,X	Droplet, bubble radius (m), (-)

R_0	Channel radius (m)
$\dot{R}$,$\dot{X}$	Velocity of the interface ($\mathrm{m\,s^{-1}}$), (-)
S	Oxygen saturation (-)
T	Temperature (K)
T_C	Collapse time (s)
ΔT	Temperature scale (K)
t	Time (s)
u	Velocity ($\mathrm{m\,s^{-1}}$)
$\mathbf{u}, \mathbf{v}$	Velocity vector ($\mathrm{m\,s^{-1}}$), (-)
V_{O2}	Volumetric content of oxygen in blood (-)
z	Axial coordinate (m)

Greek Letters

α	Solubility of oxygen $(\mathrm{ml\,O_2})(\mathrm{ml\,blood})^{-1}(\mathrm{mmHg})^{-1}$
δ	Phase thickness (-)
η	Radial Landau coordinate (-)
θ	Temperature (-)
κ	Curvature of the interface (m-1)
λ	Thermal conductivity ($\mathrm{W\,m^{-1}\,K^{-1}}$)
λ_S	Slope of the saturation curve (-)
μ	Dynamic viscosity ($\mathrm{kg\,m^{-1}\,s^{-1}}$)
ρ	Density ($\mathrm{kg\,m^{-3}}$)
ρ_b	Density of blood ($\mathrm{kg\,m^{-3}}$)
ρ_{STP}	Density of oxygen under standard conditions ($\mathrm{kg\,m^{-3}}$)
σ	Surface tension ($\mathrm{N\,m^{-1}}$)
σ_T	Temperature coefficient ($\mathrm{N\,m^{-1}\,K^{-1}}$)
τ	Time (-)
ψ ,ϕ	Volumetric fraction (-), (-)
Φ	Normalized mass fraction (-)

φ_T	Volumetric solubility of toluene in water (-)

Subscripts

b	Bulk
i	Phase index
IF	Interface
P	Particle
T	Toluene
W	Water
0	Initial
1	Phase 1, liquid 1: droplet liquid
2	Phase 2, liquid 2: base liquid
∞	Infinity

Superscripts

$*$	Dimensionless physical properties

List of Figures

List of Tables

Bibliography

[1] S. Arcidiacono, N. R. Bieri, D. Poulikakos, and C. P. Grigoropoulos. On the coalescence of gold nanoparticles. *International Journal of Multiphase Flow*, 30(7-8):979–994, 2004.

[2] P. Buffat and J. P. Borel. Size effect on melting temperature of gold particles. *Physical Review A*, 13(6):2287–2298, 1976.

[3] N. R. Bieri, J. Chung, D. Poulikakos, and C. P. Grigoropoulos. Manufacturing of nanoscale thickness gold lines by laser curing of a discretely deposited nanoparticle suspension. *Superlattices and Microstructures*, 35(3-6):437–444, 2004.

[4] N. R. Bieri, J. Chung, S. E. Haferl, D. Poulikakos, and C. P. Grigoropoulos. Microstructuring by printing and laser curing of nanoparticle solutions. *Applied Physics Letters*, 82(20):3529–3531, 2003.

[5] S. H. Ko, H. Pan, C. P. Grigoropoulos, C. K. Luscombe, J. M. J. Frechet, and D. Poulikakos. All-inkjet-printed flexible electronics fabrication on a polymer substrate by low-temperature high-resolution selective laser sintering of metal nanoparticles. *Nanotechnology*, 18(34), 2007. Ko, Seung H. Pan, Heng Grigoropoulos, Costas P. Luscombe, Christine K. Frechet, Jean M. J. Poulikakos, Dimos.

[6] C. P. R. Dockendorf, G. Hwang, B.J. Nelson, C. P. Grigoropoulos, and D. Poulikakos. Maskless writing of a flexible nanoscale transistor with au-

contacted carbon nanotube electrodes. *accepted for publication in Applied Physical Letters*, 2007.

[7] C. P. R. Dockendorf, M. Steinlin, D. Poulikakos, and T. Y. Choi. Individual carbon nanotube soldering with gold nanoink deposition. *Applied Physics Letters*, 90(19), 2007. Dockendorf, Cedric P. R. Steinlin, Markus Poulikakos, Dimos Choi, Tae-Youl.

[8] J. Chung, N. R. Bieri, S. Ko, C. P. Grigoropoulos, and D. Poulikakos. In-tandem deposition and sintering of printed gold nanoparticle inks induced by continuous gaussian laser irradiation. *Applied Physics a: Materials Science & Processing*, 79(4-6):1259–1261, 2004.

[9] J. Chung, S. Ko, C. P. Grigoropoulos, N. R. Bieri, C. Dockendorf, and D. Poulikakos. Damage-free low temperature pulsed laser printing of gold nanoinks on polymers. *Journal of Heat Transfer-Transactions of the ASME*, 127(7):724–732, 2005.

[10] T. Y. Choi, D. Poulikakos, and C. P. Grigoropoulos. Fountain-pen-based laser microstructuring with gold nanoparticle inks. *Applied Physics Letters*, 85(1):13–15, 2004.

[11] C. P. R. Dockendorf, T. Y. Choi, D. Poulikakos, and A. Stemmer. Size reduction of nanoparticle ink patterns by fluid-assisted dewetting. *Applied Physics Letters*, 88(13), 2006.

[12] W. Escher, B. Michel, and D. Poulikakos. Efficiency of optimized bifurcating tree-like and parallel microchannel networks in the cooling of electronics. *International Journal of Heat and Mass Transfer*, 52(5-6):1421–1430, 2009.

[13] S. M. Senn and D. Poulikakos. Laminar mixing, heat transfer and pressure drop in tree-like microchannel nets and their application for thermal management in polymer electrolyte fuel cells. *Journal of Power Sources*, 130(1-2):178–191, 2004.

[14] S. M. Senn and D. Poulikakos. Polymer electrolyte fuel cells with porous materials as fluid distributors and comparisons with traditional channeled systems. *Journal of Heat Transfer-Transactions of the ASME*, 126(3):410–418, 2004.

[15] S. M. Senn and D. Poulikakos. Tree network channels as fluid distributors constructing double-staircase polymer electrolyte fuel cells. *Journal of Applied Physics*, 96(1):842–852, 2004.

[16] D. Lakehal, G. Larrignon, and C. Narayanan. Computational heat transfer and two-phase flow topology in miniature tubes. *Microfluidics and Nanofluidics*, 4(4):261–271, 2008.

[17] K. Fukagata, N. Kasagi, P. Ua-arayaporn, and T. Himeno. Numerical simulation of gas-liquid two-phase flow and convective heat transfer in a micro tube. In *International Conference on Heat Transfer and Fluid Flow in Microscale*, pages 72–82, Barga, Italy, 2005. Elsevier Science Inc.

[18] P. Urbant, A. Leshansky, and Y. Halupovich. On the forced convective heat transport in a droplet-laden flow in microchannels. *Microfluidics and Nanofluidics*, 4(6):533–542, 2008.

[19] M. Monde and Y. Mitsutake. Enhancement of heat transfer due to bubbles passing through a narrow vertical rectangular channel (change in heat transfer along flow). *Heat and Mass Transfer*, 31(1-2):77–82, 1995.

[20] P. Keblinski, S. R. Phillpot, S. U. S. Choi, and J. A. Eastman. Mechanisms of heat flow in suspensions of nano-sized particles (nanofluids). *International Journal of Heat and Mass Transfer*, 45(4):855–863, 2002.

[21] S. Lee, S. U. S. Choi, S. Li, and J. A. Eastman. Measuring thermal conductivity of fluids containing oxide nanoparticles. *Journal of Heat Transfer-Transactions of the ASME*, 121(2):280–289, 1999.

[22] P. G. Gennes, F. Brochard-Wyart, and Quéré. *Capillarity and Wetting Phenomena: Drops, Bubbles, Pearls, Waves.* Springer, Berlin, 2003.

[23] P. Gao, Z. Yin, and W. Hu. Thermocapillary motion of droplets at large marangoni numbers. *Advances in Space Research*, 41(12):2101–2106, 2008.

[24] Z. Yin, P. Gao, W. Hu, and L. Chang. Thermocapillary migration of nondeformable drops. *Physics of Fluids*, 20(8), 2008.

[25] J. Buongiorno. Convective transport in nanofluids. *Journal of Heat Transfer-Transactions of the ASME*, 128(3):240–250, 2006.

[26] R. L. Bohon and W. F. Claussen. The solubility of aromatic hydrocarbons in water. *Journal of the American Chemical Society*, 73(4):1571–1578, 1951.

[27] H. Stephen and T. Stephen. *Solubilities of Inorganic and Organic Compounds*, volume 1. The Macmillan Company, New York, Vol.1, Part 1, 1963.

[28] L. E. Scriven. On the dynamics of phase growth. *Chemical Engineering Science*, 10(1-2):1–13, 1959.

[29] H. G. Landau. Heat conduction in a melting solid. *Quarterly of Applied Mathematics*, 8(1):81–94, 1950.

[30] A. Prosperetti. A generalization of the Rayleigh-Plesset equation of bubble dynamics. *Physics of Fluids*, 25(3):409–410, 1982.

[31] R.B. Bird, W.E. Stewart, and E.N. Lightfoot. *Transport Phenomena.* Wiley, New York, first edition, 1960.

[32] V.P. Carey. *Liquid-Vapor Phase Change Phenomena: An Introduction to the Thermophysics of Vaporization and Condensation Processes in Heat Transfer Equipment.* Hemisphere, Washington, 1992.

[33] S.P. Lin. Non-equilibrium phase change. In R. Narayanan and D. Schwabe, editors, *Lecture Notes in Physics: Interfacial Fluid Dynamics and Transport Processes*, pages 355–367. Springer, Berlin, 2003.

[34] M. Brust, M. Walker, D. Bethell, D. J. Schiffrin, and R. Whyman. Synthesis of thiol-derivatized gold nanoparticles in a 2-phase liquid-liquid system. *Journal of the Chemical Society-Chemical Communications*, (7):801–802, 1994.

[35] S. Levine, B. D. Bowen, and S. J. Partridge. Stabilization of emulsions by fine particles.1.partitioning of particles between continuous phase and oil-water interface. *Colloids and Surfaces*, 38(4):325–343, 1989.

[36] O. Ozen, D. Johnson, and R. Narayanan. Observations on interfacial convection in multiple layers without and with evaporation. In R. Narayanan and D. Schwabe, editors, *Lecture Notes in Physics: Interfacial Fluid Dynamics and Transport Processes*, pages 59–77. Spinger, Berlin, 2003.

[37] T. C. Illingworth and I. O. Golosnoy. Numerical solutions of diffusion-controlled moving boundary problems which conserve solute. *Journal of Computational Physics*, 209(1):207–225, 2005.

[38] C. J. Kim and M. Kaviany. A numerical method for phase-change problems. *International Journal of Heat and Mass Transfer*, 33(12):2721–2734, 1990.

[39] H. S. Lee and H. Merte. Spherical vapor bubble growth in uniformly superheated liquids. *International Journal of Heat and Mass Transfer*, 39(12):2427–2447, 1996.

[40] E. M. Sparrow, S. Ramadhyani, and S. V. Patankar. Effect of subcooling on cylindrical melting. *Journal of Heat Transfer-Transactions of the ASME*, 100(3):395–402, 1978.

[41] C.A.J. Fletcher. *Computational Techniques for Fluid Dynamics*, volume 1. Springer-Verlag, Berlin, 2nd edition, 1991.

[42] J.H. Ferziger and M. Peric. *Computational Methods for Fluid Dynamics*. Springer-Verlag, Berlin, 3rd edition, 2002.

[43] H.S. Carlslaw and J.C. Jaeger. *Conduction of Heat in Solids*. Oxford University Press, London, 2nd edition, 1959.

[44] P.J. Lindstrom and W.G. Mallard (Eds.). Nist chemistry webbook, nist standard reference database number 69. National Institute of Standards and Technology, Gaithersburg MD, June 2005 (http://webbook.nist.gov).

[45] D. R. Lide. *CRC Handbook of Chemistry and Physics*. Taylor & Francis, Boca Raton, 2005.

[46] G. Rother and G. H. Findenegg. Monolayer firms of PS-b-PEO diblock copolymers at the air/water- and an oil/water-interface. *Colloid and Polymer Science*, 276(6):496–502, 1998.

[47] M. Barak and Y. Katz. Microbubbles - pathophysiology and clinical implications. *Chest*, 128:2918–2932, 2005.

[48] J.L. Bull. Cardiovascular bubble dynamics. *Critical Reviews in Biomedical Engineering*, 33(4):299–346, 2005.

[49] E. A. Brujan. Collapse of cavitation bubbles in blood. *Europhys. Lett.*, 50(2):175–181, 2000.

[50] P. S. Epstein and M. S. Plesset. On the stability of gas bubbles in liquid-gas solutions. *Journal of Chemical Physics*, 18(11):1505–1509, 1950.

[51] A. Kabalnov, D. Klein, T. Pelura, E. Schutt, and J. Weers. Dissolution of multicomponent microbubbles in the bloodstream: 1. theory. *Ultrasound in Medicine and Biology*, 24(5):739–749, 1998.

[52] E. Rambod, M. Beizaie, M. Shusser, S. Milo, and M. Gharib. A physical model describing the mechanism for formation of gas microbubbles in patients with

mitral mechanical heart valves. *Annals of Biomedical Engineering*, 27:774–792, 1999.

[53] O. D. Kripfgans, J. B. Fowlkes, D. L. Miller, O. P. Eldevik, and P. L. and Carson. Acoustic droplet vaporization for therapeutic and diagnostic applications. *Ultrasound in Medicine and Biology*, 26(7):1177–1189, 2000.

[54] T. K. Goldstick. Oxygen transport. In J. H. V. Brown and D. S. Gann, editors, *Engineering Principles in Physiology*, pages 257–283. Academic Press, New York, 2nd edition, 1973.

[55] J. H. Meldon. Blood-gas equilibria, kinetics and transport. *Chemical Engineering Science*, 42(2):199–211, 1987.

[56] D. M. Eckmann, J. Zhang, J. Lampe, and P. S. Ayyaswamy. Gas embolism and surfactant-based intervention. implications for long-duration space-based activity. *Annals of the N.Y. Academy of Science*, 1077:256–269, 2006.

[57] I. Kutschka, Schoenrock, A. El Essawi, D. Pahari, M. Anssar, and W. Harringer. A new minimized perfusion circuit provides highly effective ultrasound controlled dearing. *Artificial Organs*, 31(3):215–220, 2007.

[58] S. N. Vaslef, R. W. Anderson, and R. J. Leonard. Use of a mathematical model to predict oxygen transfer rates in hollow fiber membrane oxygenators. *ASAIO Journal*, 40(4):990–996, 1994.

[59] T. J. Hewitt, B. G. Hattler, and W. J. Federspiel. A mathematical model of gas exchange in an intravenous membrane oxygenator. *Annals of Biomedical Engineering*, 26:166–178, 1998.

[60] J. Zhang, T. C. Nolan, T. Zhang, B. P. Griffith, and Z. J. Wu. Characterization of membrane blood oxygenation devices using computational fluid dynamics. *Journal of Membrane Science*, 288:268–279, 2007.

[61] W. J. Yang. Dynamics of gas bubbles in whole blood and plasma. *Journal of Biomechanics*, 4(2):119–125, 1971.

[62] M. Fischer, M. Dietzel, and D. Poulikakos. Thermally enhanced solubility for the shrinking of a nanoink droplet in a surrounding liquid. *International Journal of Heat and Mass Transfer*, 52(1-2):222–231, 2009.

[63] W. J. Yang, R. Echigo, D. R. Wotton, and J. B. Hwang. Esperimental studies of the dissolution of gas bubbles in whole blood and plasma: I. stationary bubbles. *Journal of Biomechanics*, 4:275–282, 1971.

[64] R. S. Srinivasan, W. A. Gerth, and M. R. Powell. Mathematical models of diffusion-limited gas bubble dynamics in tissue. *Journal of Applied Physiology*, 86:732–741, 1999.

[65] K. D. Vandegriff and J. S. Olson. Morphological and physiological factors affecting oxygen uptake and release by red blood cells. *Journal of Biological Chemistry*, 259(20):12619–12627, 1984.

[66] P. Keblinski, J. A. Eastman, and D. G. Cahill. Nanofluids for thermal transport. *Materials Today*, 8(6):36–44, 2005.

[67] X. Q. Wang and A. S. Mujumdar. Heat transfer characteristics of nanofluids: a review. *International Journal of Thermal Sciences*, 46(1):1–19, 2007.

[68] M. Joanicot and A. Ajdari. Applied physics - droplet control for microfluidics. *Science*, 309(5736):887–888, 2005.

[69] T. Cubaud and T. G. Mason. Capillary threads and viscous droplets in square microchannels. *Physics of Fluids*, 20(5):11, 2008.

[70] J. H. Xu, S. W. Li, J. Tan, Y. J. Wang, and G. S. Luo. Controllable preparation of monodisperse o/w and w/o emulsions in the same microfluidic device. *Langmuir*, 22(19):7943–7946, 2006.

[71] Y. C. Zhao, G. W. Chen, and Q. Yuan. Liquid-liquid two-phase flow patterns in a rectangular microchannel. *AIChE Journal*, 52(12):4052–4060, 2006.

[72] A. L. Dessimoz, L. Cavin, A. Renken, and L. Kiwi-Minsker. Liquid-liquid two-phase flow patterns and mass transfer characteristics in rectangular glass microreactors. *Chemical Engineering Science*, 63(16):4035–4044, 2008.

[73] C. Cramer, P. Fischer, and E. J. Windhab. Drop formation in a co-flowing ambient fluid. *Chemical Engineering Science*, 59(15):3045–3058, 2004.

[74] S. Shin, S. I. Abdel-Khalik, V. Daru, and D. Juric. Accurate representation of surface tension using the level contour reconstruction method. *Journal of Computational Physics*, 203(2):493–516, 2005.

[75] C. W. Hirt and B. D. Nichols. Volume of fluid (VOF) method for the dynamics of free boundaries. *Journal of Computational Physics*, 39(1):201–225, 1981.

[76] M. Sussman, P. Smereka, and S. Osher. A level set approach for computing solutions to incompressible 2-phase flow. *Journal of Computational Physics*, 114(1):146–159, 1994.

[77] D. Jamet, O. Lebaigue, N. Coutris, and J. M. Delhaye. The second gradient method for the direct numerical simulation of liquid-vapor flows with phase change. *Journal of Computational Physics*, 169(2):624–651, 2001.

[78] G. Tryggvason, B. Bunner, A. Esmaeeli, D. Juric, N. Al-Rawahi, W. Tauber, J. Han, S. Nas, and Y. J. Jan. A front-tracking method for the computations of multiphase flow. *Journal of Computational Physics*, 169(2):708–759, 2001.

[79] Y. Renardy and M. Renardy. Prost: A parabolic reconstruction of surface tension for the volume-of-fluid method. *Journal of Computational Physics*, 183(2):400–421, 2002.

[80] J. U. Brackbill, D. B. Kothe, and C. Zemach. A continuum method for modeling surface-tension. *Journal of Computational Physics*, 100(2):335–354, 1992. ISI Document Delivery No.: JB297 Times Cited: 860 Cited Reference Count: 34.

[81] L. Graetz. Über die Wärmeleitungsfähigkeit von Flüssigkeiten (on the thermal conductivity of liquids), part 1. *Ann. Phys. Chem.*, 18:79–94, 1883.

[82] B. C. Pak and Y. I. Cho. Hydrodynamic and heat transfer study of dispersed fluids with submicron metallic oxide particles. *Experimental Heat Transfer*, 11(2):151–170, 1998.

[83] F. H. Harlow and J. E. Welch. Numerical calculation of time dependent viscous incompressible flow of fluid with free surface. *Physics of Fluids*, 8:2182–2189, 1965.

[84] C. W. Shu and S. Osher. Efficient implementation of essentially non-oscillatory shock capturing shemes, ii. *Journal of Computational Physics*, 83:32–78, 1989.

[85] J. Chorin. Numerical solution of the navier-stokes equations. *Mathematics of Computations*, 22:745–762, 1968.

[86] C.S. Peskin. Numerical analysis of blood flow in the heart. *Journal of Computational Physics*, 25:220–252, 1977.

[87] S. Shin and D. Juric. Modeling three-dimensional multiphase flow using a level contour reconstruction method for front tracking without connectivity. *Journal of Computational Physics*, 180:427–470, 2002.

[88] S. Shin, S. I. Abdel-Khalik, and D. Juric. Direct three-dimensional numerical simulation of nucleate boiling using the level contour reconstruction method. *International Journal of Multiphase Flow*, 31(10-11):1231–1242, 2005.

[89] L. A. Girifalco and R. J. Good. A theory for the estimation of surface and interfacial energies .1. derivation and application to interfacial tension. *Journal of Physical Chemistry*, 61(7):904–909, 1957.

[90] T. Svitova, O. Theodoly, S. Christiano, R. M. Hill, and C. J. Radke. Wetting behavior of silicone oils on solid substrates immersed in aqueous electrolyte solutions. *Langmuir*, 18(18):6821–6829, 2002.

[91] E. Lajeunesse and G. M. Homsy. Thermocapillary migration of long bubbles in polygonal tubes. ii. experiments. *Physics of Fluids*, 15(2):308–314, 2003.

[92] S. M. S. Murshed, S. H. Tan, and N. T. Nguyen. Temperature dependence of interfacial properties and viscosity of nanofluids for droplet-based microfluidics. *Journal of Physics D-Applied Physics*, 41(8):5, 2008.

[93] S. C. Mohapatra, D. Loikits, and Ieee. Advances in liquid coolant technologies for electronics cooling. In *21st Annual IEEE Semiconductor Thermal Measurement and Management Symposium*, pages 354–360, San Jose, CA, 2005. Ieee.

[94] V. Velagapudi, R. K. Konijeti, and C. S. K. Aduru. Empirical correlations to predict thermophysical and heat transfer characteristics of nanofluids. *Thermal Science*, 12(2):27–37, 2008.

[95] E.R.G. Eckert and R.M. Drake. *Heat and Mass Transfer, Part A*. McGraw-Hill, New York, 2nd edition, 1959.

[96] W.M. Deen. *Analysis of Transport Phenomena*. Oxford University Press, Oxford, 1st edition, 1998.

[97] J. G. Hnat and J. D. Buckmaster. Spherical cap bubbles and skirt formation. *Physics of Fluids*, 19(2):182–194, 1976.

Appendix A

Validation of the 1D-Program

The simulation program for the calculation of the shrinking process of nanoink droplets was validated in several test cases. The grid independence was ensured in parametric studies resulting in an optimal number of 200 grid points for both phases. Results of calculations with a fixed droplet radius and the absence of thermophoresis were compared with analytical solutions. The analytical solution for the equation of thermal conduction of a sphere and a hollow spherical body can be found in the textbook by Carlslaw and Jaeger [43]. The solution for the hollow sphere is given as:

$$\begin{aligned}\phi(R,\tau) =& \frac{R_0\phi_{\max}}{R} - \frac{R_0\phi_{\max}\,(R-R_0)}{R\,(R_{\max}-R_0)} \\ &+ \frac{2}{R\pi}\sum_{n=1}^{\infty}\sin\frac{n\pi\,(R-R_0)}{(R_{\max}-R_0)}e^{-n^2\pi^2\tau/(R_{\max}-R_0)^2}.\end{aligned} \tag{A.1}$$

In Figure A.1, the error of the numerical solution, compared to the analytical solution of the temperature field inside the droplet, is plotted over the radial coordinate for different time steps. It can be seen that the maximal error is 2.5×10^{-5} compared to the analytical solution. Calculations for the concentration field give similar results. Overall mass conservation was monitored throughout all calculations, showing practically no mass leakage. In Figure A.2, the mass leakage in per cent is plotted at the beginning of the shrinking process. It can be seen that the increase in lost

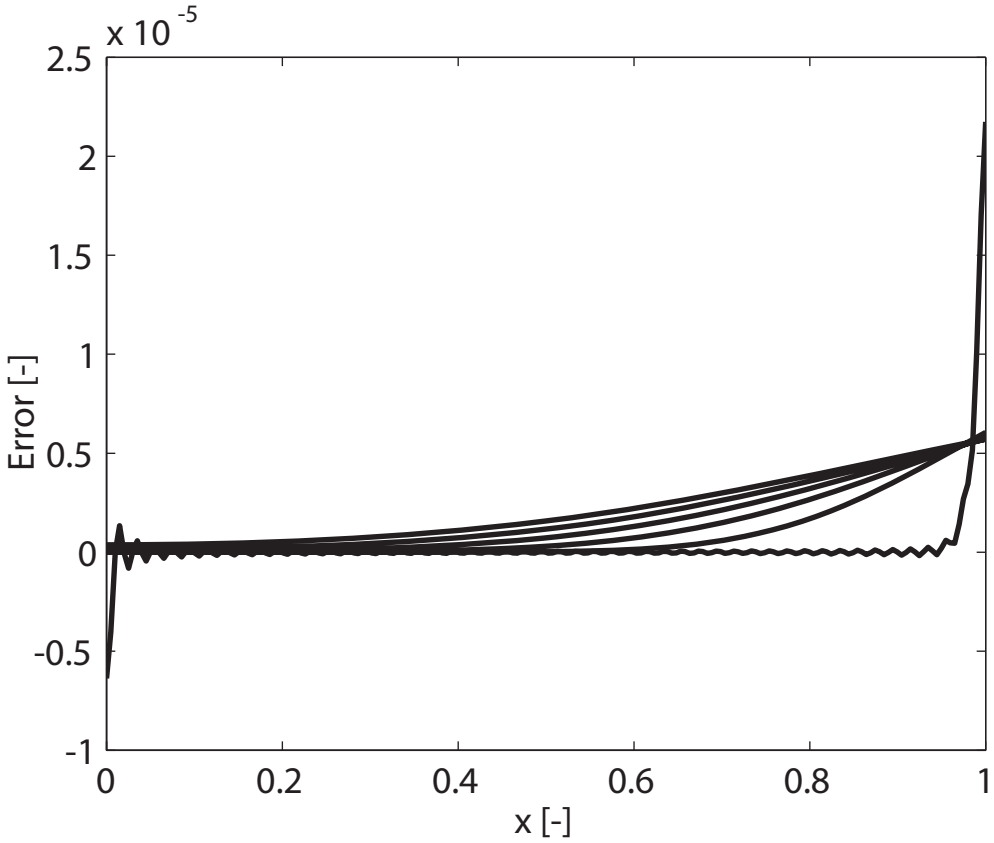

Figure A.1: Error of the numerical solution of the temperature field inside the droplet.

mass is quite high at the beginning of the process. This is due to the initially steep concentration gradient resulting in high mass fluxes at the beginning of the shrinking process.

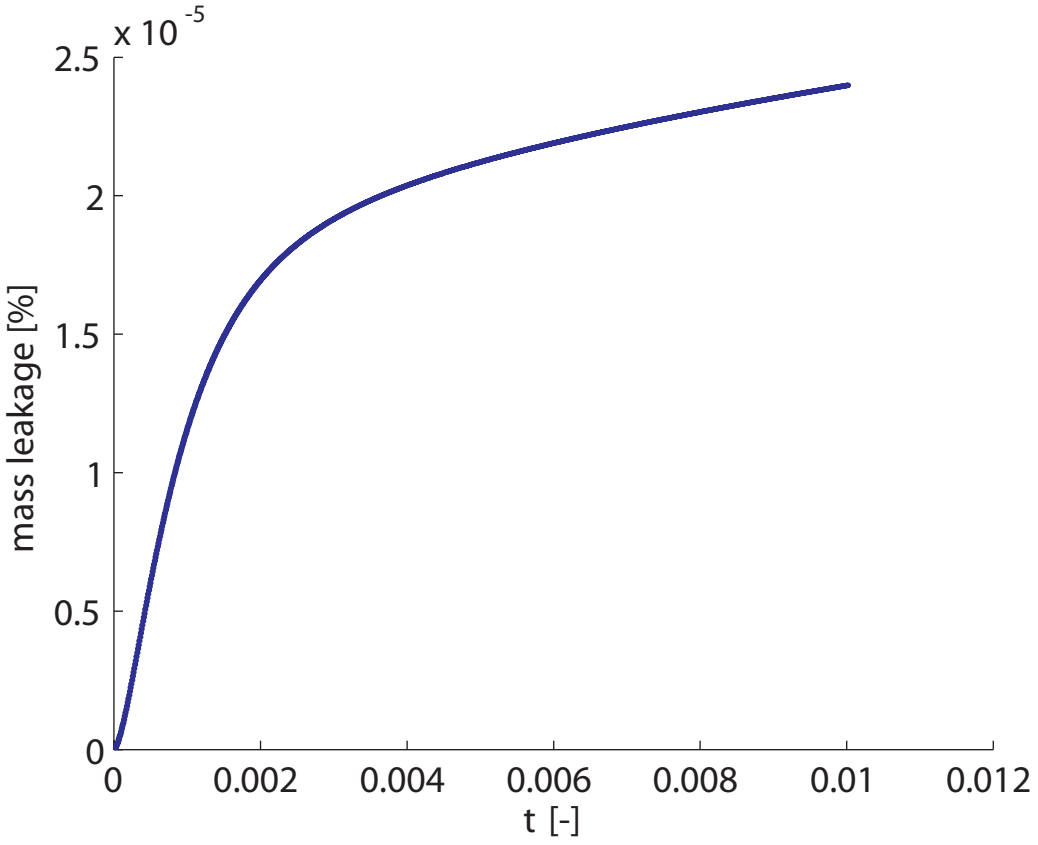

Figure A.2: Temporal evolution of the mass leakage at the beginning of the shrinking process .

Appendix B

Validation of the Front Tracking Program

The Front Tracking program was validated with experiments conducted by Hnat and Buckmaster, who investigated the shape and skirt formation of gas bubbles rising in mineral oil [97]. The parameters of the program were chosen to mach the spherical cap bubble A of the experiments. For this bubble configuration the constant rise velocity is $21.5\,\mathrm{cm\,s^{-1}}$. In Figure B.1, the rise velocity of the bubble is plotted in time. The velocity is normalized by the velocity obtained in the experiments. One can see, that the bubble accelerates at the initiation of the process and reaching a peak velocity of 1.1. After that the velocity drops slightly and the constant rise velocity is reached. The numerically obtained constant rise velocity is slightly lower than the one obtained by the experiments. This is a reason of near wall effects due to the confined domain. The actual shape of the bubble is plotted in Figure B.2. Further validation of the program included a test with identical the physical properties for the carrier and the droplet liquid. In this cases the calculated property, pressure and velocity fields showed the behavior of a single liquid flow. The Front Tracking program including the hybrid approach to calculated surface tension was validated in a study by Shin et al. [74]. In this study it is shown, that the spurious

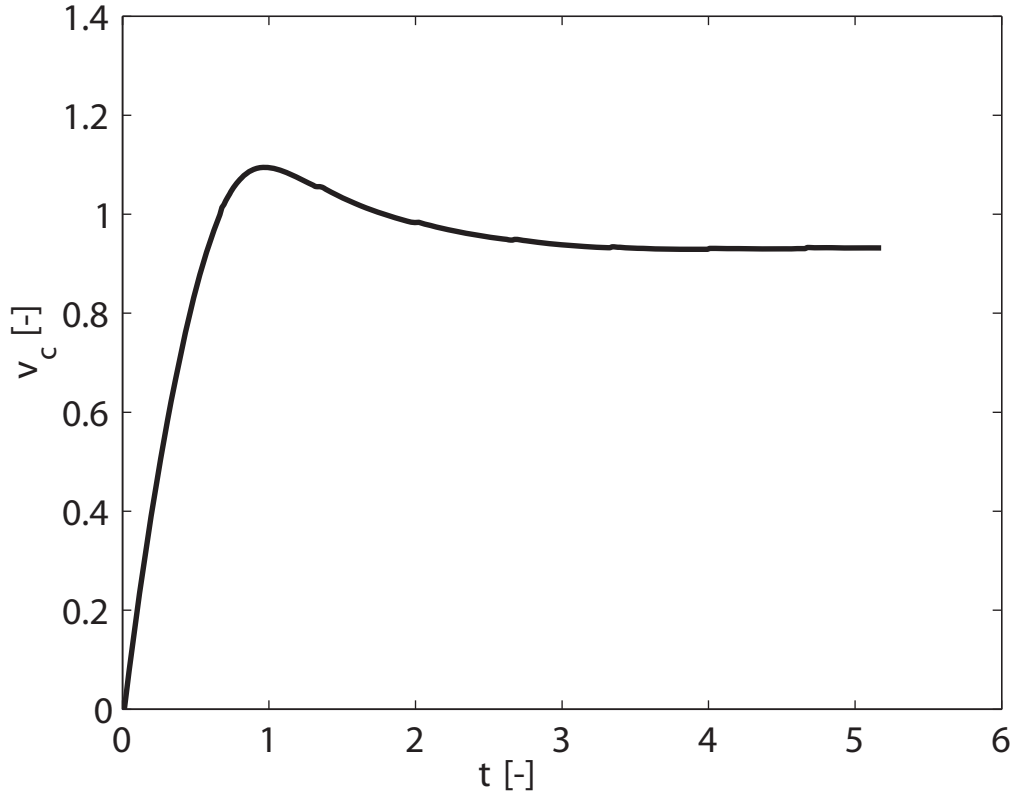

Figure B.1: Temporal evolution of the bubble rise velocity.

currents can be significantly reduced by orders of magnitudes when using the hybrid approach to calculate surface tension. The magnitude of the velocity of the spurious currents around a spherical droplet in static equilibrium was calculated to be at the order of 10^{-15}.

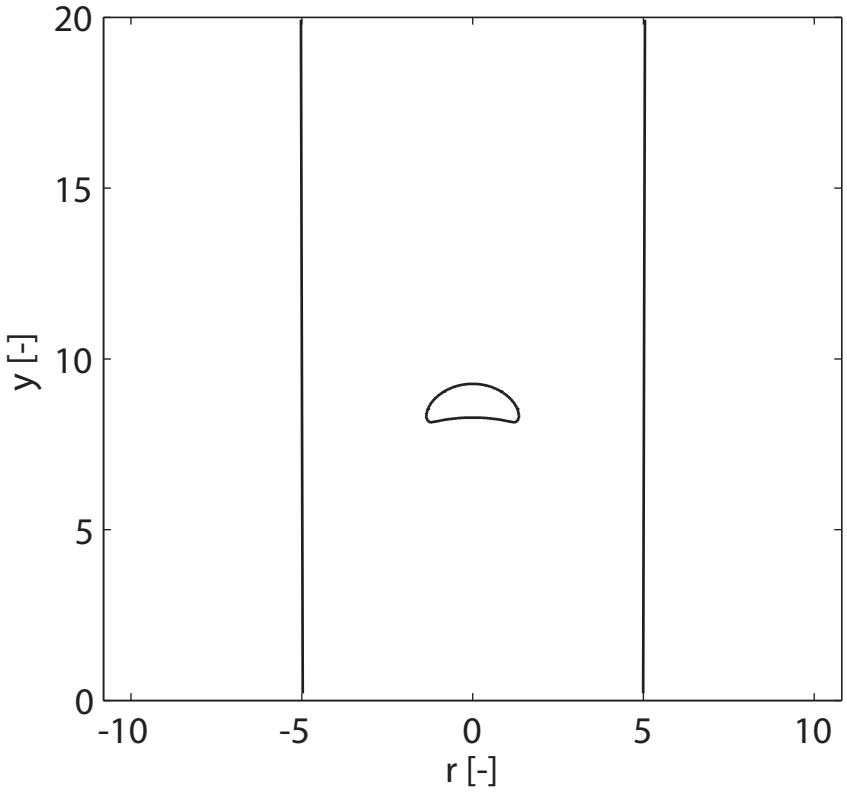

Figure B.2: The shape of the spherical cap bubble.

Curriculum Vitae

Personal Information

Name	Magnus Fischer
Date of birth	March 3^{rd}, 1978
Place of birth	Mannheim, Germany
Nationality	German

Education

07/2005 - 04/2009	ETH Zürich, Switzerland Ph.D. student, Laboratory of Thermodynamics in Emerging Technologies
10/2001 - 05/2005	Technische Universität Darmstadt, Germany Graduation in Mechanical Engineering (Dipl. Ing.)
08/2002 - 05/2003	University of California, Berkeley, USA Graduate studies in Mechanical Engineering
04/1999 - 02/2001	Technische Universität Bergakademie Freiberg, Germany Bachelor in Mechanical Engineering
07/1997	Wilhelmi-Gymnasium Sinsheim, Germany Abitur

Experience

09/2005 - 09/2008	ETH Zürich, Switzerland Teaching assistant in Thermodynamics
10/2004 - 05/2005	Volkswagen AG, Wolfsburg, Germany Diploma (Master) Thesis
10/2003 - 08/2004	Fluent Deutschland GmbH, Darmstadt, Germany Student assistant
07/2003 - 09/2003	Airbus Deutschland GmbH, Hamburg, Germany Internship
03/2001 - 08/2001	University of Nebraska Lincoln, Omaha, USA Research assistant
08/1999 - 10/1999	Tele Quarz GmbH, Neckarbischofsheim, Germany Internship
10/1998 - 11/1998	Heidelberger Druckmaschinen AG, Wiesloch, Germany Internship
07/1997 - 10/1998	Maison de la Retraite Protestante, Annonay, France Civil Service